Alma Mater Studiorum · Università di Bologna

Dottorato di Ricerca in Fisica
XXIX Ciclo

Settore Concorsuale di afferenza: 02/A1

Settore Scientifico Disciplinare: FIS/01

A tracking detector to study $\boldsymbol{O}$(1 GeV) ν_μ CC interactions

Presentata da: **Laura Pasqualini**

Coordinatore Dottorato:
Prof. Gastone Castellani

Relatore:
Dott.ssa Laura Patrizii

Correlatori:
Dott.ssa Nicoletta Mauri
Dott. Michele Pozzato

Esame finale anno 2017

Contents

Introduction

The paradigm of three standard neutrinos oscillations has been confirmed by several experiments. However, existing experimental “anomalies” may indicate the presence of one or more additional neutrinos, called “sterile” neutrinos, that do not interact weakly but participate to the oscillation phenomenon with ordinary neutrinos. To confirm or rule out the hypothesis of sterile neutrinos, a short baseline accelerator neutrino experiment was proposed to study $\nu_\mu \rightarrow \nu_e$ oscillations using two identical detectors at near and far positions, 300 m and 1600 m from the neutrino source, respectively. At each position the detector would consist of a Liquid Argon TPC to measure ν_e appearance and two magnetic spectrometers to measure the charge sign and momentum of muons produced in ν_μ CC interactions. An iron spectrometer would reconstruct muons up to 30 GeV/c, while an air light spectrometer would be dedicated to reconstruct low energy muons ($\sim$ 0.5-5 GeV/c). In particular, the light spectrometer would be required to separate μ^+/μ^- with $< 3\%$ charge misidentification at $\sim$ 1 GeV/c.

Different detectors were considered for instrumenting the magnetized air volume. In this thesis a tracking system is proposed based on planes of scintillator bars of triangular cross section (3.3 cm wide and 1.7 cm high) with embedded WaveLength Shifter (WLS) fibers. Each fiber is coupled at one end of the scintillator bar to a Silicon PhotoMultiplier (SiPM) readout in analog mode. SiPM features like single photon detection, reduced size, low power consumption, insensitivity to magnetic fields make them an optimal choice in designing a tracking device to be placed inside a magnetized volume. The particle trajectory can be reconstructed by determining, on each plane, the particle crossing position. It will be shown that the particle crossing position can be determined at millimeter level accuracy by measuring the amplitude of the analogue SiPM signals in adjacent bars.

In this thesis the activities carried out to design and test a prototype tracking system and the results obtained are reported. In Chapter 1 the experimental results that confirm standard neutrino oscillations and the experimental anomalies that may hint to sterile neutrinos are recalled. An experimental approach proposed to search for sterile neutrinos at the eV mass scale is described. In Chapter 2 the features and the operating principle of the different components of the devised tracking system (scintillation detectors, SiPM and WLS fibers) are discussed. Laboratory tests on SiPM and scintillator bars characterization are reported in Chapter 3. Results obtained testing a preliminary tracking detector with cosmic muons are also discussed. In Chapter 4 the tracker prototype is described, as well as the adopted front-end electronics and the beam tests carried out at the CERN PS. The beam test data analysis procedure is described in Chapter 5. Finally the spatial resolution and efficiency are derived and discussed.

Chapter 1

The Framework of Neutrino Oscillations

1.1 Neutrinos in the standard model of particle physics

The existence of neutrinos was proposed for the first time in 1930 by J. W. Pauli in order to explain the continuous spectrum of electrons emitted in β decay consistently with the principle of energy conservation. He suggested that the missing energy in the decay process is carried by a new type of particle emitted with the electron. He stated that this new particle should have been neutral with spin 1/2 and he called it "neutron" [1]. After Chadwick discovered the neutron as the neutral component of nucleus in 1932, Fermi proposed to call the missing particle of the β decay "neutrino".

The experimental discovery of electron neutrinos was achieved in 1956 by Reines and Cowan [2]. The detector consisted of a target of cadmium chloride dissolved in 400 liters of water and surrounded by scintillators. The detector was exposed to a flux of anti-neutrinos produced by reactors. The interaction of an anti-neutrino with a proton of the target would produce a neutron and a positron through inverse β decay. The signal from an $\overline{\nu}_e$ was identified through the detection of the light emitted from the positron annihilation and the subsequent neutron capture few microseconds after.

In 1962 the experiment of Schwartz, Lederman and Steinberg showed the existence of a second type of neutrino associated to the muon and produced in pions decay ($\pi \to \mu + \nu$) [3].

Between 1974 and 1977 e^+e^- collisions at SLAC led to the discovery of the τ lepton to which a third neutrino ν_τ might be associated. The study of the Z boson decay width at the e^+e^- LEP collider confirmed the existence of only three families of neutrinos [4]. The experimental results obtained at LEP are shown in Fig. 1.1.

The experimental evidences of ν_τ existence came in 2001 at Fermilab by

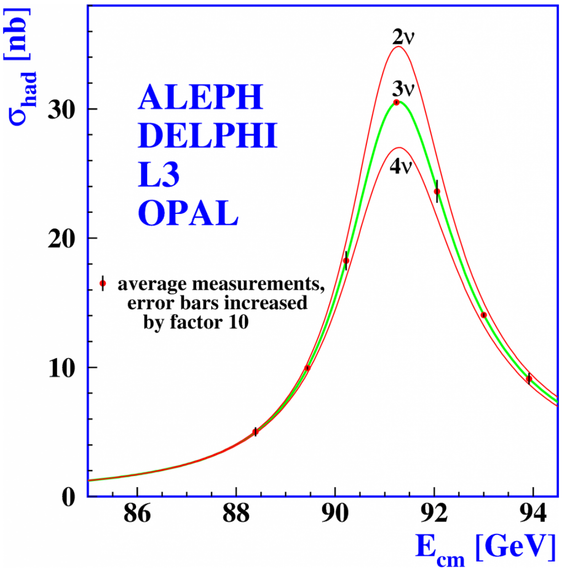

Figure 1.1: The curves are the theoretical predictions of the total cross-section σ_{had} for the production of hadrons as a function of the center of mass energy E_{cm} assuming the existence of 2, 3 and 4 neutrino families. The dots are the experimental data obtained at LEP.

the DONUT experiment [5], through the selection of the events with the characteristic τ decay tracks produced by charged current ν_τ interactions with an iron instrumented target.

The Standard Model (SM) of electroweak interactions, developed in 1960's, provided a theoretical framework to incorporate neutrinos as left-handed (LH) partners to the charged leptons. Over the years, also the strong interactions and the Higgs mechanism, have been included in the model.

The SM is defined by the gauge symmetry $SU(3)_C \times SU(2)_L \times U(1)_Y$. The groups $SU(2)_L \times U(1)_Y$ concern the electroweak sector, L index represents the left chirality of the particles and Y is the weak hypercharge. The $SU(3)_C$ group describes the strong interaction in the quark sector where C is the index used to denote the quark "color".

In the SM the particles are grouped in two main categories, gauge bosons of spin 1 and fundamental fermions of spin 1/2. Gauge bosons mediate the fundamental interactions: photons for the electromagnetic interaction, $W^\pm$ and Z^0 for the weak interaction and 8 gluons for the strong interaction. In July 2012 the ATLAS and CMS experiments at CERN's LHC announced the discovery of the Higgs boson [6, 7]. This particle of spin 0 is associated with the Higgs field that generates the masses of quarks and charged leptons through the Higgs mechanism. The fundamental fermions, quarks and leptons, are organized in $SU(2)_L$ doublets of left chirality and $U(1)_Y$ singlets of right chirality and they can be represented in three families:

$$\begin{aligned}
1)\begin{pmatrix}\nu_e\\ e^-\end{pmatrix}_L, \quad e_R^-, \quad \begin{pmatrix}u\\ d\end{pmatrix}_L, \quad u_R, \quad d_R\\
2)\begin{pmatrix}\nu_\mu\\ \mu^-\end{pmatrix}_L, \quad \mu_R^-, \quad \begin{pmatrix}c\\ s\end{pmatrix}_L, \quad c_R, \quad s_R\\
3)\begin{pmatrix}\nu_\tau\\ \tau^-\end{pmatrix}_L, \quad \tau_R^-, \quad \begin{pmatrix}t\\ b\end{pmatrix}_L, \quad t_R, \quad b_R
\end{aligned} \tag{1.1}$$

In this representation only left-handed neutrinos and right-handed antineutrinos exist, they can interact only through the weak force and they are massless particles. However, the observation of neutrino mixing, which is an evidence of physics Beyond the SM, is not consistent with the assumption of massless neutrinos.

Beyond the SM, there are different ways to assign a non-zero mass to neutrinos:

- By introducing a neutrino of right chirality ν_R and its coupling with the Higgs field that generates a Dirac mass term m_D. The corresponding Lagrangian is:

  $$\mathcal{L}_{m_D} = -m_D(\overline{\nu}_L\nu_R + \overline{\nu}_R\nu_L) \tag{1.2}$$

  In this approach the leptonic quantum number is conserved, and neutrinos differs from antineutrinos.

- By adding a Majorana mass term of left chirality m_L with the corresponding Lagrangian:

  $$\mathcal{L}_{m_L} = -\frac{m_L}{2}(\overline{\nu}_L(\nu_L)^C + \overline{\nu}_L^C\nu_L) \tag{1.3}$$

  where ν^C is the charge conjugate that fulfils the condition $\nu = \nu^C$. In this hypothesis neutrino are Majorana particles, therefore neutrinos and antineutrinos are identical and the leptonic number is violated.

- By considering an unified approach where a Dirac-Majorana mass term m_R of right chirality is introduced:

  $$\mathcal{L}_{m_R} = -\frac{m_R}{2}(\overline{\nu}_R(\nu_R)^C + \overline{\nu}_R^C\nu_R) \tag{1.4}$$

If neutrinos have both Majorana and Dirac mass components, the general Lagrangian can be written as:

$$\mathcal{L} = \mathcal{L}_{mD} + \mathcal{L}_{mL} + \mathcal{L}_{mR} = -\frac{1}{2}\begin{pmatrix}\bar{\nu}_L & \bar{\nu}_R^C\end{pmatrix}\begin{pmatrix}m_L & m_D\\ m_D & m_R\end{pmatrix}\begin{pmatrix}\nu_L\\ \nu_R^C\end{pmatrix} \tag{1.5}$$

From the diagonalization of the mass matrix one obtains:

$$m_{\pm} = \frac{1}{2}\left[m_L + m_R \pm \sqrt{(m_L - m_R)^2 + 4m_D^2}\right] \tag{1.6}$$

In the simplest version of the *see−saw* mechanism (the minimal type I seesaw model) the mass term m_L is zero and the right-handed neutrinos do not take part in weak interactions and so their mass can be large ($m_R >> m_D$). With these constraints there are two mass term resulting from the formula 1.6, an heavy mass term m_+ and a light mass term m_-:

$$m_+ \simeq m_R, \quad m_- \simeq \frac{m_D^2}{m_R} \tag{1.7}$$

This hypothesis can be in agreement with the SM if we consider that the SM is a theory that describes the universe only at low energy scale and the m_R is generated at ultra-high energy by the symmetry breaking of the theory beyond the SM. In this scenario there are three heavy sterile neutrinos with a mass of the order of m_R and three light neutrinos whose mass is suppressed by a factor m_D/m_R with respect to m_D.

1.2 Phenomenology of standard neutrino oscillations

The phenomenon of neutrinos oscillations was postulated for the first time in 1957 by B. Pontecorvo. He proposed the hypothesis of $\nu \to \overline{\nu}$ oscillations in analogy with $K \to \overline{K}$ oscillations [8], described as the mixing of two Majorana neutrinos. This hypothesis, afterwards overhauled and carried on by Maki, Nakagawa and Sakata (1967), asserts that the oscillations are due to the mixing between the flavour eigenstates (ν_e, ν_μ, ν_τ) and the mass eigenstates (ν_1, ν_2, ν_3). Therefore, the flavour eigenstates ν_α ($\alpha = e, \mu, \tau$) can be described as a linear combination of mass eigenstates ν_i ($i = 1, 2, 3$):

$$|\nu_\alpha\rangle = \sum_i U_{\alpha i} |\nu_i\rangle \tag{1.8}$$

where U is the unitary lepton mixing matrix (Pontecorvo-Maki-Nakagawa-Sakata matrix).

Considering oscillations in vacuum, the evolution in time t of the eigenstate ν_α is:

$$|\nu_\alpha(t)\rangle = \sum_i U_{\alpha i} |\nu_i(t)\rangle \tag{1.9}$$

where

$$|\nu_i(t)\rangle = e^{-iE_i t} |\nu_i(0)\rangle, \quad \mathcal{H} |\nu_i(t)\rangle = E_i |\nu_i(0)\rangle \tag{1.10}$$

The probability that a neutrino of flavour α oscillates into a neutrino of flavour β after a time t is given by:

$$\begin{aligned} P(\nu_\alpha \to \nu_\beta) &= |\langle \nu_\beta \mid \nu_\alpha(t) \rangle|^2 \\ &= \left| \sum_i U_{\beta i} e^{-iE_i t} U^*_{\alpha i} \right|^2 \\ &= \sum_i \sum_j U^*_{\alpha i} U_{\beta i} U_{\alpha j} U^*_{\beta j} e^{-i(E_i - E_j)t} \end{aligned} \tag{1.11}$$

taking into account relativistic neutrinos, $t \simeq L^2$ and the neutrino mass components energy can be approximated:

$$E_i \simeq E + \frac{m_k^2}{2E} \tag{1.12}$$

Therefore, the oscillation probability becomes:

$$\begin{aligned} P(\nu_\alpha \to \nu_\beta) &= \delta_{\alpha\beta} \\ -4 \sum_{i>j} &\mathcal{R}(U^*_{\alpha i} U_{\beta i} U_{\alpha j} U^*_{\beta j} sin^2[1.27 \Delta m^2_{ij}(L/E)]) \\ +2 \sum_{i>j} &\mathcal{F}(U^*_{\alpha i} U_{\beta i} U_{\alpha j} U^*_{\beta j} sin^2[2.54 \Delta m^2_{ij}(L/E)]) \end{aligned} \tag{1.13}$$

where $\Delta m^2_{ij} = m^2_i - m^2_j$ is in eV^2, L is the path length travelled by the neutrino in km and E is in GeV. The previous formula is valid for an arbitrary number of neutrino mass eigenstates.

In a simplified scenario with only two neutrinos involved in the mixing, the oscillation probability can be written as:

$$P(\nu_\alpha \to \nu_\beta) = \sin^2 2\theta \sin^2 \left[1.27 \frac{\Delta m^2 \left[eV^2\right] L \left[km\right]}{E \left[GeV\right]} \right] \tag{1.14}$$

The transition probability is defined by the amplitude of sinusoidal oscillation $\sin^2 2\theta$ where θ is the mixing angle and by the oscillation length l_{osc}, i.e. the distance between two adjacent maximum (or minimum) of the oscillation probability:

$$l_{osc} = \frac{4\pi E \hbar c}{|\Delta m^2|} \cong 2.48 \frac{E(GeV)}{|\Delta m^2| \, (eV^2)} [\text{km}] \tag{1.15}$$

The simplified formula 1.14 is valid in first approximation in oscillations neutrino experiments. In an experiment the values of the source-detector distance L and the neutrino energy E are fixed and the experiment can be realized in order to optimize the ratio L/E and therefore to maximize the oscillation probability. At a fixed value of L and E the experiment is sensitive to a particular range of Δm^2.

Extending the mixing to the three active neutrinos, the following notation can be used:

$$\begin{pmatrix}\nu_e\\ \nu_\mu\\ \nu_\tau\end{pmatrix} = U_{PMNS}\begin{pmatrix}\nu_1\\ \nu_2\\ \nu_3\end{pmatrix}$$

where the mixing matrix U_{PMNS} is parametrized as:

$$\begin{aligned} U_{PMNS} &= \begin{pmatrix}1 & 0 & 0\\ 0 & c_{23} & s_{23}\\ 0 & -s_{23} & c_{23}\end{pmatrix} \times \begin{pmatrix}c_{13} & 0 & s_{13}e^{-i\delta}\\ 0 & 1 & 0\\ -s_{13}e^{-i\delta} & 0 & c_{13}\end{pmatrix} \\ &\times \begin{pmatrix}c_{12} & s_{12} & 0\\ -s_{12} & c_{12} & 0\\ 0 & 0 & 1\end{pmatrix} \times \begin{pmatrix}e^{i\alpha_1/2} & 0 & 0\\ 0 & e^{i\alpha_2/2} & 0\\ 0 & 0 & 1\end{pmatrix} \end{aligned} \tag{1.16}$$

In this parametrization c_{ij} and s_{ij} stand for the sines and cosines of the mixing angles θ_{ij} respectively, δ is the Dirac phase associated with CP violation in the leptonic sector and α $(i = 1, 2)$ are the Majorana phases.

The first matrix contain the leading terms of ν oscillations in the atmospheric sector. The second matrix is usually associated with the oscillations of reactor neutrino $(\overline{\nu}_e \rightarrow \overline{\nu}_\mu, \overline{\nu}_\tau)$. Solar neutrino experiments that involve the oscillation $\nu_e \rightarrow \nu_\mu$ can investigate the parameters of the third matrix. The last matrix contains the Majorana phases that cannot be inferred from neutrino oscillations. These parameters can be studied with neutrinoless double beta decay where conservation of leptonic number is violated.

A more general case is considered for neutrino travelling through matter. Despite the interaction probability of neutrinos with matter is very low (around 10^{-12} at MeV energy scale), the coherent forward scattering of neutrino from particles in matter can modify the oscillation pattern. Since the matter contains electrons, the ν_e interacts with matter differently with respect to $\nu_{\mu,\tau}$ and therefore the propagation depends on the neutrino flavour. This effect, called MSW (Mikheyev-Smirnov-Wolfenstein), foresees that the relation between mass eigenstates and flavour eigenstates depends also on coefficients related to the density of electrons in matter. For electron neutrino the additional term in the Hamiltonian is given by:

$$\sqrt{2}G_F N_e \tag{1.17}$$

where G_F is the Fermi constant and N_e is the electron density in matter. The same contribution is not present in the Hamiltonian for ν_μ and ν_τ, since in ordinary matter the corresponding charged leptons μ and τ are not present, hence scattering due to charged current interaction are not possible.

Neutrino oscillations do not give information about the sign of neutrino mass squared differences. There are two possible ordering schemes for neutrino masses both consistent with the results on neutrino experiments: in the normal hierarchy neutrino masses are ordered such $m_1 < m_2 << m_3$, while in the inverted hierarchy the ordering is $m_3 << m_2 < m_1$ as shown in Fig. 1.2.

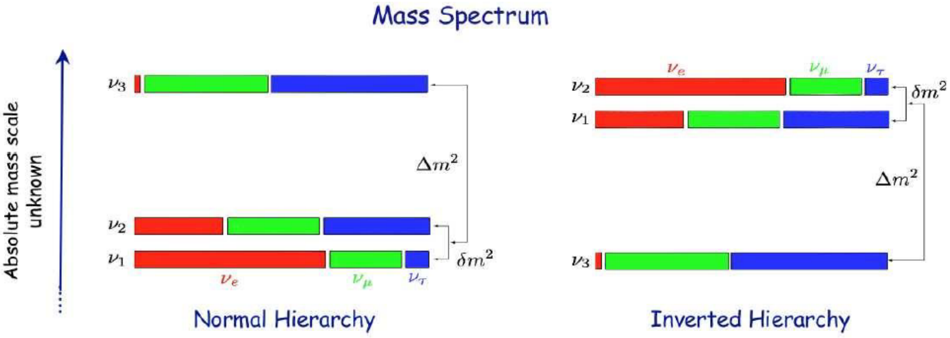

Figure 1.2: The two possible scenarios for neutrino mass ordering in the picture of three active neutrino. (Left) the mass spectrum in the hypothesis of normal hierarchy, (right) the mass spectrum in the case of inverted hierarchy.

1.3 The current experimental scenario

Many experiments on neutrino oscillations have established that neutrinos oscillate and therefore, contrary to what assumed in the SM, they have mass.

Some of these experiments use artificial neutrinos sources like nuclear reactors or accelerators, while others use natural source such as solar ($\odot$) neutrinos or atmospheric (atm) neutrinos. Neutrino oscillation experiments can look for the appearance of a neutrino flavour different from the one produced by the source (*appearance* experiments) or can observe a decrease in the flux of the neutrino flavour produced by the source (*disappearance* experiments). Different experiments, involving neutrinos of different energies travelling over different distances, can measure different Δm^2. The measurements of the mass differences shows a clearly separated spectrum:

$$\Delta m^2_\odot = \left|\Delta m^2_{12}\right| << \left|\Delta m^2_{13}\right| \simeq \left|\Delta m^2_{23}\right| = \Delta m^2_{atm} \tag{1.18}$$

The experiments on solar and reactor neutrinos are sensitive to $\Delta m^2_\odot$ and $\sin^2 2\theta_\odot$, while experiments on atmospheric and accelerator neutrinos measure Δm^2_{atm} and $\sin^2 2\theta_{atm}$.

1.3.1 Solar neutrinos

Solar neutrinos are produced by the Sun through fusion reactions in the pp chain and CNO cycle.

The first experimental evidence of neutrino oscillations was found with the Homestake experiment by studying the reaction $\nu_e +^{37} Cl \rightarrow^{37} Ar + e^-$. The experiment detected a flux of ν_e equal to 1/3 of that expected from the Standard Solar Model (SSM) [9], opening the so called "solar neutrino problem". In the '90s SAGE and Gallex/GNO observed 71 SNU[1] over the

---

[1] Solar Neutrino Units = 10^{-36} captures per second per absorber nucleus

130 expected through the reaction $\nu_e +^{71} Ga \rightarrow^{71} Ge + e^-$ [10].

Another category of solar neutrino experiments uses Cherenkov detectors. For example SuperKamiokande (SK) experiment uses a detector containing 50 kt of water, with a fiducial mass of 22.5 kt. The Cherenkov light is seen by inner-facing phototubes (PMTs). The experiment studied the CC $\nu_e + e^- \rightarrow \nu_e + e^-$ and NC $\nu + e^- \rightarrow \nu + e^-$ interactions, observing a deficit in the expected solar neutrino flux [11]. The SNO (*Sudbury Neutrino Observatory*) experiment used a heavy water (D_2O) target surrounded by photomultipliers in order to detect the Cherenkov light produced in three reactions: CC $\nu_e d \rightarrow ppe^-$, NC $\nu_x d \rightarrow pn\nu_x$ and the elastic scattering $\nu_x e^- \rightarrow \nu_x e^-$. The first reaction is sensitive only to ν_e, thus allowing to measure the flux $\Phi(\nu_e) = \Phi_{CC}$, while the others reactions are sensitive to all neutrino flavour and therefore is it possible to measure $\Phi(\nu_e + \nu_\mu + \nu_\tau) = \Phi_{NC}$. The observed ratio Φ_{CC}/Φ_{NC} was $\sim 1/3$ of the expected flux providing a proof for solar neutrino oscillations.

1.3.2 Atmospheric neutrinos

Atmospheric neutrinos are produced in the decay of secondary cosmic rays, mainly pions and kaons, created in the interactions of primary cosmic rays with the nuclei of the Earth's atmosphere. Pions and kaons decay mainly through the reactions $\pi^+ \rightarrow \mu^+ \nu_\mu$, $K^+ \rightarrow \mu^+ \nu_\mu$ and $\mu^+ \rightarrow e^+ \nu_e \overline{\nu}_\mu$ and the ratio between the numbers of muon to electron neutrinos is known at 5 %:

$$R = \frac{N_{\nu_\mu} + N_{\overline{\nu}_\mu}}{N_{\nu_e} + N_{\overline{\nu}_e}} \simeq 2 \tag{1.19}$$

Atmospheric neutrino oscillations could manifest as a discrepancy between the measured and the expected value of the ratio R. The Kamiokande-II [12], SuperKamiokande [13], Soudan-2 [14] and MACRO [15] detectors reported energy dependent deficits in the ν_μ fluxes with respect to the predictions and a distortion of the angular distributions.

The Soudan-2 experiment used a modular fine grained tracking and showering calorimeter located in Soudan Gold mine in Minnesota. The experiment measured the ratio $R = (N_{\nu_\mu}/N_{\nu_e})_{DATA}/(N_{\nu_\mu}/N_{\nu_e})_{MC}$ = (0.68 $\pm$ 0.11), consistent with $\nu_\mu \rightarrow \nu_\tau$ oscillations with maximal mixing and $\Delta m^2_{2,3} = 5.2 \times 10^{-3}$ eV^2.

The MACRO experiment, operated at the Gran Sasso underground Lab from 1989 to 2000, used 3 different sub-detectors: scintillation counters, limited streamer tubes and nuclear track detectors. Results are in agreement with the hypothesis of $\nu_\mu \rightarrow \nu_\tau$ oscillations, with maximal mixing and $\Delta m^2_{23} \simeq 2.3 \times 10^{-3}$ eV^2, and rule out the no oscillation hypothesis by $\sim 5\sigma$ [16].

The SK experiment showed an evidence of an up/down asymmetry on the ν_μ flux, a deficit for the upgoing ν_μ was found, which can be explained

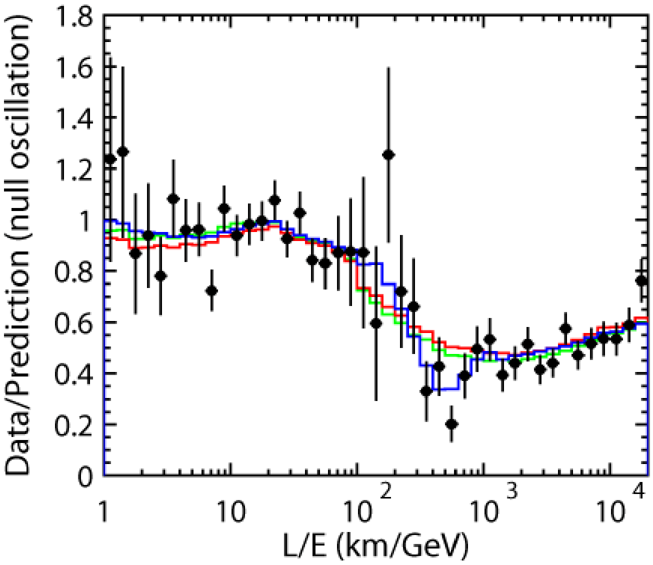

Figure 1.3: Results of the L/E analysis of SK-I atmospheric neutrino data. The points show ratio of the data to the Monte Carlo prediction without oscillations, as a function of the reconstructed L/E.

in terms of $\nu_\mu \to \nu_\tau$ oscillations with a maximal mixing $\Delta m^2_{atm} \sim 2 \times 10^{-3}$ eV^2. The SK results are shown in Fig. 1.3.

1.3.3 Nuclear reactor neutrinos

Nuclear reactors produce $\overline{\nu}_e$ emitted by fission with an energy of the order of few MeV. Due to the low energy, electrons are the only charged leptons that can be produced in neutrino CC interactions. If the $\overline{\nu}_e$ oscillates, a CC interaction cannot be observed because the neutrino has not enough energy to produce the associated charged lepton. Therefore reactor neutrino experiments are *dissapearance* experiments.

The $\overline{\nu}_e$ spectrum is calculated from measurements of $\beta-$decay spectra of ^{238}U, ^{239}Pu and ^{241}P after the fission. Through the comparison between the observed rate of positrons from the inverse β-decays and the predicted rate, these experiments can measure the oscillation parameters.

Two experiments were performed in order to measure θ_{13} parameter in disappearance mode: the CHOOZ experiment [17] and the Palo Verde experiment [18]. No evidence for $\overline{\nu}_e$ disappearance was found. The experiments obtained limits for $\overline{\nu}_e \to \overline{\nu}_\mu$ at the level of $\Delta m^2 > 10^{-3}$ eV^2 for $\sin^2 2\theta_{13} > 0.1$.

Recently 3 experiments, Daya Bay, Double Chooz and RENO, each using several nuclear reactors, measured the neutrino oscillation angle θ_{13}. θ_{13} was found to be small but not zero: the average value is $\sin^2\theta_{13} = 0.098 \pm 0.013$ [19].

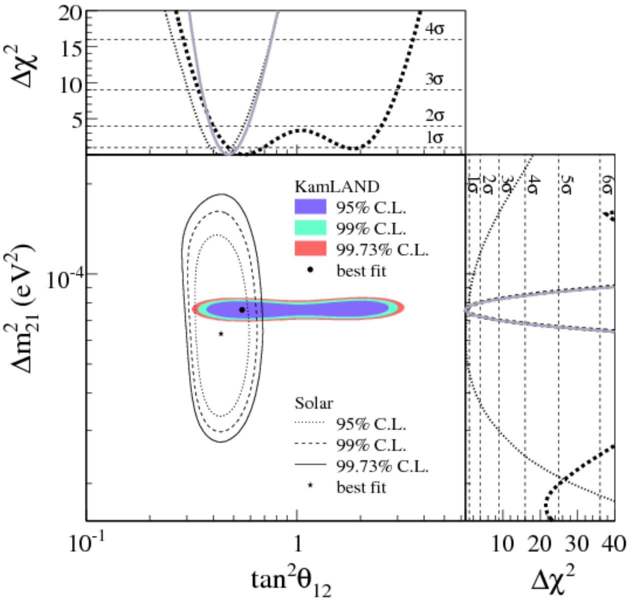

Figure 1.4: Allowed region for neutrino oscillation parameters from KamLAND and solar neutrino experiments. The side-panels show the $\Delta\chi^2$-profiles for KamLAND (dashed) and solar experiments (dotted) individually, as well as the combination of the two (solid).

The measured value of θ_{13} opens the possibility of performing precision measurements in the leptonic sector.

The solar neutrino sector was explored by the reactor experiment KamLAND [20]. The results of this experiment were in agreement with the solar neutrino experiments and by combining their data, the oscillation parameter were estimated as $\tan^2\theta_{12} = 0.47^{+0.06}_{-0.05}$ and $\Delta m^2_{12} = 7.59^{+0.21}_{-0.21} \times 10^{-5}$ eV^2 [21]. The allowed region in the neutrino oscillation parameter space obtained from KamLAND and solar neutrino experiments is shown in Fig. 1.4.

1.3.4 Accelerator experiments

Neutrino experiments at accelerator use beams of muon neutrinos travelling a distance L before their arrival at the detector. High energy neutrino beams are produced accelerating protons up to tens of GeV and impinging them on a target. The produced secondaries are momentum-selected by a series of lensing devices which focus them into a parallel beam in an evacuated decay tunnel of $\sim$ 1 km length. Two different kind of experiments are performed: *long baseline* experiments and *short baseline* experiments which differ for the travelled distance L. These experiments can look for the disappearance of the beam neutrinos or for the appearance of a different neutrino flavour in the beam. Typically these experiments has a *near* detector which measure the neutrinos energy spectrum in absence of oscillations and a *far* detector to measure the energy spectrum after neutrino oscillations.

The *long baseline* experiment K2K (KEK-to-Kamioka) used the SK detector as far detector in combination with a *near* detector $\sim$ 300 m away from the source, studying the ν_μ disappearance. The ν_μ spectrum seen by SK was compared with the prediction obtained with the measurements of the near detector and the atmospheric oscillation were confirmed at 4σ.

The *long baseline* MINOS experiments [22] operated with two equivalent detectors separated by 734 km. It had been designed to study ν_μ ($\overline{\nu}_\mu$) disappearance and ν_e appearance. Muon neutrinos and antineutrinos are produced by the NuMI facility using 120 GeV protons from the Fermilab Main Injector. This experiment has provided a very precise measurements of oscillation parameters $\Delta m^2_{32} = [2.28 - 2.46] \times 10^{-3}$ eV^2 at 68% C.L. and $\sin^2(\theta_{23}) = 0.35 - 0.65$ at 90% C.L. in the normal hierarchy, and $\Delta m^2_{32} = [2.32 - 2.53] \times 10^{-3}$ eV^2 at 68% C.L. and $\sin^2(\theta_{23}) = 0.34 - 0.67$ at 90% C.L. in the inverted hierarchy [23].

In the T2K (Tokai-to-Kamioka) experiment ν_μ are produced at J-Parc PS and travel a distance of $\sim$ 300 km before reaching the SK detector. It studies ν_μ disappearance and ν_e appearance in both neutrino and antineutrino mode. The experiment has provided the first observation of $\nu_\mu \rightarrow \nu_e$ oscillations. Running the detector in neutrino mode, the measured oscillation parameters are $\Delta m^2_{32} = (2.51 \pm 0.10) \times 10^{-3}$ eV^2 and $\sin^2(\theta_{23}) = 0.514^{+0.055}_{-0.056}$ [24]. Since 2014 T2K has been running with an $\overline{\nu}_\mu$ beam obtaining results consistent with the neutrino mode data.

The OPERA experiment was designed for the search of ν_τ appearance in a ν_μ beam (CNGS) produced at CERN SPS, 730 km far from the detector. Thanks to the use of nuclear emulsion OPERA has a micrometric resolution and is able to identify the short-lived τ lepton associated to the ν_τ. The experiment recorded events corresponding to 1.8×10^{19} p.o.t from 2008 to 2012 and 5 ν_τ candidates were observed at 5.1σ [25].

1.4 Experimental “anomalies”

Results of short baseline experiments require the existence of at least one additional squared mass difference Δm^2_{SBL} much larger than Δm^2_{SOL} and Δm^2_{ATM}.

The LSND experiment [26] observed an excess of $\overline{\nu}_e$ events in a beam of $\overline{\nu}_\mu$ produced by μ^+ decay at rest ($\mu^+ \rightarrow e^+ + \nu_e + \overline{\nu}_\mu$). The $\overline{\nu}_e$ events have been detected at a distance L $\simeq$ 30 m through the inverse neutron decay process ($\overline{\nu}_e + p \rightarrow n + e^+$) in a detector filled with liquid scintillator in the range $20 \lesssim E_e \lesssim 60$ MeV for the energy E_e of the detected positron. The nominal statistical significance of the LSND $\overline{\nu}_e$ appearance signal is of about 3.8σ. However, the similar KARMEN experiment [27] did not measure any excess of $\overline{\nu}_e$ events over the background at a distance L $\simeq$ 18 m. The LSND

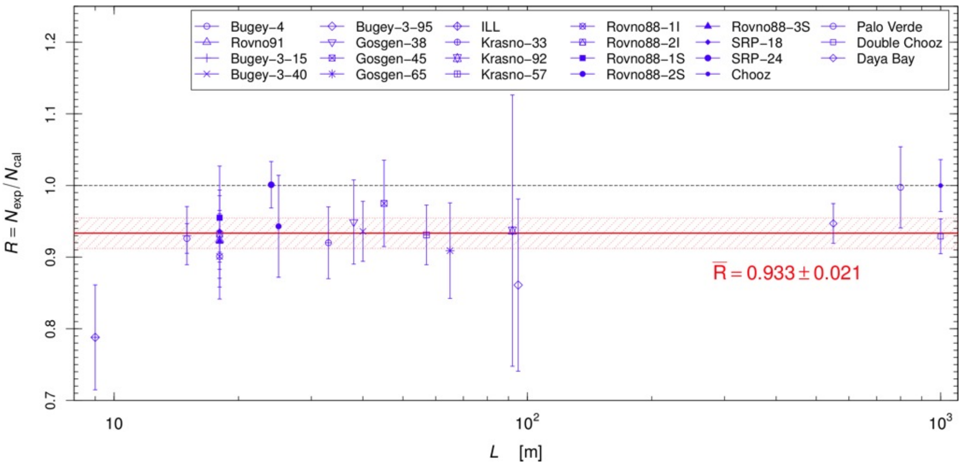

Figure 1.5: Ratio R of the measured (N_{exp}) and calculated (N_{cal}) number of $\overline{\nu}_e$ events in reactor experiments at different distances L. The horizontal shadowed red band shows the average ratio $\overline{R}$ and its uncertainty.

$\overline{\nu}_e$ appearance signal can be explained by $\overline{\nu}_\mu \to \overline{\nu}_e$ oscillations generated by a squared-mass difference of $\Delta m^2_{SBL} \gtrsim 0.1$ eV^2.

The MiniBooNE experiment was designed in order to check the LSND signal at the same baseline L/E by studying $\overline{\nu}_\mu \to \overline{\nu}_e$ and $\nu_\mu \to \nu_e$ transition. By combining the data from both channels, an excess of 3.8σ in the range $200 < E_\nu < 1250$ MeV have been observed. The results of MiniBooNE are ambiguous because the LSND signal was not seen in neutrino mode ($\nu_\mu \to \nu_e$) and the $\overline{\nu}_\mu \to \overline{\nu}_e$ signal observed in 2010 with the first half of the antineutrino data was not observed in the second half of the antineutrino data.

Another indications consists in the reactor antineutrino anomaly [28], which is a deficit of the rate of $\overline{\nu}_e$ observed in several short-baseline reactor neutrino experiments in comparison with that expected from the calculation of the reactor neutrino fluxes [29]. In particular the ratio R of the measured (N_{exp}) and calculated (N_{cal}) number of $\overline{\nu}_e$ events in the reactor experiments is shown in Fig. 1.5 and its average value is:

$$\overline{R} = 0.933 \pm 0.021 \tag{1.20}$$

with a statistical significance of about 3.2σ which depends on the estimated uncertainties of the calculated reactor antineutrino fluxes. The reactor antineutrino anomaly can be explained by neutrino oscillations with an oscillation length which is shorter than about 20 m. The relation between a squared-mass difference Δm^2 and the corresponding oscillation length is given by 1.15, therefore the required squared-mass differences is $\Delta m^2_{SBL} \gtrsim 0.5$ eV^2.

The Gallium neutrino anomaly refers to the ν_e flux from calibration

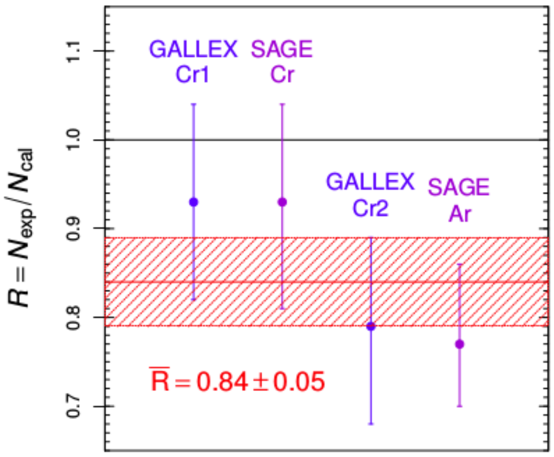

Figure 1.6: Ratio R of the measured (N_{exp}) and calculated (N_{cal}) number of ν_e events in the GALLEX and SAGE radioactive source experiments. The horizontal shadowed red band shows the average ratio $\overline{R}$ and its uncertainty.

sources measured by GALLEX [30] and SAGE [31] experiments.

These radiochemical experiments studied solar neutrinos detecting ν_e coming from the Sun through the reaction:

$$\nu_e +^{71} Ga \rightarrow^{71} Ge + e^- \tag{1.21}$$

Afterwards, in order to verify the efficiencies, the detectors were tested with intense artificial ^{51}Cr and ^{37}Ar radioactive sources which produce electron neutrinos through the electron captures:

$$e^- +^{51} Cr \rightarrow^{51} V + \nu_e, \quad e^- +^{37} Ar \rightarrow^{37} Cl + \nu_e \tag{1.22}$$

These tests have measured a rate of production of ^{71}Ge less than that was previously predicted from the calculation of Gamow-Teller coefficients. In Fig. 1.6 is shown the ratios R of the number of electron neutrino events (N_{exp}) measured in the GALLEX and SAGE radioactive source experiments and that calculated (N_{cal}) with the Gamow-Teller strengths. The average ratio is:

$$\overline{R} = 0.84 \pm 0.05 \tag{1.23}$$

which indicates a deficit with a nominal statistical significance of about 2.9σ. The Gallium neutrino anomaly can be explained by neutrino oscillations generated by a squared-mass difference of $\Delta m^2_{SBL} \gtrsim 1$ eV^2.

Many analyses of short-baseline neutrino oscillation data have been done since the discovery of these anomalies. Fig. 1.7 shows the allowed regions in the $sin^2 2\theta_{e\mu} - \Delta m^2_{41}$ plane obtained in the 3+1 fit. The combined disappearance constraint in that plane excludes a large part of the region allowed

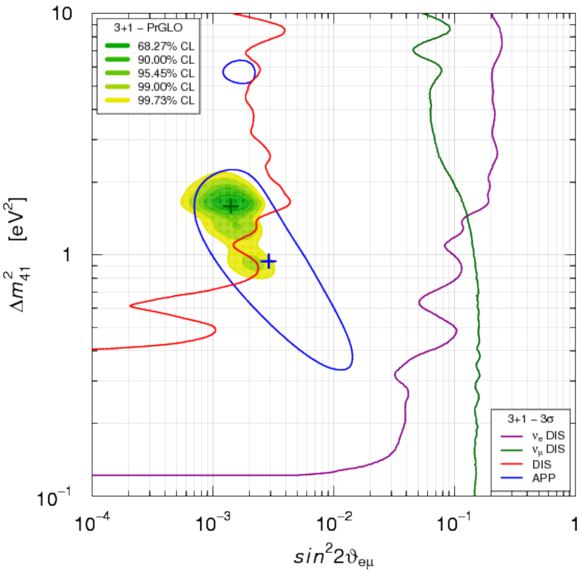

Figure 1.7: Allowed regions in the $sin^2 2\theta_{e\mu} - \Delta m^2_{41}$ plane obtained in the 3+1 global fit of short-baseline neutrino oscillation data compared with the 3σ allowed regions obtained from $\overline{\nu}_\mu \to \overline{\nu}_e$ short-baseline appearance data (APP) and the 3σ constraints obtained from $\overline{\nu}_e$ short-baseline disappearance data (ν_e DIS), $\overline{\nu}_\mu$ short-baseline disappearance data (ν_μ DIS) and the combined short-baseline disappearance data (DIS).

by $\overline{\nu}_\mu \to \overline{\nu}_e$ appearance data, leading to the appearance-disappearance tension [32].

The existence of massive sterile neutrino at eV scale can affect the standard ΛCDM cosmological framework, producing effects on the observables generated in the first part of the evolution of the Universe, when the sterile neutrinos were relativistic, namely the Cosmic Microwave Background (CMB) and the nuclear abundances produced by Big Bang Nucleosynthesis (BBN). From cosmological data results that the effective number of neutrino is $N_{eff} = 3.046$ [33].

Recent measurements of the CMB anisotropies coming from the 2015 updated data analysis of the Planck experiment give constraints on the sum of the active neutrino masses $\sum m_\nu$ [34]:

$$\sum m_\nu < 0.23 \quad eV \tag{1.24}$$

Up to now cosmological data disfavoured very strongly the hypothesis of a 4th sterile neutrino.

1.4.1 Light Sterile Neutrinos

The hypothesis of light sterile neutrinos was introduced to explain anomalies found in oscillation experiments.

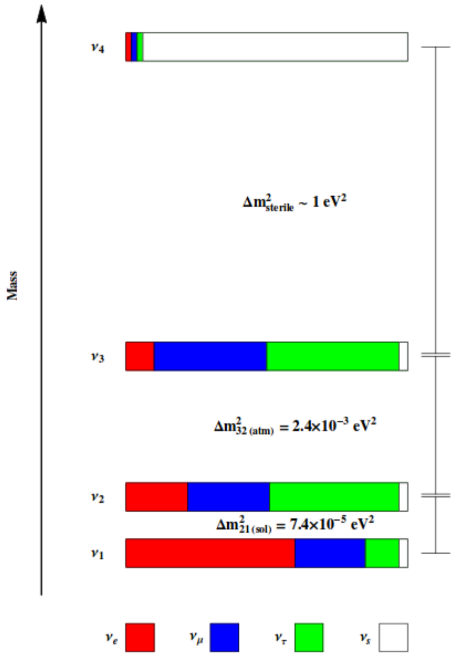

Figure 1.8: Schematic illustration of the 3+1 model in the framework of light sterile neutrino.

Sterile neutrinos are neutral leptons that do not interact weakly with the W and Z bosons but participate to the mixing phenomenon [29]. Very heavy sterile neutrinos are utilized in the minimal type I seesaw model [35–38] and play an important role in leptogenesis while light sterile neutrinos participate to the oscillations with the ordinary active neutrinos. Besides light sterile neutrinos at eV mass scale, interesting possibilities are under study: very light sterile neutrinos at a mass scale smaller than 0.1 eV which could affect the oscillations of solar and reactor neutrinos; sterile neutrinos at the keV scale, which could constitute warm dark matter according to the Neutrino Minimal Standard Model (νMSM) [39]; sterile neutrinos at the electroweak scale or above it [40], whose effects may be seen at LHC and other high-energy colliders.

Taking into account the scenario with only light sterile neutrinos, the minimal scheme which can explain the anomalies in neutrino sector found in some short-baseline experiments is the so called “3+1” model, which includes 3 active neutrinos ν_e, ν_μ and ν_τ plus a fourth sterile neutrino ν_s. As shown in Fig 1.8, in this model the mass spectrum of neutrino consists of three mostly active neutrino mass eigenstates with masses m_1, m_2 and m_3 and one mostly sterile neutrino mass eigenstate with a mass m_4 1 eV greater than that of the ordinary neutrinos.

In this framework the mixing between the flavour and the mass eigenstates is described by generalizing the PMNS matrix to a 4×4 unitary matrix, $U^{(4)}$, which can be parametrized by six mixing angles and 3 CP violation phases:

$$U = R_{34}(\theta_{34})R_{24}(\theta_{24})R_{23}(\theta_{23}, \delta_3)R_{14}(\theta_{14})R_{13}(\theta_{13}, \delta_2)R_{12}(\theta_{12}, \delta_1) \quad (1.25)$$

where $R_{ij}(\theta_{ij})$ $(i, j = 1, ...4$ and $i > j)$ is the 4×4 rotation matrix in the ij plane with angle θ_{ij}. Therefore there are 6 new mixing parameter: 3 mixing angle θ_{14}, θ_{24}, θ_{34} which quantify, respectively, the $\nu_s - \nu_e$, $\nu_s - \nu_\mu$ and $\nu_s - \nu_\tau$ mixings; one new mass squared difference $\Delta m^2_{41} = m^2_4 - m^2_1$ and 2 CP violation phases δ_{14} and δ_{24}.

Since the sterile neutrinos hypothesis should be compatible with the results of 3 neutrino scenario, the mass squared differences have to satisfy the following condition:

$$\left|\Delta m^2_{21}\right| << \left|\Delta m^2_{31}\right| << \left|\Delta m^2_{41}\right| \quad (1.26)$$

Another assumption to be done in order to do not affect standard oscillations is to consider that the new mass state is mostly sterile:

$$\left|U^{(4)}_{e4}\right|^2, \left|U^{(4)}_{\mu 4}\right|^2, \left|U^{(4)}_{\tau 4}\right|^2 << 1, \quad \left|U^{(4)}_{s4}\right|^2 \simeq 1 \quad (1.27)$$

In this way their mixing with the three active neutrinos is sufficiently small to be negligible in the analysis of the data of current experiments.

The oscillation probability of neutrinos in vacuum is similar to Eq. 1.13, replacing the PMNS matrix with $U^{(4)}$. In short-baseline experiments $\Delta m^2_{41} = \Delta m^2_{SBL}$ and $\Delta m^2_{41} L/4E \sim 1$, the transition and survival probabilities can be written as:

$$\begin{aligned} P^{SBL}_{\nu_\alpha \to \nu_\beta} &\simeq sin^2 2\theta_{\alpha\beta} sin^2 \left[\frac{\Delta m^2_{41} L}{4E}\right] \quad (\alpha \neq \beta) \\ P^{SBL}_{\nu_\alpha \to \nu_\alpha} &\simeq 1 - sin^2 2\theta_{\alpha\alpha} sin^2 \left[\frac{\Delta m^2_{41} L}{4E}\right] \end{aligned} \quad (1.28)$$

with the transition and survival amplitudes:

$$\begin{aligned} sin^2 2\theta_{\alpha\beta} &= 4\left|U_{\alpha 4}\right|^2 \left|U_{\beta 4}\right|^2 \quad (\alpha \neq \beta) \\ sin^2 2\theta_{\alpha\alpha} &= 4\left|U_{\alpha 4}\right|^2 (1 - \left|U_{\alpha 4}\right|^2) \end{aligned} \quad (1.29)$$

and with the appearance-disappearance constraint

$$sin^2 2\theta_{\alpha\beta} \simeq \frac{1}{4} sin^2 2\theta_{\alpha\alpha} sin^2 2\theta_{\beta\beta} \quad (\alpha = e, \mu, \tau) \quad (1.30)$$

The transition and survival probabilities in Eq. 1.28 depend only on the largest squared-mass difference Δm^2_{41} and on the absolute values of the elements in the fourth column of the mixing matrix. The transition probabilities of neutrinos and antineutrinos are equal, because the absolute values of the elements in the fourth column of the mixing matrix do not depend on the CP-violating phases in the mixing matrix.

Others possible framework have been theorized such as the 2+2 and the 3+2 models. The former foresees the existence of two pairs of neutrinos with similar masses separated by a gap and is ruled out at a very high confidence level [41], while the latter considers that there are two non-standard massive neutrinos at the eV scale.

1.5 An experimental approach to the search for sterile neutrinos

In 2011 an experimental search for sterile neutrinos beyond the Standard Model with a CERN-SPS neutrino beam was proposed by the ICARUS-NESSiE Collaboration [42,43]. The proposal foresaw a short baseline neutrino experiment based on two identical LAr-TPC followed by magnetized spectrometers, observing the electron and muon neutrino events at the far and near positions, respectively 1600 and 300 m from the proton target. The ICARUS T600 LAr-TPC should have been placed at the far position, while an additional T150 LAr-TPC (with a volume of 1/4 with respect to the T600) should have been constructed and placed at the near position. Downstream of each Lar-TPC detector, should have been put two spectrometers in order to measure with high precision the charge and the momentum of muons produced by ν_μ CC interactions in the LAr target and those interacting in the spectrometer itself.

This experimental approach was intended to study $\nu_\mu \rightarrow \nu_e$ oscillations in both beam polarity, providing both ν_μ and ν_e measurements in CC and NC process. In absence of oscillations, the ν_e spectrum distributions must be identical at far and near site. Any difference of the event distributions at the locations of the two detectors might be due to the fact that the ν_μ oscillated into a sterile neutrino with a mixing angle $\sin^2(2\theta_{new})$ and a squared mass difference Δm^2_{new}. In particular, the technique of the LAr imaging TPC allows to identify very well ν_e interactions, making possible to study ν_e appearance signals. On the other hand, the use of spectrometers allows the full separation of ν_μ from $\overline{\nu}_\mu$. In the negative beam polarity the rate of ν_μ interactions is a sizeable fraction of $\overline{\nu}_\mu$ interactions and therefore the identifications of ν_μ and $\overline{\nu}_\mu$ events at the near detector allows to reduce the systematic errors associated with the predictions of ν_μ and $\overline{\nu}_\mu$ fluxes at far detector. Such a measure is also crucial for the observation of any difference between $\nu_\mu \rightarrow \nu_e$ and $\overline{\nu}_\mu \rightarrow \overline{\nu}_e$ transitions, as a possible signature of CP violation.

All sterile neutrino models predict large ν_μ disappearance effects together with ν_e appearance/disappearance. To fully constrain the oscillation searches, the ν_μ disappearance studies have to be addressed in order to put severe

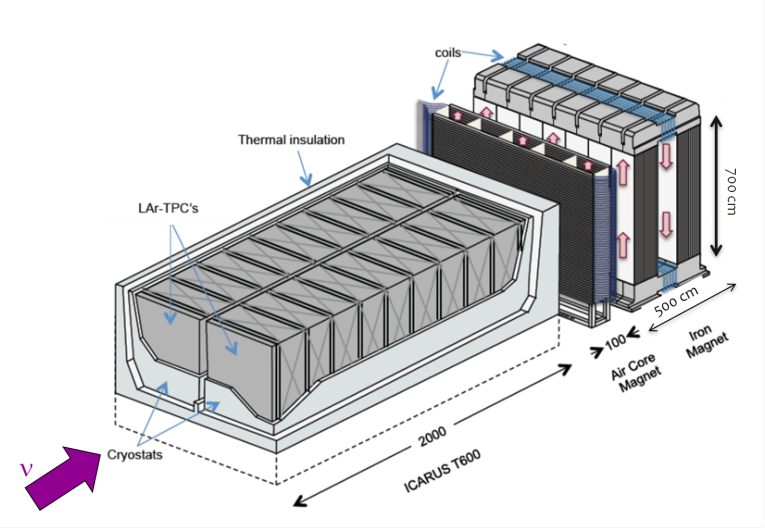

Figure 1.9: A sketch of the ICARUS-NESSiE far detector. The ICARUS Lar-TPC is followed by two spectrometers placed downstream, an Air Core Magnet and an Iron Core Magnet.

constraints to sterile neutrinos model, or to provide a confirmation in case of signal observation. For this purpose, the NESSiE spectrometers would have allowed to detect CC ν_μ ($\overline{\nu}_\mu$) disappearance signal, namely the rates of CC ν_μ events at near (CC$_{near}$) and far (CC$_{far}$) detectors. Thanks to the capability of the LarTPC to measure NC interactions, a strong evidence of NC disappearance signal can be given by the double ratio:

$$\frac{\frac{CC}{NC}_{near}}{\frac{CC}{NC}_{far}} \tag{1.31}$$

The spectrometers consisted of a light air-core magnet (ACM) followed by an iron-core magnet (ICM) as shown in Fig. 1.9. The ICM is dedicated to the reconstruction of the momentum and charge of high energy muons (up to 30 GeV) through the range measurement. Simulations have shown that up to 3.5 GeV/c the resolution is about 5 % for muon momentum measured by the ICM, while for momentum greater than 3.5 GeV/c the resolution obtained analyzing the curvature either in the ICM or the ACM increase to 30 % as shown in Fig. 1.10 (a). For low momentum muons the effect of multiple scattering in iron is comparable to the magnetic bending and therefore the charge mis-identification increase. For this reason also a light spectrometer with an air magnetized volume (ACM) was devised for the reconstruction of the charge and momentum of muons with energy less than 1 GeV. The ACM spectrometer includes a precise tracking system with a spatial resolution of 1-2 mm which is required in order to achieve a charge mis-ID of about 1 % at 1 GeV/c (see Fig. 1.10 (b)).

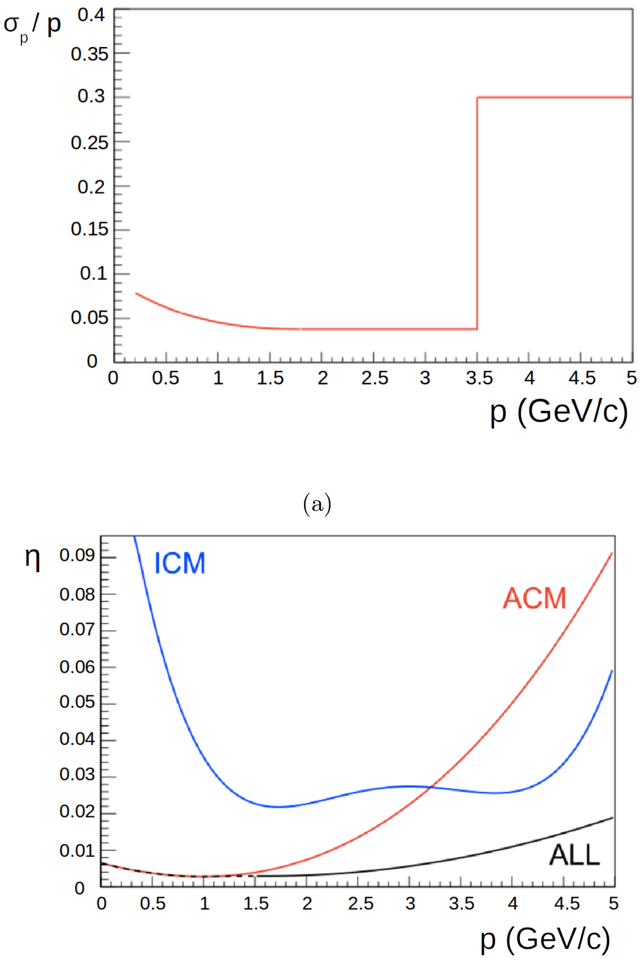

(a)

(b)

Figure 1.10: (a) Resolution on muon momentum: up to 3.5 GeV/c the resolution is about 5 % for muon momentum measured by the ICM, while for momentum greater than 3.5 GeV/c the resolution obtained analyzing the curvature either in the ICM or the ACM increase to 30 %. (b) Sensitivity to the charge mis-identification η as a function of the momentum of muons produced in ν_μ CC interactions: the blue line corresponds to the charge mis-ID taking into account only the ICM, red line is for the ACM part and black line results from the combination of the two magnetic systems which allow to achieve a mis-ID below 2% up to 5 GeV muon momentum.

1.5.1 The light magnetic spectrometer

The proposed light spectrometer is made of 39 Aluminum coils, 72×72 mm^2 cross section with a circulating 2 A/mm^2 current density generating a magnetic field of 0.12 T in an air volume 1.3 m deep [44]. This choice was considered because the coil design has not only to fulfil the magnetic, structural and thermal requirements but also to take into account the ne-

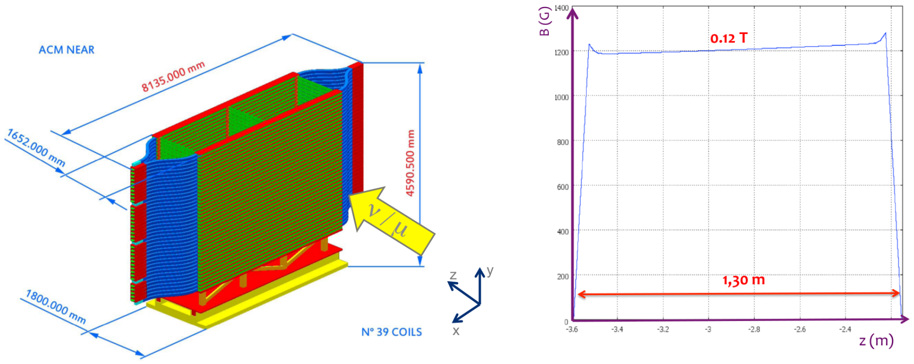

(a) (b)

Figure 1.11: (a) A sketch of the Air Core Magnet for the near site. The neutrino beam propagates along the z direction. (b) The magnetic field in the ACM volume along the z beam axis.

cessity of having minimal material in the beam direction. Moreover, using an air magnetized volume, the only dead material along the muon path is given by the conductor coils. In Fig. 1.11 (a) and (b) are shown the ACM spectrometer and the magnetic field along the beam direction, respectively.

In order to track particle trajectories in the magnetic field, the ACM is instrumented with a tracking system, as shown in Fig. 1.12 (a), with a millimetric spatial resolution. The tracking system is made of planes of scintillator bars with WaveLength Shifter (WLS) fibers (see Fig. 1.12 (b)) coupled to Silicon Photomultipliers (SiPM) read in analog mode. The solid polystyrene scintillator bar detectors were produced through extrusion by FNAL [45] and have a triangular profile with a height of (17.0 ± 0.5) mm and a width of (33.0 ± 0.5) mm. In the middle of the bar there is an hole with a diameter of (2.6 ± 0.2) mm used to lodge the WLS fiber. These scintillator detectors were previously used in several experiments for particle physics [22, 46–52]. SiPM detectors were chosen thanks to their features like single photon detection, reduced size, low power consumption and insensitivity to magnetic fields [53], which make them excellent candidates in replacing standard photomultipliers.

The momentum is determined evaluating the track curvature in the magnetic field, measuring the track sagitta thanks to the high accuracy position reconstruction.

In this thesis are reported and discussed the R & D studies carried on for the implementation of the tracking system which demonstrates the capability of reconstruct particle tracks with a spatial resolution of 1-2 mm required for the separation of μ^+ and μ^- events produced in CC ν_μ and CC $\overline{\nu}_\mu$ interactions and the determination of their momentum.

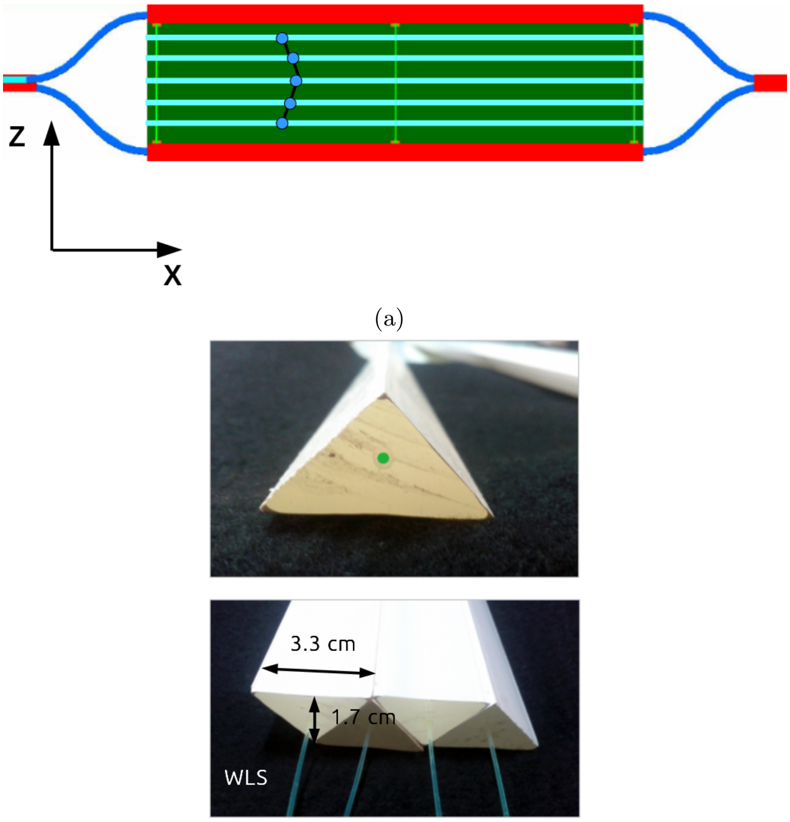

(a)

(b)

Figure 1.12: (a) A $x - z$ view of the ACM with the internal detector planes made of scintillator bars. The particle position is reconstructed in each plane with a spatial accuracy of 1-2 mm. (b) A picture of the adjacent triangular shape scintillator bars with the WLS fibers.

Chapter 2

Scintillation detectors and Silicon Photomultipliers

2.1 Passage of radiation through matter

Charged particles moving through matter interact with its components producing excitation or ionization of the material's atoms, leading to energy loss of travelling particles. The passage of charged particles through matter is characterized by two processes: inelastic collisions with atomic electrons which leads to energy loss and elastic scattering from nuclei that deflect the particle's path. Inelastic collisions with atomic electrons are responsible for the energy loss of heavy particles such as muons, pions, protons, alpha particles and other light nuclei. High energy electrons predominantly lose energy in matter by bremsstrahlung, and high energy photons by e^+e^- pair production. Inelastic collisions can be divided into soft collisions, in which only excitations occur, and hard collisions in which sufficient energy is transferred to atomic electrons, thus leading to ionization. If the transferred energy is sufficient for atomic electrons to be ejected a secondary ionization occurs; recoil electrons are called $\delta-$rays or knock-on electrons.

The rate of energy loss, or stopping power, is given by the Bethe-Bloch equation:

$$-\frac{\mathrm{d}E}{\mathrm{d}x} = 4\pi N_A r_e^2 m_e c^2 z^2 \frac{Z}{A}\frac{1}{\beta^2}\left(\frac{1}{2}\ln\frac{2m_e c^2\beta^2\gamma^2 T_{max}}{I^2} - \beta^2 - \frac{\delta(\beta\gamma)}{2}\right) \quad (2.1)$$

where N_A is the Avogadro's number, r_e is the classical electron radius, m_e is the electron mass at rest, z is the charge of the incident particle, Z is the atomic number of the absorber, A is the atomic mass, $\beta = v/c$ is the velocity of the particle expressed in multiples of the velocity of light c, $\gamma = 1/\sqrt{(1-\beta^2)}$ is the Lorentz factor and $\delta(\beta\gamma)$ is the density effect correction to ionization energy loss. The stopping power of muons in copper is shown in Fig. 2.1 as a function of the momentum. Particles with $\beta = 0.96$

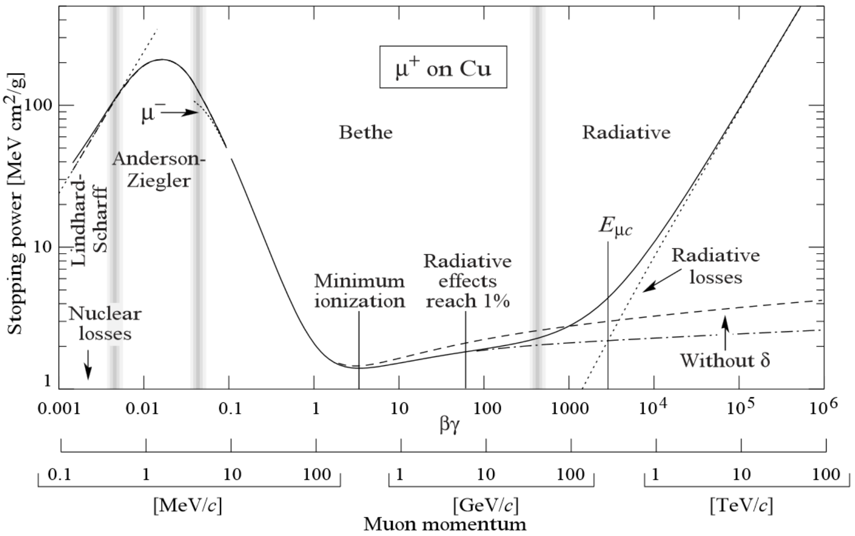

Figure 2.1: The rate of energy loss (-dE/dx) expressed by the Bethe-Bloch equation for muons in copper as a function of $\beta\gamma = p/Mc$.

have mean energy loss rates close to the minimum of the Bethe-Bloch function; they are referred as minimum ionizing particle (m.i.p.). For a m.i.p. the stopping power is weakly dependent on its momentum, therefore an even distribution of free charge carriers along its paths is produced. Thanks to this feature, m.i.p. are excellent candidates to test and study detectors since they give an almost uniform response along their path.

The phenomenon of particle energy loss is largely exploited in many particle physics devices such as scintillator detectors and silicon sensor described in the following sections.

2.2 Scintillation detectors

Scintillator detectors are widely used since a long time in many particle physics experiments. Scintillation materials convert particles' energy loss into photons, i. e. scintillation light. This process is called *luminescence*. When the emission of light occurs within 10^{-8} sec after the absorption of the particle energy, the process is called *fluorescence*. If the emission of the light is delayed the process is called *phosphorescence* or *afterglow*.

The number of photons N emitted in the scintillation process can be expressed by the formula:

$$N = Ae^{-\frac{t}{\tau_f}} + Be^{-\frac{t}{\tau_s}} \tag{2.2}$$

where τ_f and τ_s are the decay constants, corresponding to the fast (prompt) and slow (delayed) components, respectively. A and B are their relative

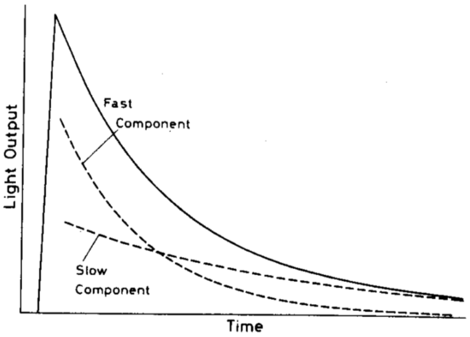

Figure 2.2: Light output N as a function of time (solid line). It consists of a combination of a fast and a slow component (dashed lines).

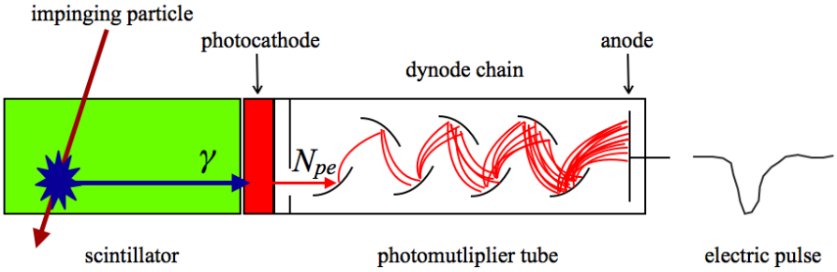

Figure 2.3: Scintillator detector coupled to a photomultiplier tube.

magnitude which vary from material to material. The light output N as a function of time follows an exponential decay shown in Fig. 2.2 (solid line), which is a combination of fast and slow components (dashed lines) [54].

By coupling a scintillator detector to a photodetector as shown in Fig. 2.3, the scintillation light can be converted into electrical pulses which provide information on the incident particle. In the sketch shown in Fig. 2.3 the scintillation light produced by the impinging particle is transmitted to a photomultiplier tube (PMT). Scintillation photons reaching the photocathode excite its electrons by the photoelectric effect, thus N_{pe} photoelectrons (p.e.) are emitted in the vacuum tube. By an electric field the photoelectrons are accelerated and focused onto a series of dynode inducing electron multiplication by secondary emissions. Electrons are collected by the anode yielding thus an electrical amplified pulse.

Above a minimum energy of the travelling particle, the scintillator light output is directly proportional to the energy lost by the particle ($L \propto E$). Since conventional amplification devices, such as silicon photodetectors, work mainly in a linear regime, the amplitude of the electrical signal is proportional to the energy deposited by the impinging particle.

In many applications, the linearity between the light output and the deposited energy is a good approximation. In reality, the response of scintillators is a complex function of not only the energy but also of the type of particle and its specific ionization. The light output can be expressed by the Birk's formula when non linear effects are taken into account:

$$\frac{\mathrm{d}L}{\mathrm{d}x} = \frac{A\frac{\mathrm{d}E}{\mathrm{d}x}}{1 + kB\frac{\mathrm{d}E}{\mathrm{d}x}} \tag{2.3}$$

where $\mathrm{d}L/\mathrm{d}x$ is the light output per unit length, A is the absolute scintillation efficiency, kB is a parameter relating the density of ionization centers to the energy loss $\mathrm{d}E/\mathrm{d}x$. The Birk's model explains deviations from linearity as being due to quenching interactions of excited molecules along the path of incident particle. A particle with a higher ionizing power produces a higher density of excited molecules, thus more quenching interactions will take place for these particles carrying away energy that would otherwise go into luminescence. A better fit of the data is:

$$\frac{\mathrm{d}L}{\mathrm{d}x} = \frac{A\frac{\mathrm{d}E}{\mathrm{d}x}}{1 + kB\frac{\mathrm{d}E}{\mathrm{d}x} + C\left(\frac{\mathrm{d}E}{\mathrm{d}x}\right)^2} \tag{2.4}$$

Such higher order formulae reduce to a linear relationship for small dE/dx:

$$\frac{\mathrm{d}L}{\mathrm{d}x} = \frac{\mathrm{d}E}{\mathrm{d}x} \tag{2.5}$$

For large dE/dx, Birk's formula implies saturation:

$$\frac{\mathrm{d}L}{\mathrm{d}x} \simeq \frac{A}{kB} \tag{2.6}$$

Experimentally all these formulae have been shown to be incomplete because of some further dependence of $\mathrm{d}L/\mathrm{d}x$ on the particle type in addition to $\mathrm{d}E/\mathrm{d}x$.

As a good detector, scintillators should satisfy the following conditions:

- high efficiency for the conversion of the exciting energy to fluorescent radiation, namely high light yield; which determines also the energy resolution of the scintillator;
- transparency to its fluorescent radiation;
- short decay constant τ;
- emission in a spectral range consistent with the spectral response of a coupled photodetector.

The last requirement can be solved also by optically coupling the scintillator to the photodetector through WLS fibers which absorb the scintillation light and re-emit it at a wavelength better matching with the photodetector sensitivity.

An important characteristic of scintillators is the attenuation length λ of the light response, namely the length where the light intensity is reduced by a factor $1/e$. The light intensity as a function of the length is:

$$L(x) = L_0 e^{\left(\frac{-x}{\lambda}\right)} \tag{2.7}$$

where x is the path travelled by the light and L_0 the initial light intensity. The attenuation length is a parameter that describes the loss of light through absorption by the scintillator material. For small detectors, this effect is negligible. Only when the dimensions of the detector are such that the total path lengths travelled by the photons are comparable to the attenuation length, the absorption process plays an important role.

Another significant source of light loss is the transmission through the boundaries of the scintillator. In plastic scintillators the total internal reflection is facilitated by polishing their surfaces. Another common procedure is to wrap in aluminium foil or to cover the scintillator surfaces with a reflective paint as Titanium dioxide (TiO_2) or Magnesium oxide (MgO) pigments.

There are several types of scintillation material such as organic crystals, organic liquids, plastics, inorganic crystals, gases and glasses. In the following are described the scintillators used in the context of this thesis.

2.2.1 Organic scintillators

Organic scintillators are divided into three categories: crystals, liquids and plastics. They are aromatic hydrocarbon compounds containing condensed benzene-ring structures. Organic scintillators have a low light yield with respect to inorganic scintillators but have a fast decay time of few nanoseconds or less.

The scintillation light in organic compounds arises from transitions made by free valence electrons of the molecules. The energy deposition from a charged particle passing through the material excites the electrons from the ground state to higher states. These delocalized electrons are not associated with any particular atom in the molecule and occupy a π*-molecular orbitals*. A typical energy diagram for these orbitals in which spin singlet states are distinguished from spin triplet states is shown in Fig. 2.4. At room temperature all electrons are in the ground state denoted as S_0. Incident radiation populates both the excited electron singlet states (S_1, S_2,...) and the vibrational states. Vibrational levels decay in a time $<$ 10 ps to the base state S_1 without the emission of radiation; this process in known as *internal degradation*. Electrons from the state S_1 have a high probability of making

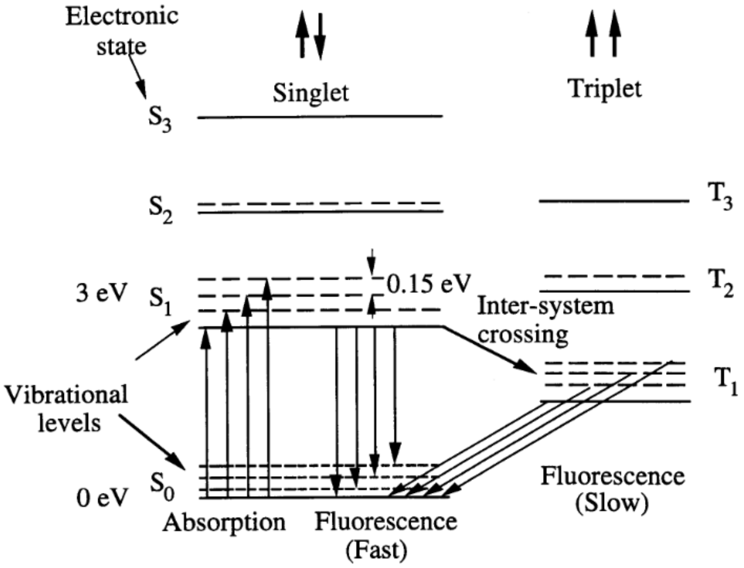

Figure 2.4: Energy level diagram of an organic scintillator molecule.

a radiative decay to one of the vibrational states of the ground state S_0 within few nanoseconds. This light emission, associated with the fluorescence process, is described by the fast exponential component of Eq. 2.2. The fact that S_1 decays to excited vibrational states of S_0 with emission of radiation energy smaller than that required for the transition $S_0 \rightarrow S_1$ ensures the transparency of the scintillator to the light emitted. S_1 can also decays to adjacent triplet levels T_1 through *inter-system crossing.* A molecule in the state T_1 can interact with another molecule in the same state:

$$T_1 + T_1 \rightarrow S_1 + S_0 + phonons \tag{2.8}$$

One of the molecules is left in the excited state S_1 which then decays as described previously. The resulting light emission has a delay time ($> 10^{-4}$ s) characteristic of the interaction between excited molecules. This light is associated with the phosphorescence process and is described by the slow exponential component of Eq. 2.2.

2.2.1.1 Plastic scintillators

Plastic scintillators are solutions of organic materials dissolved in a solvent that can be polymerized. Typical plastic materials used are polystyrene (PS), polyvinyltoluene (PVT), or polymethylmethacrylate (PMMA). Some common primary solutes are PBD[1], p-Terphenyl[2] and polybenzoxazole

---

[1] 2-phenyl,5-(4-biphenylyl)-1,3,4-oxadiazole ($C_{20}H_{14}N_20$)

[2] $C_{18}H_{14}$

(PBO). A secondary solute POPOP[3] is also added for its wavelength shifting properties [54]. Plastic scintillators are realized with relatively inexpensive materials, they can easily be fabricated and shaped. They can produce an extremely fast signal with a decay constant of about 2-3 ns and a high light output. For these reasons they are often the best practical choice for the realization of large scintillator detectors.

The light output of plastic scintillators is described by Bengston and Moszynski formula:

$$N(t) = N_0 f(\sigma, t) e^{\frac{-t}{\tau}} \tag{2.9}$$

where $f(\sigma, t)$ is a Gaussian with a standard deviation σ.

In many detector applications, plastic scintillators consist of binary and ternary solutions of *fluors* in a plastic base. Ionization in the plastic base produces UV photons with a short attenuation length ($\sim$ few mm). Longer attenuation lengths can be obtained by dissolving a primary fluor in high concentration (about 1%) into the base. The fluor is selected in order to efficiently re-radiate the absorbed energy at wavelengths where the base is more transparent. The fluor has an absorption and emission spectra shifted: the two distributions have a certain overlapping and the wavelength difference between the absorption and emission peaks is called the Stoke's shift. The greater this shift is, the smaller the overlapping and therefore the self-absorption. The other function of the fluor is to shorten the decay time and to increase the total light yield. It is often necessary to add a secondary fluor or even a third one, at a fraction percent levels, in order to shift light to longer wavelengths that better match the region of maximum sensitivity of the photodetectors [55].

2.3 Silicon Photodetectors

Silicon photodetectors are semiconductor devices that convert optical signals into electrical ones. These devices consist of a $p-n$ junction. In a $p-n$ junction electrons diffuse from the n-side to the p-side and the holes diffuse from the p-side to the n-side. The charges flowing from one side to the other, lead to the formation of a built-in electric field near the junction zone of opposite direction with respect to the carrier diffusion thus stopping the diffusion itself. If no external bias voltage is applied to the semiconductor, an equilibrium condition is reached: near the junction electrons in the p-side combine with holes to form negative ions leaving behind positive ions in the n-side. In this way a space charge builds up, creating a *depletion region* which inhibits any further electron transfer. Within the depletion region, there are very few mobile electrons and holes. Fig. 2.5 shows the basic principle of the pn junction. At the thermal equilibrium, the width W of

---

[3] 1,4-Bis-[2-(5-phenyloxazolyl)]-benzene ($C_{24}H_{16}N_2O_2$)

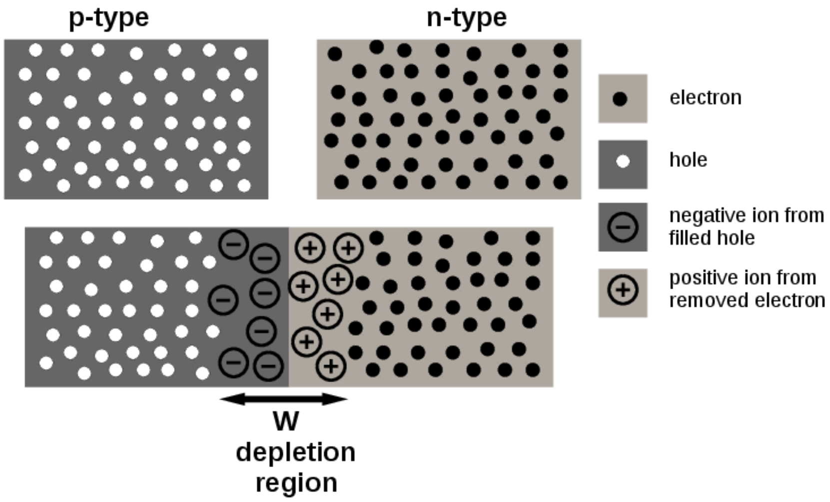

Figure 2.5: A $p-n$ junction.

the depletion region depends mainly on the doping concentration of the p and n zones according to:

$$W = \sqrt{\frac{2\epsilon_s}{q}\left[\frac{N_A + N_D}{N_A N_D}\right] V_{bi}} \tag{2.10}$$

where N_A is the number of acceptor p-ions, N_D is the number of donor n-ions, ϵ_s is the semiconductor dielectric permittivity and V_{bi} the electrostatic potential across the junction (*built-in* potential) defined as:

$$V_{bi} = \frac{kT}{q} ln \frac{N_a N_D}{n_i^2} \tag{2.11}$$

where k is the Boltzman's constant, q is the electric charge and n_i is the intrinsic concentration of carriers [56].

If an external voltage is applied to the junction, the system is no longer at equilibrium and the depletion zone is modified. If a positive voltage is applied to the p-type side and a negative voltage to the n-type side, a current can flow (*forward biased*). The built-in electric field is opposite to the applied electric field, thus the resultant field at the junction is smaller than the original built-in electric field. This results in a thinner, less resistive depletion region (see Fig. 2.6 (a)). If a negative voltage is applied to the p-type side and a positive voltage to the n-type side, no current flows (*reverse biased*). At the $p-n$ junction the applied electric field and the built-in electric field have the same direction, thus the resultant field at the junction is larger than the original built-in electric field. This results in a thicker, more resistive depletion region (see Fig. 2.6 (b)). In reality, some current

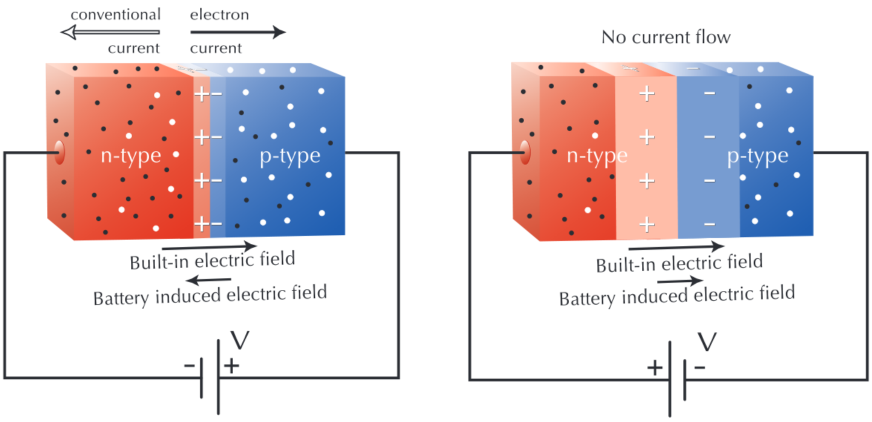

(a)
(b)

Figure 2.6: (a) A $p-n$ junction in the forward biased configuration. (b) A $p-n$ junction in the reverse biased configuration.

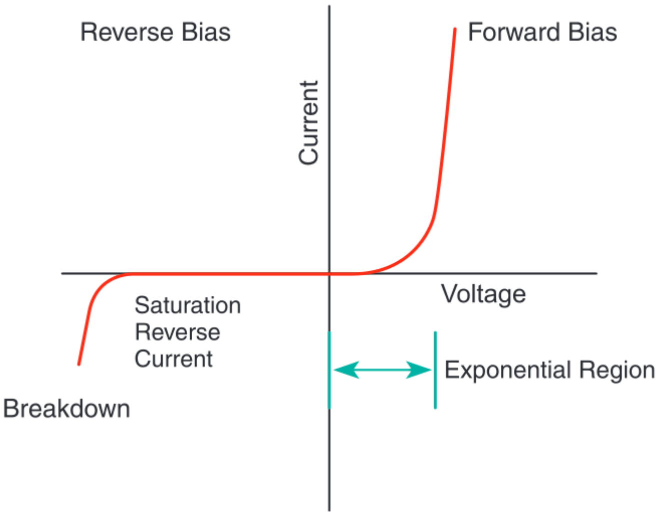

Figure 2.7: I-V curve of a $p-n$ junction.

will still flow through the junction, but the resistance is so high that the current may be considered to be zero. As the reverse bias voltage becomes larger, the current flow will saturate at a constant small value. This is called inverse saturation current and is approximately 10^{-12} A/cm^2 of the $p-n$ junction area.

The current voltage relation, namely the I-V curve (shown in Fig. 2.7), correlates the voltage V applied to the $p-n$ junction with the resulting current I. In reverse bias, the $p-n$ junction exhibits extreme electrical resistance and only a very small current flows due to electron-hole pairs continuously generated by thermal excitations. This behaviour is taken into account in the following formula [57]:

$$I = I_S\left(e^{\frac{V}{nV_T}} - 1\right) \tag{2.12}$$

where V is the applied voltage, $V_T = \frac{kT}{e}$ is the thermal voltage[4], n is the quality factor which varies from 1 to 2 depending on the diode manufacturing process and I_S is the inverse saturation current. If the reverse bias voltage becomes too large then the junction breaks-down and current flows. The *breakdown voltage* V_{bd} corresponds to the start of the uncontrolled multiplication process which is the basic mechanism of avalanche photodetectors like Silicon Photomultipliers. In forward bias, the $p-n$ junction exhibits an exponential lowering of resistance with applied voltage. From 0 to 0.5 V, the silicon $p-n$ junction is high resistive and no current flows through the junction. When the applied voltage approaches 0.6 V ($V >> V_T$, and $exp(V/nV_T) >> 1$) the resistance drops significantly and the current I starts flowing in the junction following an exponential law:

$$I = I_S e^{\frac{V}{nV_T}} \tag{2.13}$$

The basic principle of the photodetection is the photoelectric effect: electron-hole pairs can be produced inside the depleted region by light if the energy of the impinging photons is large enough to bring the electron from the valence band to the conduction band. Applying an external electric field, it is possible to collect the photo-carriers created by light by an external circuit. The responsivity R is the ratio of the photocurrent I_{ph} flowing in the photodetector over the incident optical power P_{in}:

$$R = \frac{I_{ph}}{P_{in}} \tag{2.14}$$

The responsivity can be written also as:

$$R = \frac{q\eta}{h\nu} = \eta\frac{\lambda}{1.24} \tag{2.15}$$

where q is the electron charge, $\nu = hc/\lambda$ is the frequency of the light and η is the Quantum Efficiency (QE). QE is defined as the ratio of photons hitting the sensitive area of the photodetector which produce an electron-hole pair over the total number of impinging photons. QE depends on the structure of the junction: the undepleted layer should be thin enough for short-wavelength photons to be transmitted and the depleted layer should be thick enough to allow the absorption of long-wavelength photons. If we consider a photoconductor of thickness d, neglecting reflections at the interface, the quantum efficiency can be expressed as:

$$\eta = \eta_c\left(1 - e^{-\alpha d}\right) \tag{2.16}$$

---

[4] $V_T = T/11600$, at room temperature (T = 25 °C) V_T is 26 mV

where α is the absorption coefficient, η_c is the collection efficiency, namely the percentage of carriers generated and contributing to the photocurrent.

The quantum efficiency describes the efficiency of conversion from optical photons to pairs, but this value does not represent the detection efficiency of the whole device. This parameter is represented by PDE, which is the probability that an impinging photon is detected by the photodetector. The PDE definition varies according to the different types of photodetectors.

Another important parameter that characterizes photodetectors is the gain G, i.e. the multiplication factor of photodetectors working in avalanche or in Geiger-Müller regime.

There are different type of photodetectors described in the following: pn diodes, pin diodes and Avalanche PhotoDiodes.

2.3.0.2 pn diodes

pn photodiodes are operated under reverse bias conditions. In this configuration the electric field within the depletion region is so high that electron-hole pairs created by an impinging photon drift with a fast transit time $\tau_{tr} < 100$ ps. When the carriers reach the p and n regions the motion is characterized by diffusion processes and the transit time becomes slower, $\tau_{tr} < 10$ ns. For this reason the p and n regions should be as small as possible, while the depth of the depletion region should be as thick as possible in order to reduce the diffusion time. In *pn* diodes the thickness of the depletion region d is < 10 μm, leading to low QE and slow diffusion time. A solution is represented by *pin* diodes.

The PDE of single pixel non-amplifying photodetectors, like *pn* and *pin* diodes, is equal to the QE of the device (typically QE is $\sim 90\%$) [58], multiplied by the inverse of the recombination probability of the carriers during the drift.

2.3.0.3 pin diodes

pin photodiodes consist of an intrinsic i (undoped) piece of ohmic semiconductor sandwiched between two heavily doped $n+$ and $p+$ regions. In this way a wide depletion region with high uniform electric field is formed between the p and n regions, as shown in Fig. 2.8. This electric field helps in speeding up of the transport of charge carriers from p to n region, which results in faster operation of the diode, making it a suitable device for high frequency operations.

The gain is ~ 1 both for *pn* and *pin* diodes.

2.3.0.4 Avalanche PhotoDiodes

Avalanche PhotoDiodes (APD) are used to measure very low photocurrent since they have very high gain compared to *pn* and *pin* diodes. APD are

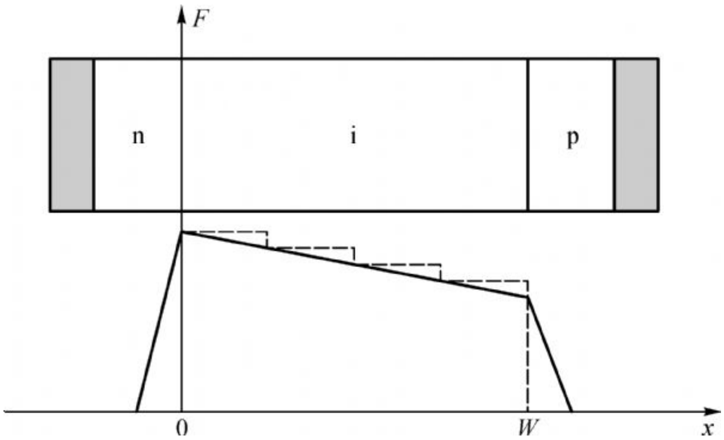

Figure 2.8: Scheme of a *pin* diode (top) and the intensity of the electric field F in the different regions of the diode (bottom).

particular types of *pn* diodes reverse biased near the breakdown voltage working in the charge multiplication regime. The multiplication factor is moderate and varies between 50 and 1000. In Fig. 2.9 (a) is sketched the structure of an avalanche photodiode. APD consists of a $p+$ heavily doped region, an intrinsic i region, a p region and a $n+$ heavily doped region. The p region placed in ohmic contact with the intrinsic region generates a very high electric field within the small p region. The electrons generated in the i region impact in the p region before reaching the $n+$ side, thus leading to a high acceleration of the electrons which have enough kinetics energy to produce secondary electrons through impact ionization process. This mechanism leads to the generation of carriers multiplication regime, namely an avalanche, which is shown in Fig. 2.9 (b).

The PDE of an APD is equal to the QE (typically QE is $\sim 85\%$) multiplied by the avalanche trigger probability. Two avalanche trigger probabilities can be defined, one for the electrons and one for the holes, where the first is usually larger.

2.4 Silicon Photomultipliers

Silicon Photomultipliers are single photon sensitive devices built from an avalanche photodiode array on common Si substrate. Each APD, called *pixel* or *microcell*, is biased above the breakdown voltage V_{br}, working in Geiger-Müller avalanche mode and readout in parallel via a common substrate. The Geiger discharge is produced when a sufficiently high electric field ($> 5 \times 10^5$ V/cm) is generated within the depletion region of the silicon. This leads to a high gain of the device, typically G $\sim 10^6$. Each pixel is in series with a quenching resistor which limits the current (to about 10 μA) drawn by the

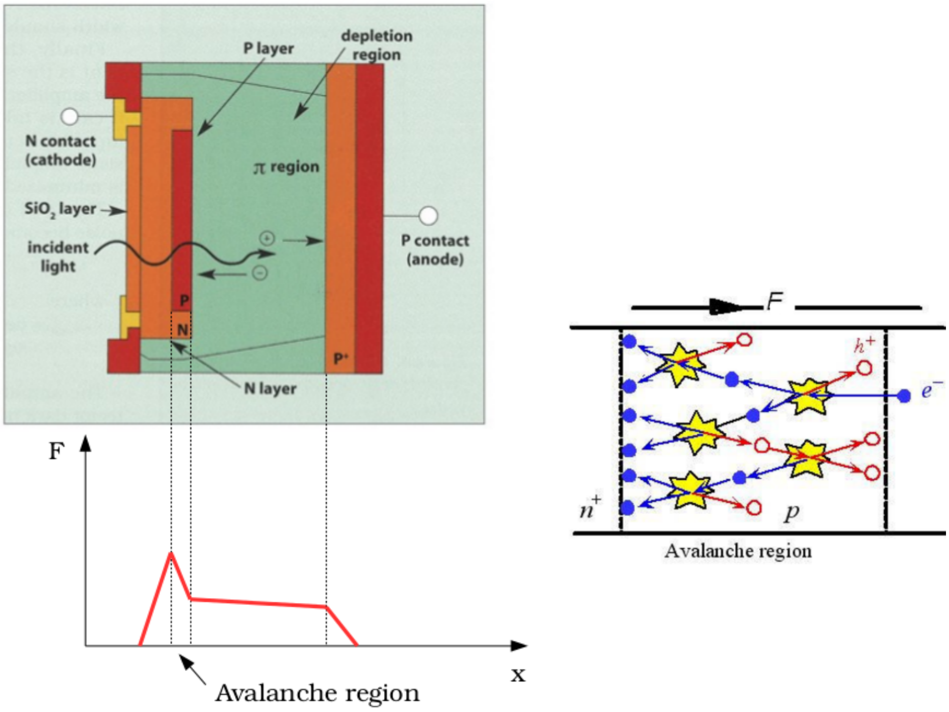

(a) (b)

Figure 2.9: (a) Sketch of an avalanche photodiode (top) and the electric field F along the junction (bottom). (b) Impact ionization process leading to the generation of an avalanche of photoelectrons.

diode during the breakdown, and hence lowers the reverse voltage to a value below the diode breakdown voltage. This cycle of breakdown, avalanche, quench and subsequent reset of the bias to a value above the breakdown voltage is illustrated in Fig. 2.10.

Each microcell detects photons independently. The sum of the discharge currents from each pixels combines to form a quasi-analog output, and is thus capable of giving information on the magnitude of an incident photon flux. A simplified electric circuit to illustrate the concept is shown in Fig. 2.11 (a) [59]. Output signals with an amplitude proportional to the number of detected photons are shown in Fig. 2.11 (b).

The development of SiPMs started at the beginning of 1960s and nowadays different devices have been developed to optimize SiPM's performance. Typically they consists of 500-4000 pixels/mm^2, with a pixel dimension in the 20-100 μm range.

The most important advantages of SiPMs are:

- insensitivity to magnetic fields. Thanks to this feature, not present in photomultiplier tubes, SiPM are used in many HEP experiments;

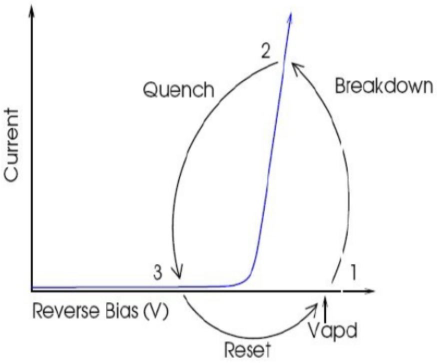

Figure 2.10: Breakdown, quench and reset cycle of a photodiode working in the Geiger mode.

- low bias voltage, usually of the order of $\sim$ 50 V;
- high gain, of the order of 10^6, comparable with PMT's one: none or very simple amplification of the output signal is thus required [60];
- compact and easy-to-handle structure;
- very small excess noise factor, due to the fact that no fluctuations in the avalanche process are present;
- sensitivity to single photoelectrons;
- low cost with respect to standard photomultiplier tubes.

The main drawbacks of these devices are large (temperature dependent) dark noise (as described in section 2.4.1) and a low radiation hardness. Bulk damage in silicon detectors caused by hadrons or higher energy leptons and photons is primarily due to displacement of primary knock-on atoms from the lattice. Irradiating a SenSL SiPM with neutrons of 1 MeV with a fluence of 3.7×10^9 particle/cm^2, the dark rate of the SiPM will increase by a factor 10 [61].

SiPMs typically operate at an over-voltage $\Delta V_{ov} = V_{bias} - V_{br}$ from 1 to 5 V over V_{br}. Like other silicon-based photodetectors, SiPMs have quantum efficiency close to 100 %. However additional contributions apart from the quantum efficiency limit the SiPM PDE $\eta(\lambda)$:

- the fill factor F or geometric efficiency, i.e. the ratio of sensitive to total area of a pixel, which depends on the gaps between the microcells;
- the probability for a photo-electron to initiate a Geiger discharge $\epsilon(V)$;

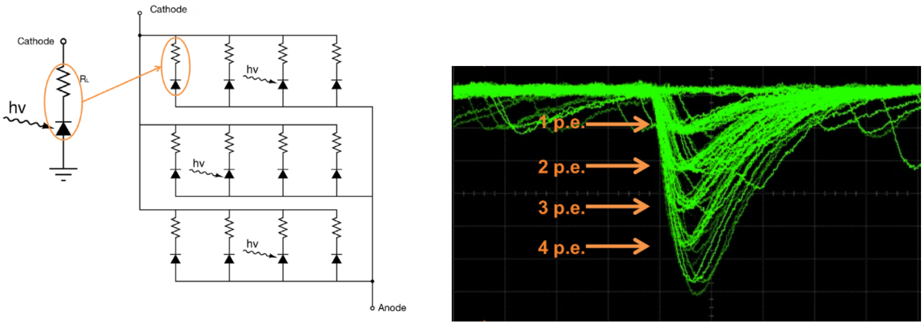

(a) (b)

Figure 2.11: (a) Electric circuit of an array of microcells (photodiode plus quench resistor) with summed output. (b) Output signals from a SiPM when illuminated by brief pulses of low-level light.

- the recovery time τ_{rec} of the pixel, defined as the microcell reset period, $\tau_{rec} = R_Q \cdot C$ in which the pixel capacitance C recharges back to V_{bias} through the quenching resistance R_Q and the microcell is ready for the detection of a new photon.

The PDE can be written as:

$$PDE(\lambda, V) = \eta(\lambda) \cdot \epsilon(V) \cdot F \tag{2.17}$$

The gain G of a microcell is the ratio of the output charge to the charge of an electron. The output charge can be calculated from the over-voltage and the microcell capacitance C as:

$$G = \frac{C\Delta V_{ov}}{q} \tag{2.18}$$

The signal of a fired pixel is linearly proportional to the capacitance of the microcell and to ΔV_{ov}. Each detected photon results in a highly quantized output pulse. If such pulses are integrated by an ADC, the peaks due to successive numbers of detected photons will be clearly visible in the spectrum shown in Fig. 2.12 (a). The separation between each pair of adjacent peaks is constant and corresponds to the charge from a single Geiger discharge. This can therefore be used to accurately calculate the gain, using equation 2.18. By repeating this procedure at different over-voltage values, the gain as a function of ΔV_{ov} can be obtained; an example is shown in Fig. 2.12 (b).

Considering the high density of cells, SiPMs are linear over a wide range of light intensities. The linearity limit is due to the finite number of cells because two or more photons that impinge on one cell produce exactly the same signal as one single photon. The dynamic range of a SiPM ranges from the lowest detectable signal, to the input signal level resulting in all SiPM microcells detecting photons simultaneously. At this point the output

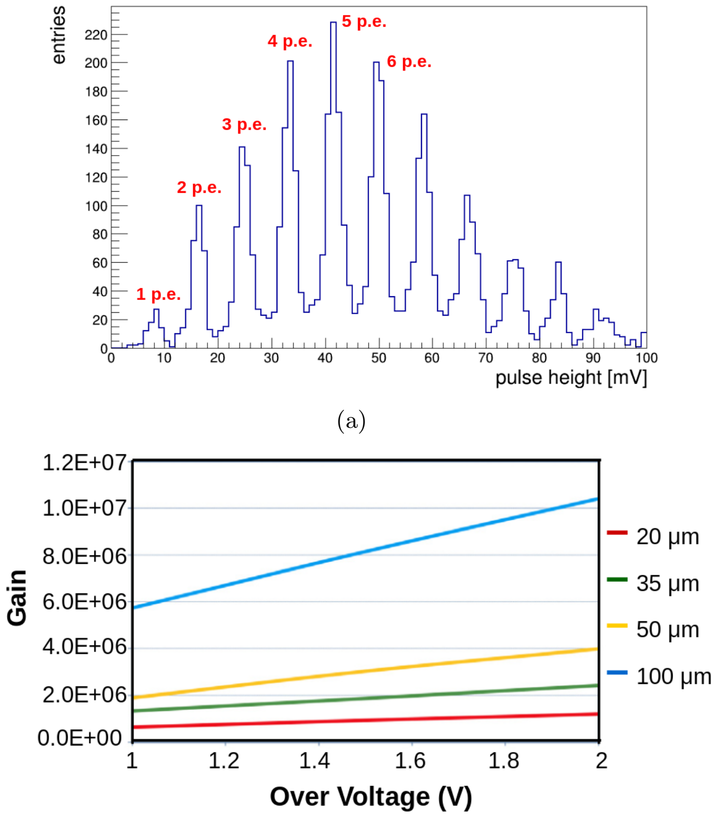

(a)

(b)

Figure 2.12: (a) Photoelectron spectrum of a SiPM illuminated by low-level light pulses. The pedestal (0 p.e.) due to eletronic noise is subtracted from the signal. (b) SiPM gain as a function of applied over-voltage for different microcell size (20 μm, 35 μm, 50 μm and 100 μm).

signal saturates since no more microcells are available to detect incoming photons, until some of the microcells have recovered back to their sensitive state. The dynamic range of a SiPM is therefore a function of the total number of microcells and of the PDE of the device. The number of fired cells N_{fired} can be written as:

$$N_{fired} = N_{tot}\left[1 - exp\left(\frac{-N_{ph} \cdot PDE}{N_{tot}}\right)\right] \tag{2.19}$$

where N_{tot} is the number of SiPM microcells, N_{ph} is the number of incident photons. Due to the finite number of available cells, deviations from linearity occur when the number of photons is comparable to the number of available pixels.

2.4.1 SiPM noise

The electronics noise of SiPMs is negligibly small due to its high gain, in contrast to standard APDs, where G is typically ~ 100. For SiPMs, the electronic noise corresponds to less than 10 % of the signal from one photoelectron [53]. The main source of noise, which limits the SiPM's single photon resolution is the dark current. Other sources of noise are the optical crosstalk and the afterpulses.

2.4.1.1 Dark current

The dark current arises from thermally generated electrons that trigger an avalanche in the high field region. Signals resulting from the breakdown of the cell, either from photoelectrons or thermally generated electrons, are identical. Therefore, the latter ones are a source of noise at the single photon level.

The probability of thermally producing electron-hole pairs is a function of the temperature T:

$$P(T) = CT^{3/2}exp(-E_g/2k_BT) \tag{2.20}$$

where E_g is the bandgap energy, k_B is the Boltzman constant and C is a proportionality constant.

An example of output signal of a SiPM showing 1-pixel of dark current is reported in Fig. 2.13 (a). This effect can be reduced by cooling down the device or by reducing the volume of the depleted region, i.e. the dimensions of the SiPM cells.

Dark current rate is also due to field-assisted generation of free electrons. This phenomenon is due to the large electric field inside the depleted region: free carriers have a probability proportional to the electric field to overcome the potential barrier by quantum mechanical tunnel effect. This process can be reduced decreasing the bias voltage and, consequently, the electric field inside the junction.

Both the thermal and field-assisted processes are mediated by impurities inside the *pn* junction which act as generation-recombination centers. This means that another way to reduce dark counts is to use a very pure and defect-free silicon technology [62]. The dark count rate can be substantially reduced increasing the threshold of the readout electronics to values larger than the amplitude of the single photoelectron signal. A threshold scan performed increasing the threshold is shown in Fig. 2.13 (b).

The presence in the dark count events of signals with amplitude larger than the single photoelectron is due to the optical crosstalk.

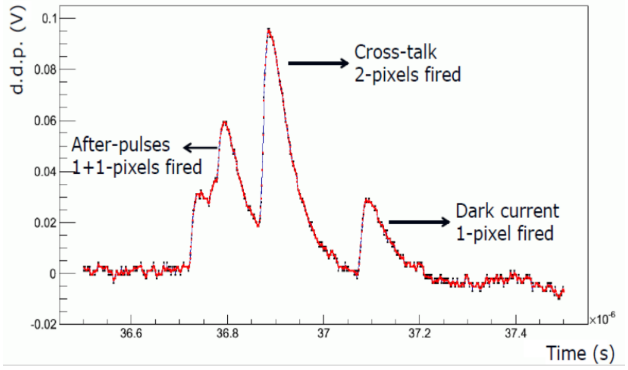

(a)

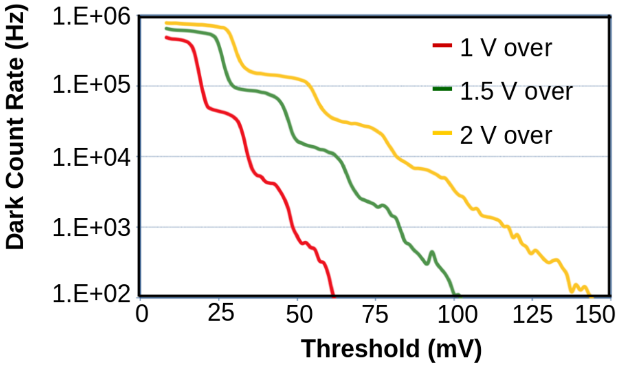

(b)

Figure 2.13: (a) Output signal of a SiPM recorded in a time window of 1 μs. It shows 3 main sources of noise: the pulse on the right is 1-pixel dark current signal, the middle pulse is a signal generated by optical crosstalk and the pulse on the left shows an afterpulses. (b) Dark count rate as a function of counting threshold, for different over-voltages.

2.4.1.2 Optical crosstalk

An additional component of SiPM noise is the optical cross-talk between microcells. This phenomenon is due to photons emitted by accelerated electrons during the avalanche breakdown in one cell that travel to the neighbouring cells and trigger a second avalanche (see Fig. 2.14). Typically 10^{-5} photons per electron are emitted. These photons are mainly in the near infrared region and can travel substantial distances through the device. The crosstalk probability is that of an avalanching microcell to initiate an avalanche in another microcell. The process happens instantaneously and as a consequence, single photons may generate signals equivalent to a 2, 3 or higher photoelectron event. This can be seen for the middle pulse shown in Fig. 2.13 (a) where the pulse height is equivalent to a 2-photon event. The optical crosstalk probability is a function of SiPM over-voltage and the distance between neighbouring microcells. It can be estimated by the ratio of the count rate at the second photoelectron level to the count rate at the

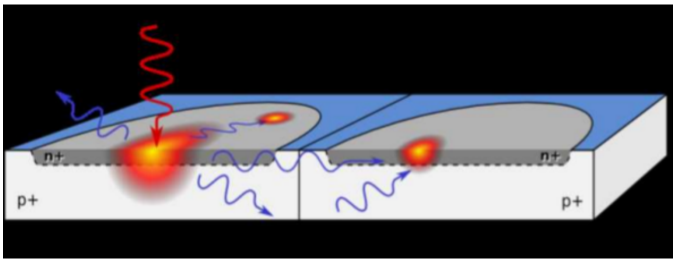

Figure 2.14: Illustration of the optical crosstalk phenomenon.

single photoelectron level.

The optical crosstalk can be reduced by placing the microcells at a larger distance, by introducing *trenches* and *grooves* between the cells which act as optical isolation and by reducing the bias in order to reduce the avalanche trigger probability. With the first solution the optical crosstalk is reduced at the expense of the geometrical fill factor, while the third solution reduces the avalanche trigger probability: in both cases the resulting effect is a much lower PDE. The second solution is the most convenient one and is used by many SiPM manufacturers.

2.4.1.3 Afterpulses

Another source of noise are after pulses. In this process the carriers trapped in metastable traps during the avalanche discharge are released with a certain delay with the effect of triggering a new avalanche even few 10 ns after the breakdown. The resulting output signal of the SiPM presents a first pulse followed by a second pulse with a delay that can last from nanoseconds up to several microseconds as shown in Fig. 2.13 (a). The charge fraction carried by these pulses depends on the recovery state of the corresponding pixel and can be calculated from the recovery time τ_r. If the time delay with respect to the preceding pulse, is short, only pulses smaller than the 1 p.e. signal amplitude are generated; if the delay is larger than the pixel recovery time, a standard avalanche signal is triggered.

2.5 WLS fibers

Often in many experiments, it is not practical to couple the photodetector directly to the scintillator. The reasons could be several, such as the lack of space or an inconvenient scintillator shape, the sensitivity of the photosensor too low at the wavelength of the light emitted by the scintillator, etc. Optical fibers represent a common solution to couple a photo sensitive sensor with a scintillator detector in order to maximize the light collection. The light signals produced by the scintillator are guided by the fiber to the surface of the photodector.

Optical fibers consist of two components: a core and one or more claddings as shown in Fig. 2.15 (a). The core is usually made of PS or PMMA. Fibers with core diameters much larger than the wavelength of the transported light are called multimode fibers. Their core diameter typically ranges between 50 μm and 2 mm. In this case, the trajectory of light inside the fiber can be described by geometrical optics. A cladding is a layer surrounding the fiber core with a thickness of typically a few percent of the fiber radius. Typical materials for claddings of plastic fibers are PMMA or fluorinated polymer (FP). Cladding's refractive index n_{clad} is lower than n_{core}: for example, for Saint-Gobain fibers [63] (used in the tests described in chapter 3) n_{clad} is 1.49 and n_{core} is 1.6. An optical fiber may have multiple claddings (multicladding fiber) each with a lower refractive index than the underlying one allowing repeated total internal reflections used to confine and propagate light inside fiber.

When light transit from one medium (with a refractive index n_{in}) into another (n_{out}), its direction changes depending on the incident angle α_{in} between the light ray and the interface normal. The deflection is given by the Snell's law:

$$n_{in} \cdot sin(\alpha_{in}) = n_{out} \cdot sin(\alpha_{out}) \Leftrightarrow \alpha_{out} = arcsin\left(\frac{n_{in}}{n_{out}} \cdot sin(\alpha_{in})\right) \tag{2.21}$$

if $n_{out} < n_{in}$ and for incident angle larger enough, α_{out} exceeds 90° and the light is reflected back into the outgoing medium leading to a total internal reflection. The critical incident angle can be calculated for $\sin(\alpha_{out}) = 1$:

$$n_{in} \cdot sin(\alpha_{in}) = n_{out} \Leftrightarrow \alpha_{out} = arcsin\left(\frac{n_{in}}{n_{out}}\right) \tag{2.22}$$

The propagation of a photon emitted after the passage of a charged particle or a photon inside the fiber core is shown in Fig. 2.15 (b). Only a fraction of the emitted light (with $\alpha_{in} > \alpha_{cr}$) can be trapped inside the fiber through total internal reflections. This fraction corresponds to the trapping efficiency of the fiber. Typical trapping efficiency of multi-cladding fiber is around $\sim 6\%$.

There are three types of optical fiber: standard light guides, scintillating fibers and WLS fibers. The latter, besides the light transportation, absorbs also the scintillation light and re-emits it isotropically at a greater wavelength. For example, in Fig. 2.16, are shown the absorption and emission spectra of WLS fiber BCF-91A produced by Saint-Gobain: the light absorbed (blue) is then emitted in another region of the spectrum (green).

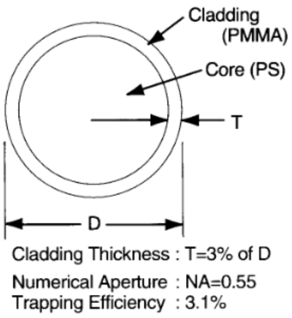

(a)

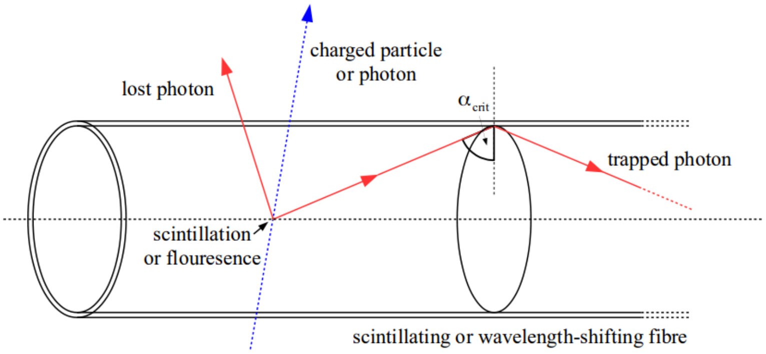

(b)

Figure 2.15: (a) A frontal section of an optical fiber. It consists of two components: the core and one or more claddings. (b) Schematic of an optical fiber (scintillating or WLS): photons are emitted after the passage of a charged particle or a photon. They are trapped inside the fiber through total internal reflection if the incident angle at the core-cladding interface is larger than the critical angle α_{crit}.

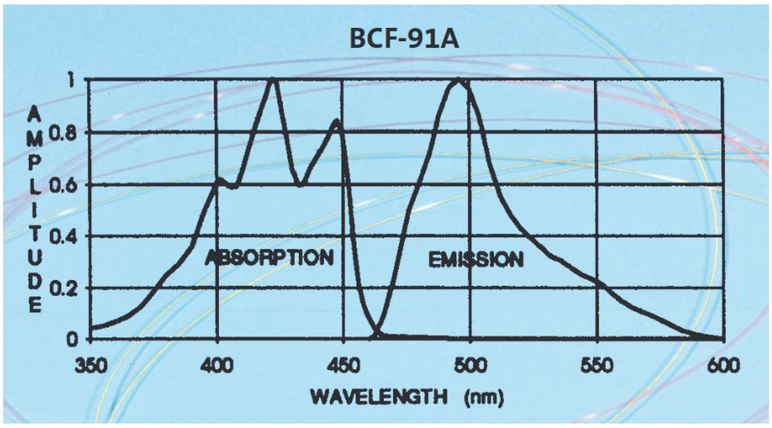

Figure 2.16: Absorption and emission spectra of WLS fiber BCF-91A produced by Saint-Gobain.

Chapter 3

Preliminary tracking system

In this chapter I report about the results obtained with a small tracking system composed of 4 planes of scintillator bars + WLS fiber coupled to SiPM. First tests were performed to characterize the response of scintillator bars and SiPMs. Then tracks of cosmic muons crossing the detector planes were reconstructed. The spatial resolution of detector planes was also measured [64].

3.1 Characterisation of Silicon Photomultipliers

The SiPMs selected for the first tracking system prototype are the MicroSL-10035 SiPM provided by SenSL manufacturer [65]. This device has an active area of ~ 1 mm^2 and in total 576 microcells with a size of 35 μm each, and an overall fill factor of 64 %. The breakdown voltage, as reported in the datasheet, is (27.5 ± 0.5) V; the overvoltage ΔV_{ov} can range between 1 and 5 V. For this SiPM two different kind of packaging are available as shown in Fig. 3.1: the ceramic package (MicroSL-10035 X13) and the TO18 package (MicroSL-10035-X18) with a metal cap and a glass window. We tested SiPMs with both packages: with the ceramic package the WLS fiber is directly coupled to the SiPM while with the TO18 package there is a gap of air between the two. We found that using the ceramic package the amount of

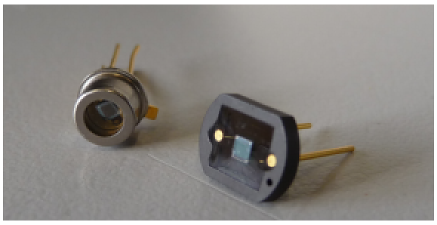

Figure 3.1: (on the left) SiPM MicroSL-10035 X18 with TO18 package; (on the right) SiPM MicroSL-10035 X13 with ceramic package.

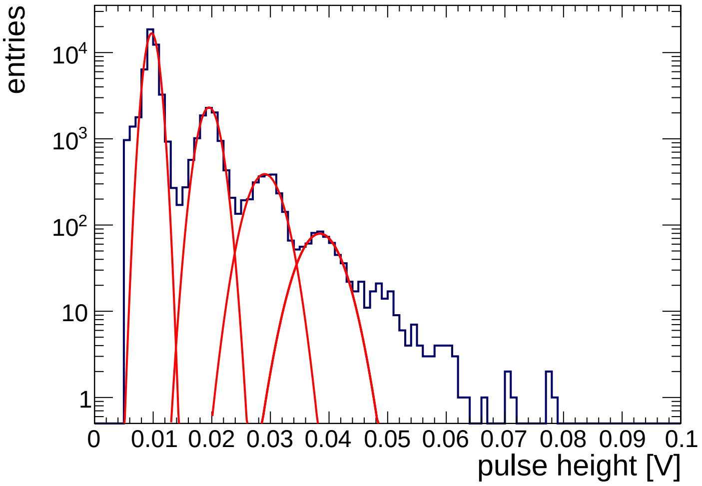

Figure 3.2: Pulse height distribution of the dark current for the MicroSL-10035 SiPM. The total collection time was 25 ms at $\Delta V_{ov} = 1.5$ V and T = 26 °C. The Gaussian curves (red) are drawn to identify the first four peaks.

light hitting the SiPM surface is larger than using the TO18 package resulting in higher signal amplitudes. For this reason the SiPM MicroSL-10035 X13 was chosen to test the tracking system.

3.1.1 Measurement of the dark current

As discussed in 2.4.1, the main source of noise for SiPMs is the dark current rate, namely the rate of spurious current pulses in absence of light. The dark current pulse height distribution, measured at a working voltage V_{bias} of 29 V and at a temperature of $\sim$ 26 °C, is shown in Fig. 3.2 for MicroSL-10035 X13 SiPM. The dark current rate (DCR), including also contributions from cross talk and after pulses is $\sim$ 900 kHz.

DCR depends on the V_{bias} as shown in Fig. 3.3 which report a measurement that I performed for a MicroSL-10035 X13 SiPM. In order to have low rates of dark current I fixed the value of ΔV_{ov} at 1.5 V (V_{bias} = 29 V).

As discussed in Section 2.4.1 the dark current counts depends on the temperature. I investigated the variation of the dark current single pixel rate as a function of the temperature using Peltier cells[1] in order to keep the temperature controlled. The results are shown in Fig. 3.4 where the reported rate takes into account only the contribution of the 1st dark current pixel. In the 18-28 °C temperature range the variation of the dark current rate

---

[1] Peltier cell is a thermoelectric device for cooling that uses the Peltier effect to create a heat flux between the junction of two different types of materials. The Peltier effect is the heat transfer that occurs when an electric current flows between two metals or semiconductors placed in contact through a junction.

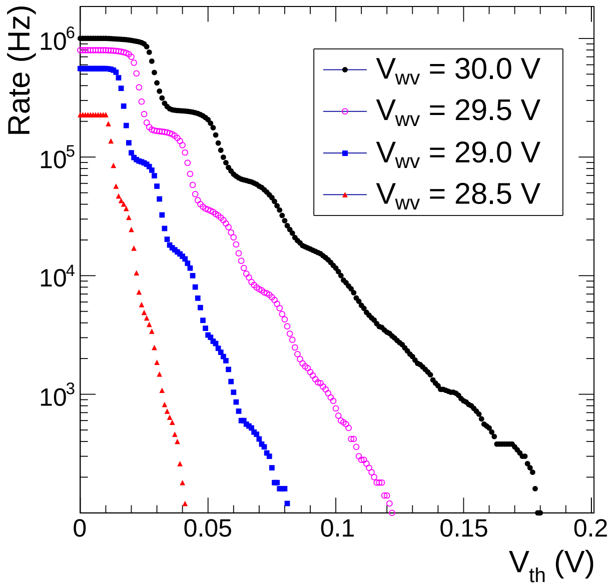

Figure 3.3: Dark current rate of the selected SiPM for different working voltages versus the threshold voltage V_{th}. Measurements have been performed at T = 26 °C.

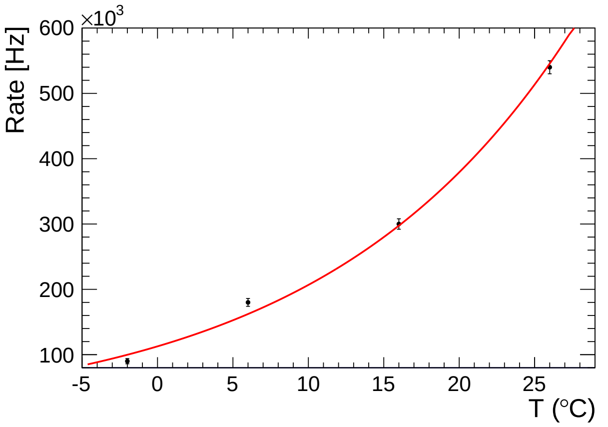

Figure 3.4: Dark current rate of the 1st pixel of the selected SiPM versus room temperature of the selected SiPM at fixed $\Delta V_{ov} = 1.5$ V. The red line, drawn to guide the eye along the measured values, follows a theoretical exponential behaviour.

is $\sim 5\%/^{\circ}$C. I also studied the dependence on the temperature of the peak amplitude. In Fig. 3.5 the SiPM pixel amplitude shows a linear dependence on temperature, where the error bars take into account the SiPM signal fluctuations of ± 1 mV due to electronic noise. By fitting linearly the data

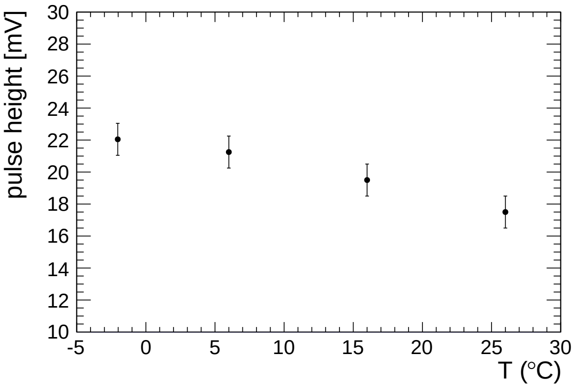

Figure 3.5: Peak amplitude dependence on room temperature for SiPM MicroSL-10035 X13 SMD SenSL at V_{bias} = 29 V and gain = 10^6.

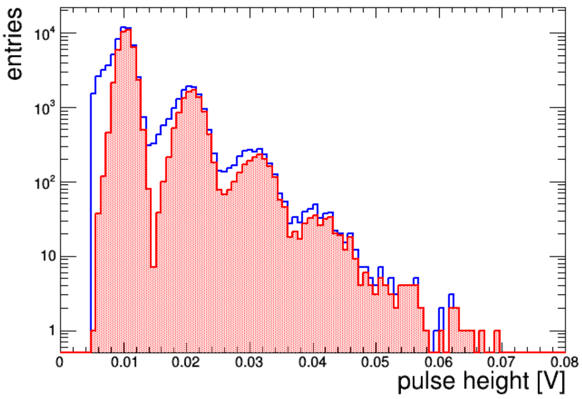

Figure 3.6: The experimental dark current distribution of Fig. 3.2 (blue histogram) is reported together with that simulated with the framework GosSiP (red histogram).

points I found that the variation of the peak amplitude is about 0.2 mV/°C.

An estimate of the optical cross talk probability can be obtained by the ratio double-to-single pulse rate as discussed in Section 2.4.1. Optical cross-talk between pixels leads to a non-Poissonian behaviour of the distribution of fired pixels. I measured the cross-talk probability which is ∼ 15-16%, compatible with the one reported in the datasheet.

The SiPM under test was also simulated with the framework GosSiP [66], which gives a detailed model of the SiPM response by providing its basic parameters and microcells configuration (i.e. the number of microcells, the microcell size, the fill factor etc). In Fig. 3.6 the experimental dark current distribution of Fig. 3.2 (blue histogram) is reported together with that obtained with the simulation (red histogram).

3.2 The detector unit

As discussed in Section 1.5.1, the aim of this thesis is to prove the feasibility of a particle tracker prototype based on scintillator strips with isosceles triangular cross-section. A detector unit is composed of a scintillator bar embedding a WLS fiber coupled to a SiPM. Each bar is 50 cm long with a base of 3.3 cm and an height of 1.7 cm and the lateral surface is painted with white titanium dioxide paint (Eljen EJ-510 TiO_2 [67]) to increase the total internal reflections of light in the scintillator.

The scintillation light is collected by 1.2 mm BCF-91A multicladding WLS fiber[2]. This fiber has a minimum trapping efficiency of 5.6 %, an attenuation length > 3.5 m and shifts blue to green with an emission peak at $\lambda = 494$ nm. The fibers are glued to the strip along the hole with RTV 615 silicone rubber (optical glue) [68] and ends are polished with sandpaper. Because of the reduced length of the bar the read-out is done only at one end; the other end is mirrored with reflecting tape to maximize the light collection. The coupling between the WLS fiber and the SiPM is obtained by a plastic mask properly shaped to host the SiPM and tightly coupled to the sensor surface.

The response of each bar coupled to a SiPM was tested by injecting light pulses provided by a laser and also by collecting the light induced by a radioactive source.

3.2.1 Tests with laser pulses

The product of the photon detection efficiency (PDE) and the gain determines the SiPM response to the light hitting its surface. For the SiPM under test the PDE, which is wavelength dependent, is about 15% at $\lambda \sim 500$ nm as reported in the datasheet. The gain can be measured by determining the distance between two adjacent peaks of a charge spectrum (see Fig. 3.7), corresponding to the charge of 1 fired pixel. At $V_{bias} = 29$ V and T ~ 26 °C the gain is $\sim 2.4\times10^6$ as reported in the datasheet. The amplitude of one pixel signal is ~ 10 mV.

The charge spectrum shown in Fig. 3.7 was obtained by injecting into the scintillator bar laser pulses from Picosecond Diode Laser (PiLas). Fig. 3.8 (a) shows a sketch of the experimental setup used for the laser measurements. A module composed of 8 bars was inserted inside an aluminium box: the end of the module near the SiPMs is plugged in a cap made with a black plastic mask (as explained in Section 3.4.1) while the other end is closed by means of a light injection mask (black plastic). Laser pulses were guided through a fiber into the injection mask which is provided with holes as shown in Fig. 3.8 (b). During the test the fiber was inserted into a hole so that the light is

---

[2] Produced by Saint-Gobain Ltd [63]

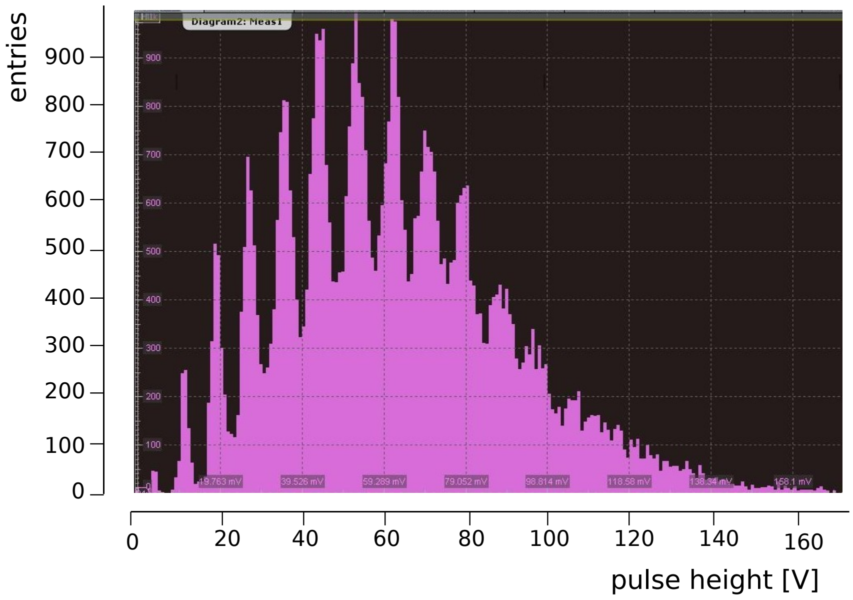

Figure 3.7: Charge spectrum of a SiPM obtained by injecting laser pulses on the scintillator bar at a distance of ∼ 6 mm from the WLS fiber. The amplitude of 1 pixel is ∼ 10 mV.

injected on the scintillator surface at a distance of ∼ 6 mm from the WLS fiber.

In Fig. 3.9 it is shown that signal pulse height and pulse area are proportional, for this reason in the following, measured SiPM outputs are indicated indifferently by mV or ADC counts.

All triangular bars used in the test with cosmic rays described in Section 3.4 were tested with laser pulses. For each bar a charge spectrum as the one shown in Fig. 3.7 was obtained. The calibration factors c_i for each detector unit were calculated as:

$$c_i = \frac{\Delta V_{mean,i}}{\Delta \overline{V}_{mean}} \tag{3.1}$$

where $\Delta V_{mean,i}$ is the mean signal amplitude value for each bar charge spectrum and $\Delta \overline{V}_{mean}$ is the mean value among all the bars. Calibration factors allow to correct for different WLS-SiPM coupling, WLS-scintillator coupling, etc., among detector units. Bar calibration factors are listed in Table 3.1.

3.2.2 Study of fiber-scintillator optical coupling

As stated before the WLS fiber is glued inside the scintillator bar. In order to choose the best medium to optically couple the fiber to the scintil-

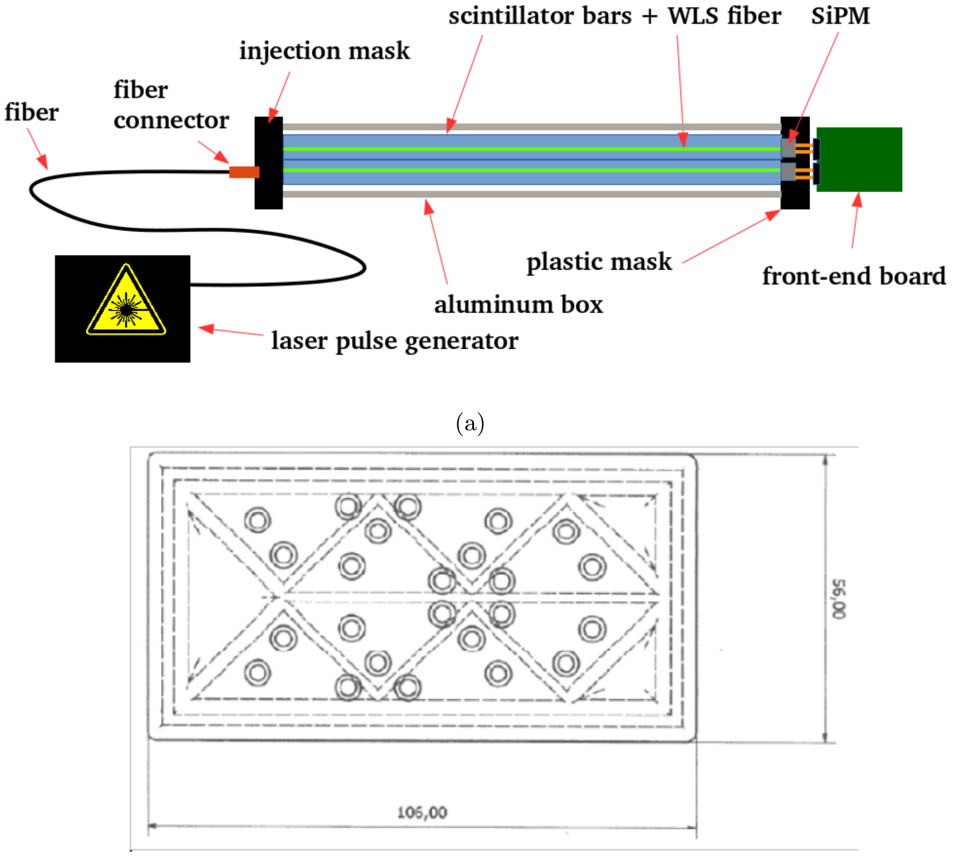

(a)

(b)

Figure 3.8: (a) A sketch of the experimental setup used in the measurements with the laser source. (b) A drawing of the frontal view of the light injection mask used in the measurements with the laser source. Circles indicate holes to inject the laser light.

lator and to maximize the light collection I did some preliminary test with different coupling mediums. For this purpose a system composed of three adjacent scintillator bars as shown in Fig. 3.10 was set up. Different gluing materials were tested: silicone rubber RTV 615 with two components (glue), glycerine and liquid paraffin (oil) with refractive index 1.406, 1.472 and 1.477 respectively.

The response of each bar was studied injecting laser pulses into the scintillator as described in Section 3.2.1. The signal amplitude distributions obtained injecting laser pulses at different attenuation factors in the bar with the glue are shown in Fig. 3.11 (a). Similar measurements were performed using the other coupling mediums. The mean value of the signal amplitude is shown in Fig. 3.11 (b) as a function of the laser attenuation factor for each bar. The measurements show that the best optical fiber-scintillator

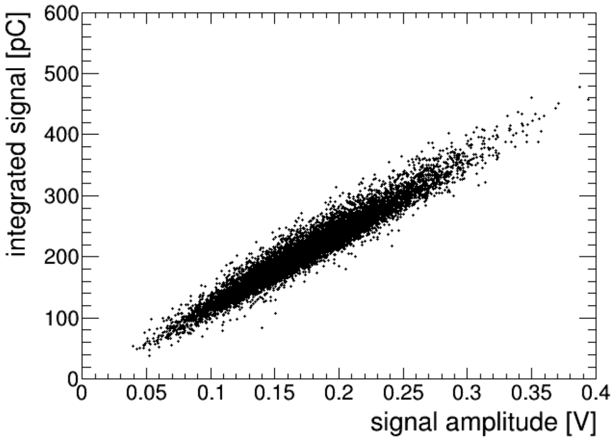

Figure 3.9: Integrated signal value vs. amplitude of the linear signal.

channel - module 1	calib. factor	channel - module 2	calib. factor
Ch00	0.70	Ch10	1.13
Ch01	1.35	Ch11	0.53
Ch02	0.86	Ch12	1.24
Ch03	1.14	Ch13	1.00
Ch04	1.20	Ch14	1.09
Ch05	0.98	Ch15	1.00
Ch06	0.93	Ch16	1.01
Ch07	0.82	Ch17	1.00

Table 3.1: Calibration factors for each detector unit obtained through measurements with the laser source.

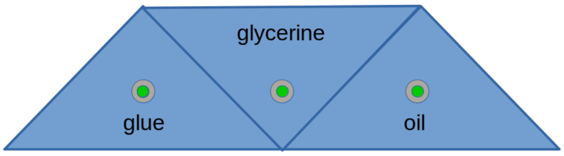

Figure 3.10: A system of 3 adjacent bars, each with the fiber optically coupled with different mediums: silicone rubber RTV 615 with two components (glue), glycerine and liquid paraffin (oil).

coupling is obtained using the optical glue: for 43 % laser attenuation the mean signal amplitude obtained with the glue is 10 times larger than that obtained with the glycerine and 5 times larger than that obtained using oil.

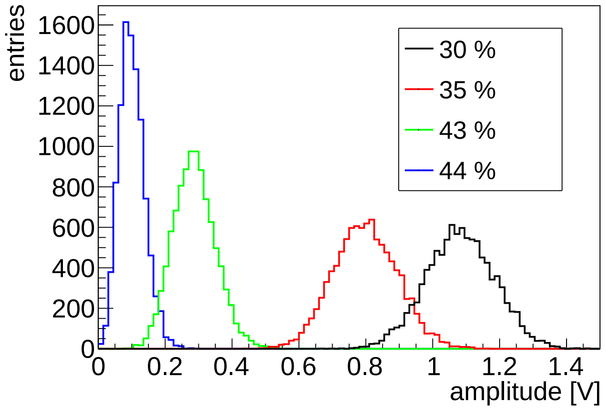

(a)

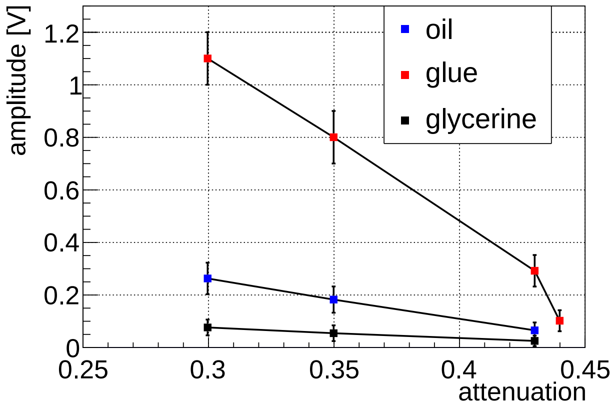

(b)

Figure 3.11: (a) Signal amplitude distributions obtained injecting laser pulses at different attenuation factors (30 %, 35 %, 43 % and 44 %) in the bar with the glue. (b) Mean value of signal amplitude distribution of each bar shown in Fig. 3.10 as a function of the laser attenuation factor. Error bars are the RMS of the signal amplitude distributions.

3.2.3 Determination of the light attenuation length

In order to evaluate the attenuation length of a detector unit, I studied the response of a system made of two adjacent triangular bars (see Fig. 3.12) coupled to SiPMs using a ^{90}Sr β-source having an activity of $\sim$ 90 kBq and a decay energy spectrum peaked at $\sim$ 0.5 MeV. The two scintillators were placed inside a metallic box with 5 equispaced holes to accommodate the source at different positions along the two bars. The vertical axis of the source collimator passed at a distance of 4 mm from the fiber of scintillator # 2 and 12.5 mm from that of scintillator # 1.

SiPMs were cooled at T $\sim$ 1 °C using Peltier cells in order to have the

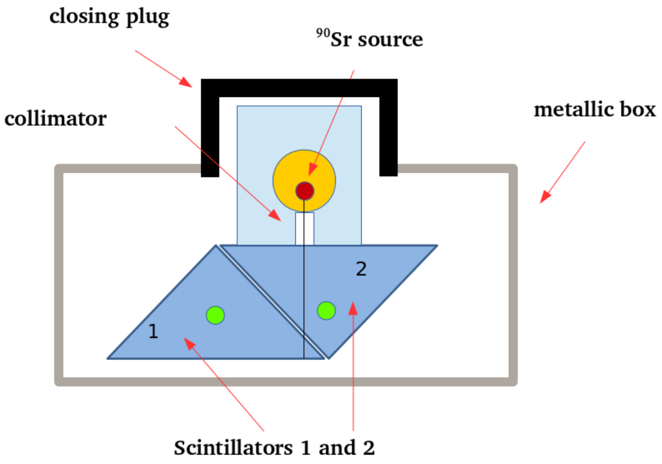

Figure 3.12: The setup used in the measurement with the radioactive source.

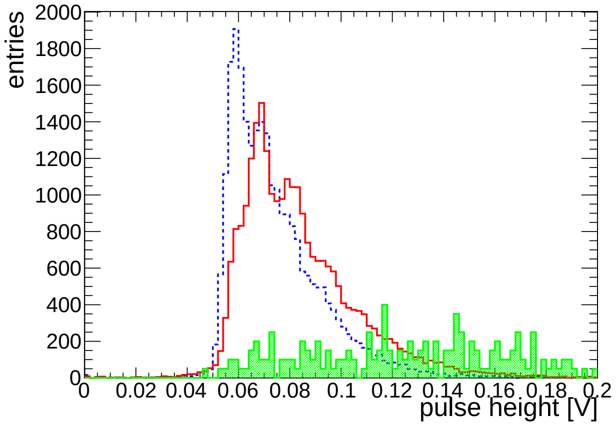

Figure 3.13: The distributions of pulse heights measured with a radioactive source placed above the bars # 1 and # 2 (see text and scheme in Fig. 3.12) at a distance of 25 cm from the SiPMs: blue dashed (red solid) histogram for scintillator # 1 (# 2). Green filled area corresponds to the coincidence signals in scintillator # 1 and # 2 without the source. In this latter case entries are multiplied by a factor 50.

best signal-to-noise ratio (as shown in Fig. 3.4). With this setup a signal is acquired triggering on the coincidence in both scintillators. In a first measurement shown in Fig. 3.13, the discriminator threshold on the signal amplitude was set to 60 mV for both scintillators. Fig. 3.13 shows the distribution of pulse height signals in scintillator 1 and 2 obtained with the radioactive source at 25 cm from the scintillator end. The green histogram shows the contribution of cosmic rays signals (obtained in a measurement without the source). Then the discriminator threshold on the signal amplitude was set to 120 mV in the scintillator # 2 and to 60 mV in the scintillator

1 because the β-electrons emitted travel a greater distance in scintillator # 2 than in scintillator # 1, producing on average larger signal amplitudes. In Fig. 3.14 (a) are shown the signal amplitude distributions in scintillator # 2 with the source at different positions along the bar: 5, 25 and 45 cm from the SiPM. As expected, by increasing the distance of the source from the SiPM, the rate of high amplitude signals (signals > 80 mV) in Fig. 3.14 (a) decreases, which is a signature of light attenuation because less photons reach the SiPM surface. For example, with the source at 5 cm from the SiPM the rate of high pulses is 50% larger than at 25 cm and 45 cm from the SiPM. The "attenuation" length of scintillator strips + WLS fibers was evaluated by measuring the rate of coincident pulses over a fixed threshold ($V_{th} = 80$ mV) when the radioactive source is at different positions along the two bars. The result is shown in Fig. 3.14 (b). As it appears from the figure, the rate variation shows two components, a "short" one and a "long" one. By taking into account a systematic uncertainty of 1 % on the longitudinal positioning of the source and of 2 % on the rate from CRs contribution, the fit of the data to the sum of two exponential functions gives a "short" $L_1 = (4.4 \pm 0.5)$ cm and "long" $L_2 = (290 \pm 70)$ cm attenuation lengths. The long component is dominated by the fiber attenuation length $L \sim 3.5$ m [63].

3.3 Front-end electronics

The front-end electronics is directly connected to the SiPM. It includes the transimpedance amplifier for the current-to-voltage conversion of the SiPM signal ($V_{out} = -R \times I_{SiPM}$.) and the input connectors for the power supply and the V_{bias}. The amplifier output is split in two chains: an integration and shaping chain with a time constant of about 150 ns and an amplification chain with a gain of 10. Therefore, as sketched in Fig. 3.15 (a), the front-end board has three output:

1. a linear (negative) output with a gain factor G = 10
2. a linear inverted (positive) output with G = 10
3. an integrated output

The front-end board provides a fast signal with 20-30 ns of rise time.

Each front-end board (shown in Fig. 3.15 (b)) handles 8 channels. The board is provided with LEMO connectors to acquire the negative, the positive and the integrated outputs. The board is also equipped with a fan to keep the temperature of the electronics stable. Each channel has its own voltage regulator (+5V, -5V). For the study of a single detector unit single channel front-end boards were used. The single channel and 8-channels front-end boards prototype dedicated to the amplification and SiPM readout has been developed by the Bologna INFN electronic group.

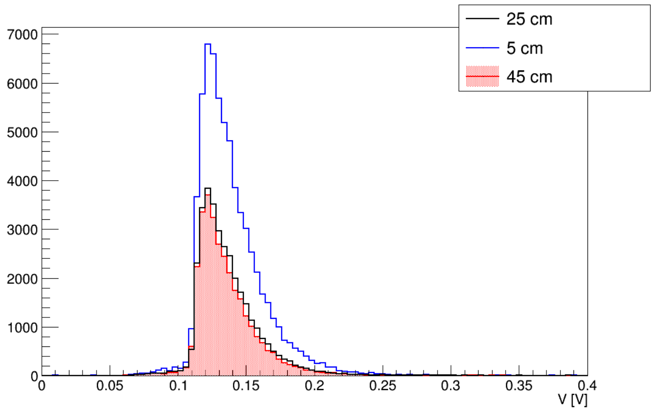

(a)

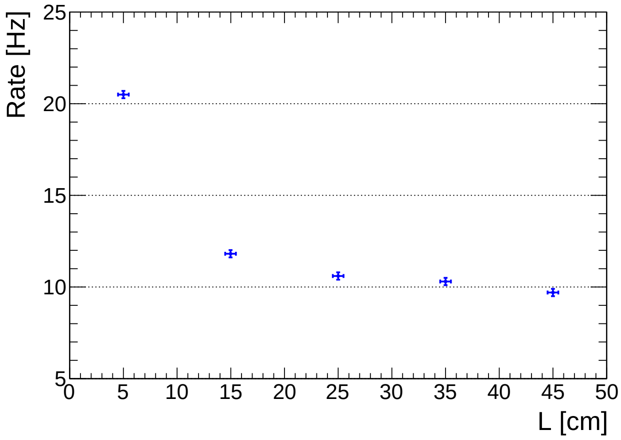

(b)

Figure 3.14: (a) Signal amplitudes with the source at: 5, 25 and 45 cm from the SiPM of scintillator # 2. (b) Rate of pulses > 80 mV coincidence in scintillator # 1 and # 2 with the source at different distances L from the SiPM. Horizontal error bars are the estimated 1 % uncertainty on the source longitudinal position; vertical errors bars indicate a systematic uncertainty of 2 % on the rate from CR.

3.4 Tests with cosmic rays

A preliminary simple laboratory system was built to be tested with cosmic muons.

3.4.1 The lab apparatus

The lab set up (Fig. 3.16) consisted of two detector modules, separated by $\sim$ 12 cm, each composed of two faced planes of 4 triangular bars. The detector modules were located between two external trigger stations separated by $\sim$ 40 cm. Each trigger station was composed by 8 staggered rectangular

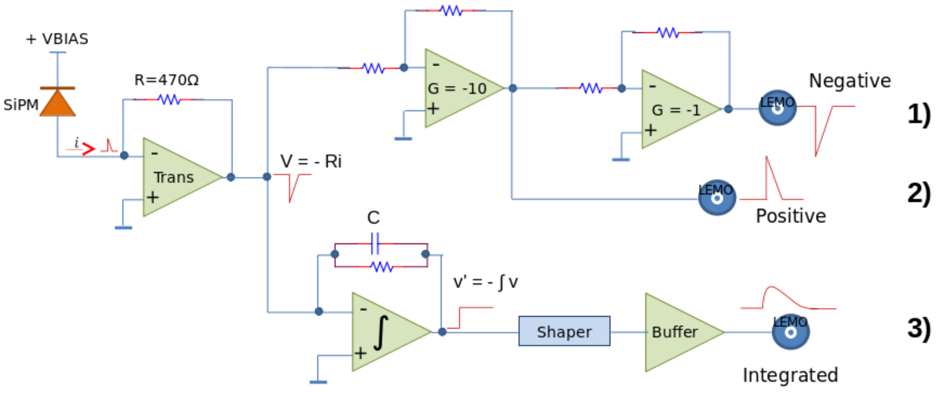

(a)

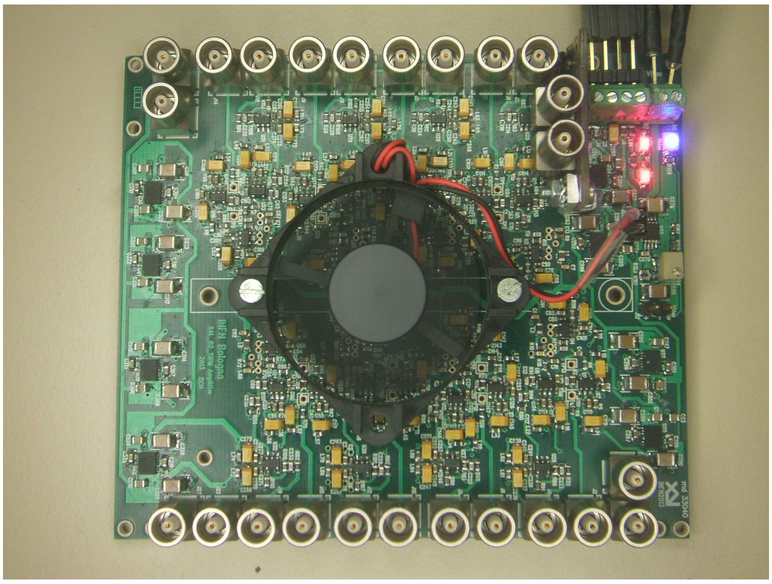

(b)

Figure 3.15: (a) Diagram of a single channel amplifier: three outputs are provided, the linear one (positive and negative) and the integrated one. The former ones are proportional to the input voltage, the latter to the current. (b) Top view of the front-end board, managing 8 channels. A common V_{bias} is applied to all channels, while each channel has its own voltage regulator.

scintillator strips (60 × 4 × 1 cm^3 each) equipped with WLS fibers, read out by SiPMs (ASD-SiPM1S-M-100) [69]. Each detector module was inserted inside an aluminium box. SiPM for triangular bars were soldered on the front-end board (Fig. 3.15 (b)) and lodged in a plastic holder (see Fig. 3.17 (a)). The SiPMs were plugged in a black cap at one end of the aluminium box for an optimal sensor WLS coupling (Fig. 3.17 (b)). The 8-channels front-end board was soldered to the external cap edge. At the other side of

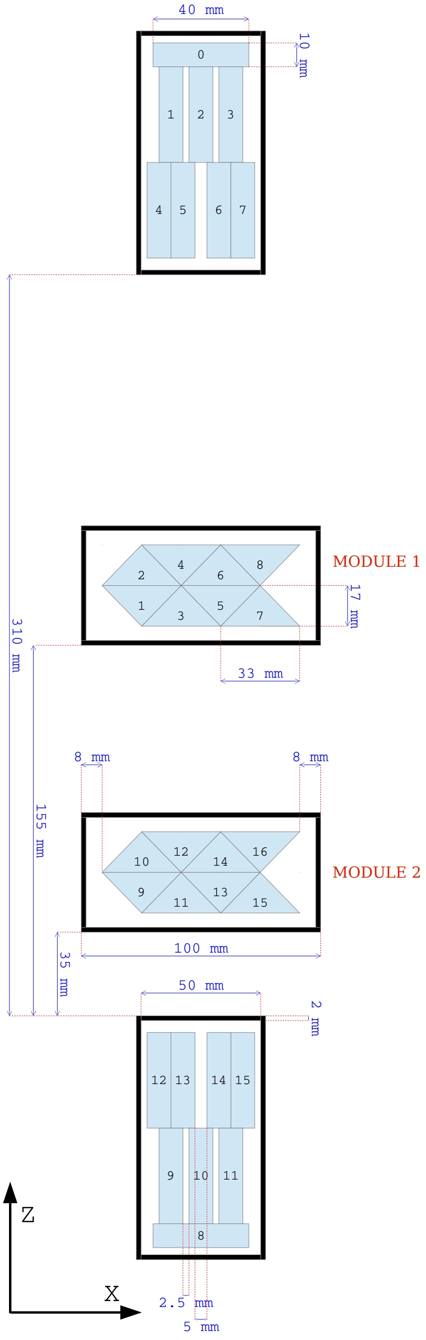

Figure 3.16: The Lab set-up used to detect cosmic muons. The detector modules can be moved independently along the x direction by a fraction of a mm. The staggered configuration of the rectangular bars allows to select CR particles in windows 0.5 and 0.25 cm wide. The origin of the x axis is set at the external border of the module box.

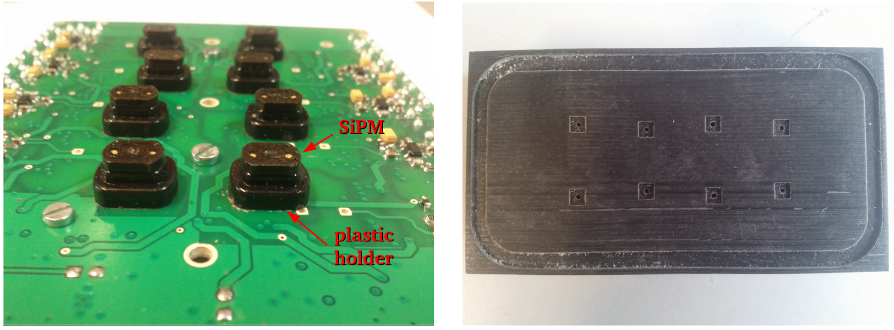

(a) (b)

Figure 3.17: (a) A picture of SiPMs soldered on the front-end board. SiPMs are kept fixed with black holders glued on the front-end board. (b) A frontal view of the black cap which has 8 site with holes to couple the SiPM to the WLS fibers.

window width (mm)	trigger quadruple
2.5	2-5-10-13
2.5	2-6-10-14
5.0	1-5-9-13
5.0	1-4-9-12
5.0	3-6-11-14
5.0	3-7-11-15

Table 3.2: Trigger coincidences of 4 rectangular bars used to select vertical muons crossing the lab apparatus in windows 5 mm or 2.5 mm wide.

the aluminium box is closed by a cap provided with an aluminium reflective foil. A picture of the aluminium box containing a module of triangular bars is shown in Fig. 3.18 (a). In each module the triangular bars were tied together and the aluminium box was placed in a mechanical support structure (see Fig. 3.18 (b)).

The apparatus was tested selecting cosmic ray muons crossing the tracking detector almost vertically along defined positions using the external trigger stations. The arrangement of the rectangular bars was such that 6 different trigger configurations were possible. Each trigger configuration ("quadruple") is a coincidence of 4 rectangular bars over threshold (~ 60 mV) which allows the selection of muons in windows 5 mm or 2.5 mm wide. The quadruple trigger configurations used in the test are listed in Tab. 3.2.

The aluminium boxes (each containing two faced planes of triangular bars) could be displaced horizontally with respect to the rectangular bars (kept at fixed positions) with an accuracy of a fraction of mm. The overall uncertainty in the nominal relative positions of the triangular bar planes was < 1 mm.

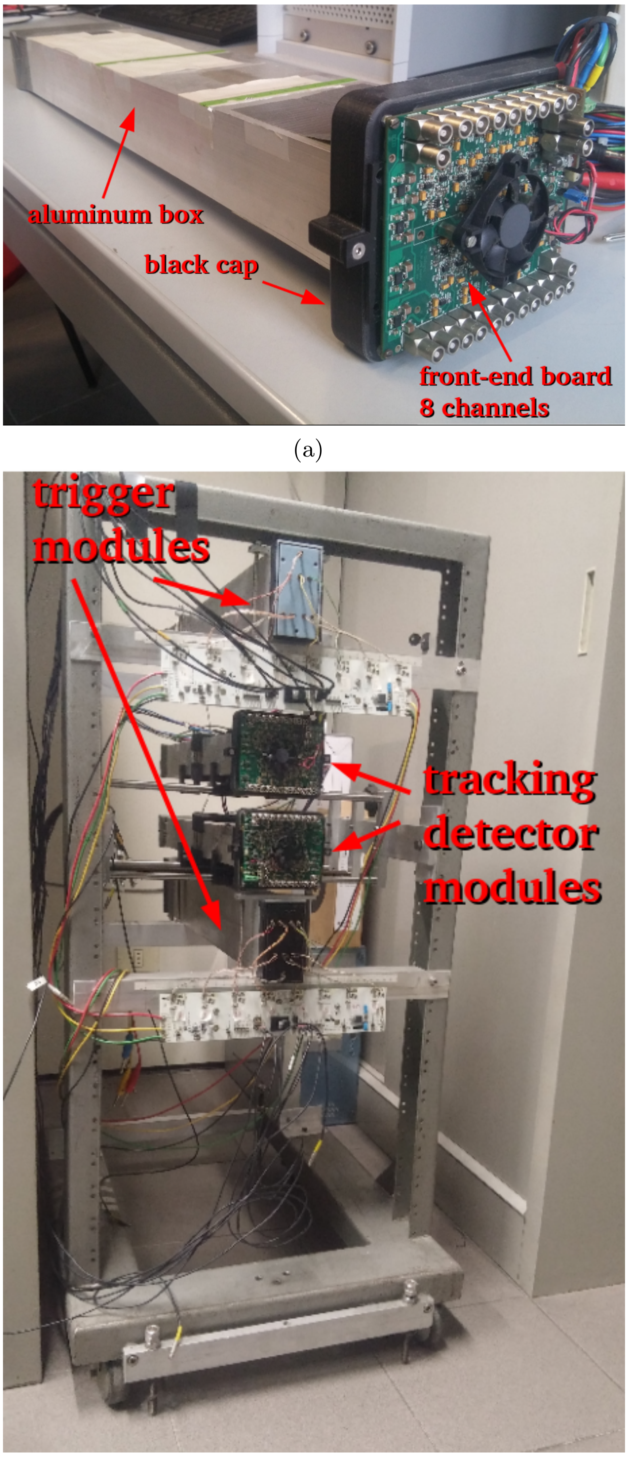

(a)

(b)

Figure 3.18: (a) A picture of the aluminium box that contains a module of triangular scintillator bars. (b) A picture of the support structure that holds the two modules of triangular bars and the two trigger stations.

3.4.2 The DAQ

The DAQ system was based on NIM and VME standards. Signals from the rectangular bars are input to discriminators (Fig. 3.19) and set in coincidence to select cosmic ray muons, as described in Section 3.4.4. Coincidence signals trigger the acquisition of triangular scintillators signals by means of waveform digitizers.

Each digitizer acquires analog waveforms from the SiPM, processes them by analog-to-digital converters (ADC) and sends the digitized sample to a buffer. The digitizer characteristics are:

- the bandwidth, namely the frequency range at which a sinusoidal input signal is attenuated to 70.7 % of its original amplitude, also known as the -3 dB point;
- the sampling rate, i.e. the frequency at which analog signals are converted to digital data by the analog-to-digital converter (it is usually expressed in MS/s or GS/s);
- the dynamic range which determines the maximum and minimum signal voltage that can be measured in one acquisition. It is related to the digitizers resolution;
- the resolution specified by the number of bits used to represent the analog value, i.e. the Effective Number of Bits (ENOB). For a resolution equal to N bits the ADC provides 2^N discrete levels;
- the acquisition memory is the buffer memory where digital data from the ADC's are stored. The depth of the digitizers acquisition memory determines the length in bit of a signal that can be stored in the buffer before it must be transferred for processing, display, or saved;
- the form factor, namely the type of standard: VME, NIM or Desktop;
- the number of input channels. Each modular digitizer has a specific number of channels per card, for example a VME digitizer has 8 to 32 input channels, while NIM and Desktop digitizer have 2 to 8 input channels;

For the tests with cosmic rays the CAEN 8 channel 12 bit 250 MS/s mod V 1720 Digitizer [70] was used allowing a time window of 4 μs with 4 ns sampling time in order to record 1024 samples for each waveform. To acquire waveforms from 16 triangular bars 2 digitizer were used, one for each detector module. This digitizer features an internal self-trigger capability; acquisitions were done also excluding the trigger provided by the rectangular bar system (autotrigger mode).

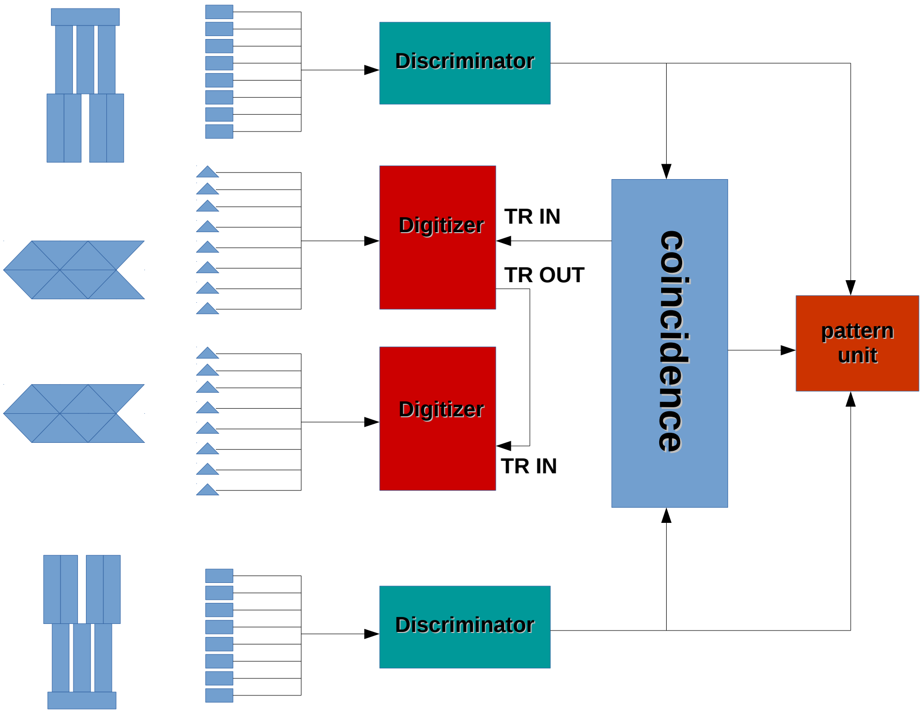

Figure 3.19: A sketch of the acquisition system: a coincidence of signals from rectangular bars triggers the acquisition of triangular scintillators signals which are input to a waveform digitizer. The trigger coincidence is sent to one digitizer which generates a trigger output that allows to extend the trigger signal to the other digitizer board.

The triangular and rectangular strip channels were recorded by pattern units and the signals from triangular bars were also sent to scalers. A sketch of the acquisition system is shown in Fig. 3.19. A single board computer with PC-to-VME interface (VMIC VMIVME-7698) allowed to control the DAQ and to store the data. The DAQ program was written in C++ language developed and used in Linux environment. The DAQ program uses the polling technique to acquire data. In this mode the computer program is in a continuous loop waiting for a clock signal given by the trigger; when the trigger arrives, the digitizer samples and stores the data. A digitizer event is composed of:

- the *Header* which has 4 32-bit words, namely the size of the event, the board ID, the event counter and Trigger Time Tag or timeStamp;
- the *Data* which have variable size depending on the number of enabled channels and on the number of samples for each channels.

Digitizer events are readout sequentially and in “SINGLE D32” mode, i.e. a 32 bit long word per time is readout. This kind of DAQ can support the readout for a system triggering on CR events since the expected rate is quite

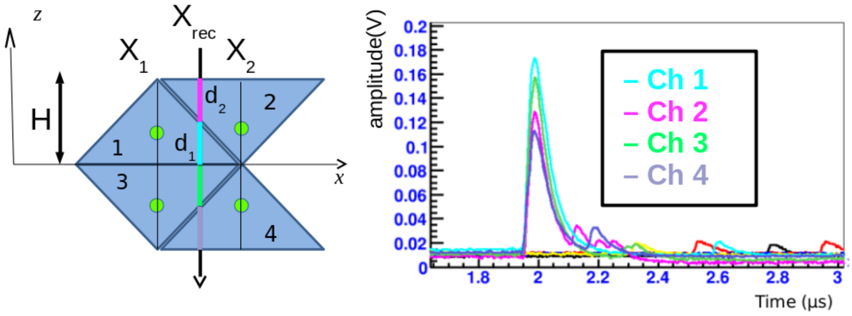

Figure 3.20: (left) A sketch of 4 scintillator bars crossed by a cosmic ray muon and (right) the corresponding signals of each channel. X_1 and X_2 are the nominal positions of the WLS fibers of scintillator 1 (3) and 2 (4) respectively. The particle position in a plane is reconstructed using the signal amplitude in adjacent channel.

low (few Hz in autotrigger mode). The DAQ program generates two files for each digitizer: a binary file containing the complete event of the digitizer and an ASCII file which contains the header of the digitizer and the pattern unit mask. It creates also a txt file with the rates of triangular bars counted by the scaler.

3.4.3 Position reconstruction

The particle crossing point on a plane of triangular bars is obtained by the pulse height in each channel. With reference to Fig. 3.20 (left), one has:

$$X_{rec} = (E_1X_1 + E_2X_2)/(E_1 + E_2) \tag{3.2}$$

where X_{rec} is the reconstructed particle position, E_i (i =1,2) is the energy lost by the particle crossing two adjacent scintillator bars; X_i is the nominal coordinate of the WLS fiber in each triangular bar from a reference position. With the assumption that the pulse height w_i is proportional to the path length of the particle across the bar ($w_i \propto d_i \propto E_i$) and $d_1 + d_1 =$ H (see Fig. 3.20), the position of the crossing point along the plane is:

$$X_{rec} = (w_1X_1 + w_2X_2)/(w_1 + w_2) \tag{3.3}$$

A sketch of 4 bars crossed by a cosmic ray muon and the corresponding signals of each channel acquired by the digitizer is shown in Fig. 3.20.

Relation 3.3 is still valid for particles entering the detector with a momentum component in the y direction, as the relative path length in the bars is the same. The coefficient of proportionality between the pulse height and the energy deposited in a bar ($w_i = c_iE_i$) can vary for each bar as shown in table 3.1 (f.e. because of slightly different WLS-SiPM coupling, scintillator response, etc), thus affecting the position reconstruction.

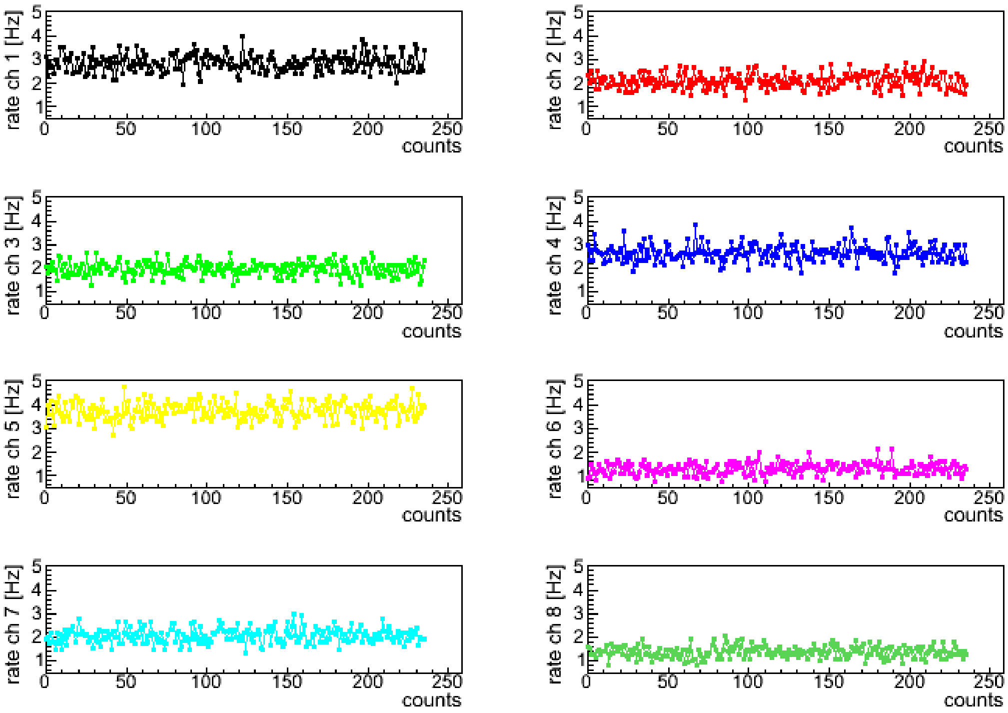

Figure 3.21: Counting rates of triangular bars of module 1 monitored with a scaler during an acquisition run. Rates are measured every 20 seconds.

3.4.4 Data taking - External trigger mode

In this section are reported the results obtained acquiring triangular bars outputs by triggering with the two external trigger station described in Section 3.4.1.

The counting rates of a triangular bar were monitored over long times by a scaler. Triangular bars outputs were sent to discriminators in which a threshold of about 3 SiPM pixels was set. The rates of module 1 measured by a scaler every 20 seconds are shown in Fig. 3.21. Stable behaviours were obtained apart from night/day variations due to slight changes in room temperatures. A similar behaviour was observed also for bars of module 2.

The trigger on rectangular bars required a coincidence of 4 vertical staggered scintillators (see Fig. 3.16). A rate of $\sim$ 20 events/hour was collected summing over all the 5 mm wide trigger configurations (4 trigger configurations); and a rate of $\sim$ 1 event/hour was collected summing over all the 2.5 mm wide trigger configurations (2 trigger configurations).

Signals from the triangular bars are in time coincidence with the external trigger if they reach their maximum amplitude within 10 digitizer sample counts (typically 40 ns by looking at the oscilloscope signals) after the trigger time. The signal distribution is shown in Fig. 3.22 together with that of the

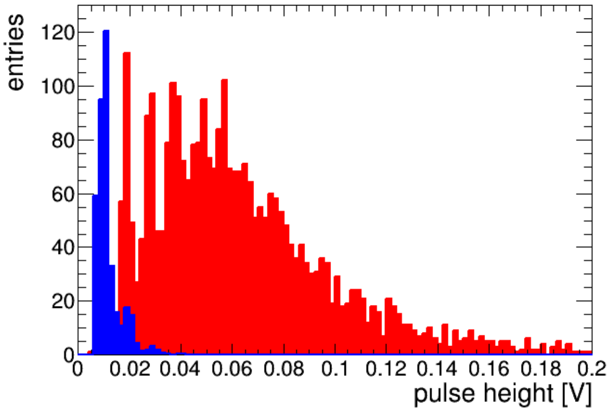

Figure 3.22: Cosmic muon signals (red solid histogram) to noise (blue solid histogram) comparison. Noise signals were collected over a time interval of the same duration as for CR muon events, far from the trigger time window.

dark current. The two distributions appear well separated.

As already reported (Section 3.1), at the SiPM working conditions (V_{bias} = 29 V and T = °26 C) the signal amplitude of one fired pixel is ∼ 10 mV. By using Peltier cells operated at 7 °C the noise is reduced by a factor 5 (from 900 kHz to about 200 kHz). Signals from triangular bars have a rise time of about 20-30 ns. In this time window and at a temperature of ∼ 26 °C the dark current contributes to a few % of the collected signals. Under this conditions and for the aims of the tests it was adequate to run the system at a normal room temperature, avoiding the use of Peltier cells.

3.4.4.1 Position reconstruction

Tracks of CR muons crossing different pairs of adjacent triangular scintillator bars could be selected by accurately modifying the relative positions of staggered rectangular modules.

As an example, in a run of 560 hours 3568 events were collected satisfying the trigger configuration 3-6-11-14 of the rectangular bars (see Fig. 3.23) with the additional (off-line) requirement of no other rectangular bar with a signal > 60 mV. This configuration triggers events crossing triangular bars # 1, # 2, # 3, # 4 of module 1 and # 9, # 10, # 11, # 12 of module 2 like the event shown in Fig. 3.24. In the remaining triangular bars (channels # 5, # 6, # 7, # 8 of module 1 and # 13, # 14, # 15, # 16 of module 2) there are no signals on time with the external trigger. In this way a sample of CR events in a 5 mm wide window were selected. A subsample of events with two adjacent triangular bars yielding a signal in time coincidence with the external trigger was selected from the sample. The position of the

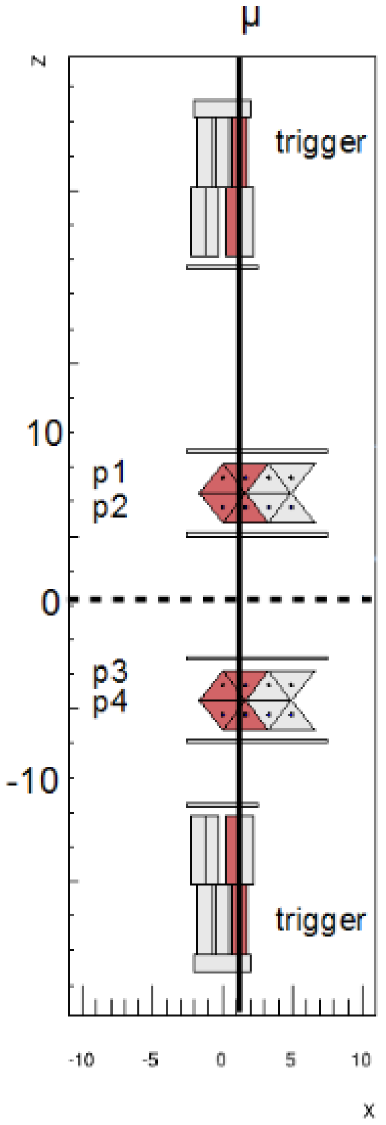

Figure 3.23: An example of a quadruple trigger configuration (3-6-11-14) of rectangular bars used to select CR muons passing through a window 5 mm wide. This quadruple is defined as the coincidence of signal over a threshold (∼ 60 mV) in rectangular bars # 3, # 6, # 11 and # 14 (with reference to the Fig. 3.16) coloured in red in this figure.

reconstructed muon tracks on each plane of triangular bars was computed. The distribution of reconstructed positions in the bottom plane of module 1 is shown in Fig. 3.25 (a) (blue solid histogram); X_{rec} is referred to the external border of the aluminium box of modules 1 and 2.

The experimental distribution is compared in Fig. 3.25 (a) with that obtained from a Geant 4.9.5 based MC simulation [71] of 1 GeV muons cross-

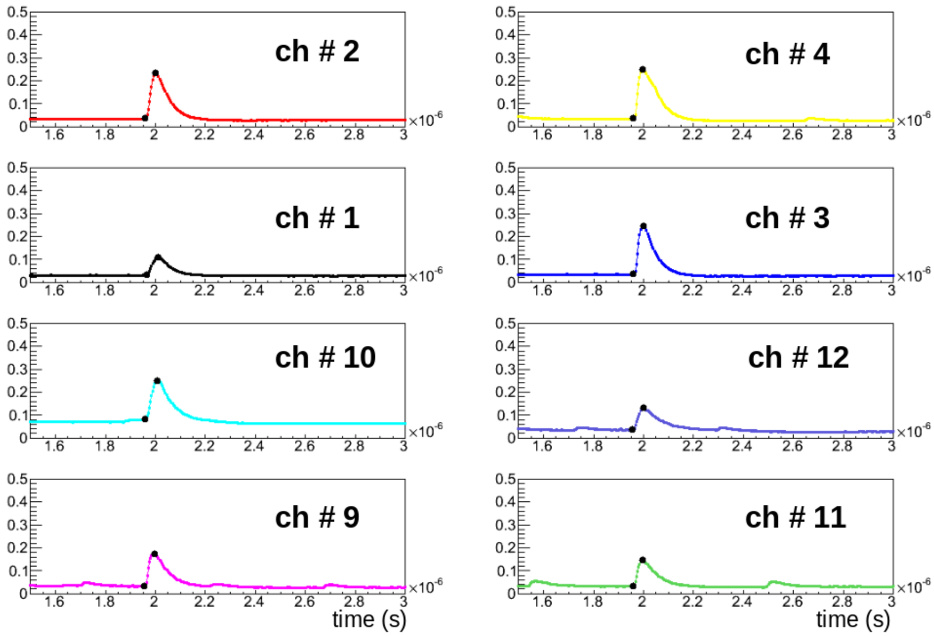

Figure 3.24: An event display that shows analog signals in triangular bars on time with the external trigger. In the example shown here the event was triggered by a coincidence of rectangular bars 3-6-11-14 and the particle crossed triangular bars # 1, # 2, # 3, # 4 of module 1 and # 9, # 10, # 11, # 12 of module 2.

ing the apparatus (red dashed histogram). Muons are uniformly distributed in the azimuth directions and follow a $\cos^2\theta$ zenithal distribution. This MC simulation takes into account only geometrical effects and energy losses. This simplified model was used to obtain a rough estimate of the spatial resolution. The HWHM of the data distribution is 2.8 mm to be compared to the value of 2 mm predicted by MC simulation. The asymmetric data distribution indicates a residual misalignment of the detector modules with respect to the external trigger bars which was not considered in the MC simulation.

Additional data sample were collected with different alignments of the triangular bar modules with respect to the external trigger frame. In a first run the left walls of the triangular bar module boxes were aligned to the left sides of the rectangular bar boxes. Events triggered by the quadruple 2-6-10-14 (2.5 mm wide window) were selected and signals from channels 1, 2, 3, 4 were collected. The reconstructed positions distribution is shown in Fig. 3.25 (b) (black solid histogram). In another run module 1 was shifted by 3 mm to the left and signals from channels 5, 6, 7 and 8 were collected obtaining the distributions of reconstructed positions shown in Fig. 3.25 (b) (blue dashed histogram). The HWHM of the former is 3 mm and that of the latter is 2.2 mm while the distance between the barycenters of the two distributions is 2.7 mm.

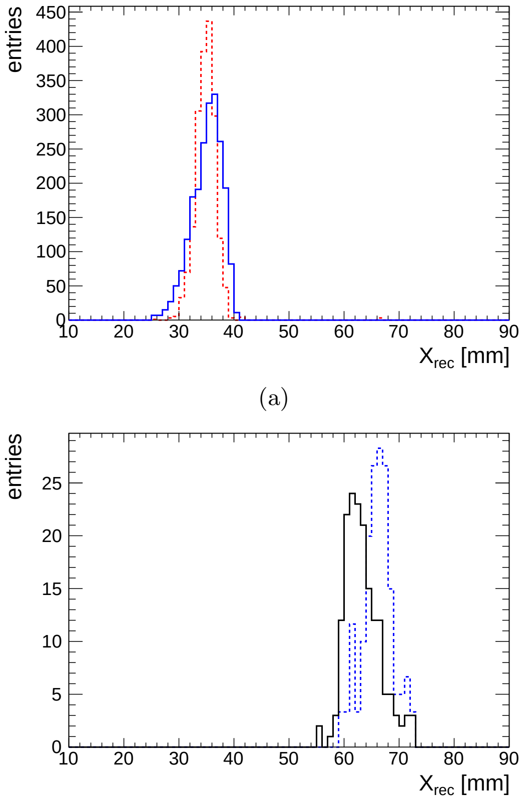

(a)

(b)

Figure 3.25: (a) Reconstructed positions in the bottom plane of module 1 for events selected by the quadruple trigger 3-6-11-14 and with only two crossed adjacent triangular bars: data (blue solid) and MC (red dashed) histograms. (b) (black solid histogram) distribution of reconstructed position in the bottom plane of module 1 for events selected by the quadruple trigger 2-6-10-14 and with only two adjacent scintillators fired in each plane; (blue dashed histogram) the distribution obtained by shifting the module 1 by 3 mm to the left with respect to the fixed external trigger system.

3.4.5 Data Taking - Autotrigger mode

The spatial resolution achievable with the modules of triangular scintillators (in the layout of Fig. 3.16), was determined in autotrigger mode by triggering on triangular bar signals requiring:

- a threshold of $\sim$ 50 mV ($\sim$ 5 pixels fired) on each channel
- at least one triangular bar with a signal over threshold in each plane

The threshold was fine tuned in order to have uniform signal rates among channels and to ensure that for each couple of adjacent bars crossed by a particle, at least one bar yielded a signal over threshold.

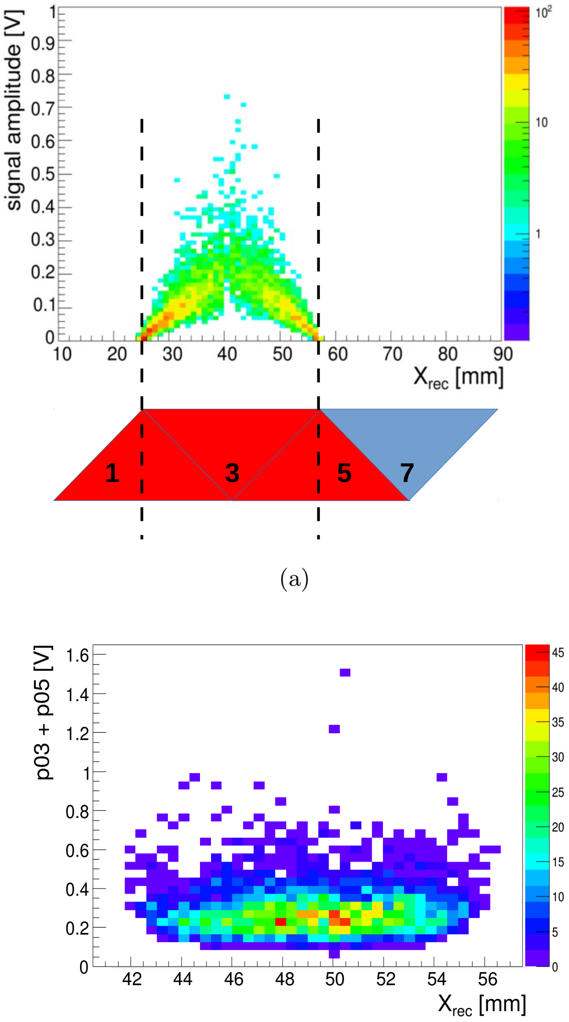

(a)

(b)

Figure 3.26: (a) Signal amplitude vs. reconstructed position in the bottom plane of module 1 for events crossing pairs of adjacent bars (1-3 and 3-5 in Fig. 3.16). No cut on signal amplitude was applied. (b) Sum of the pulse heights from pairs of adjacent triangular bars (3-5, 5-7) vs. the position reconstructed in the bottom plane of module 1. CR muon events with only two adjacent triangular bars crossed in each plane and with a slope < 50 mrad were selected.

In the data analysis channel signals in time coincidence with the trigger were considered. In Fig. 3.26 (a) the signal amplitude from channel 3 is shown versus the reconstructed position in the bottom plane of module 1 for events crossing pairs 1-3 and 3-5. An off-line cut on the minimum signal amplitude increases the size of the “dead zone” at the vertices of the triangular bars, namely the region where the particle position point cannot be reconstructed. For example, if a cut of about 30 mV (corresponding to at least 3 pixels fired) is applied, the size of the dead zone is about 1.5 mm around the fiber nominal position. In our analysis we selected pulses > 15 mV in each bar. The reconstructed position is thus not affected by the contribution of one dark current pixel occurring randomly in bars not participating in the trigger.

The energy deposited by a vertical 1 GeV muon crossing an extruded scintillator bar is about 1.7 MeV/cm. As reported in [72] the light yield of the scintillator is within 66% of the BC408 scintillator, thus ~ 8500 photons/MeV are produced. A conservative estimate of the fiber BCF-91A light collection is 0.4% [73], therefore about 60 photons/cm reach the SiPM surface. With a 15% PDE, a m.i.p. in 1 cm long path would yield about 9 p.e., namely 9 fired pixels. Fig 3.26 (b) shows the distribution of the sum of the pulse heights in two adjacent bars vs. the reconstructed position in a plane (the considered sum is proportional to the energy released by a m.i.p particle crossing vertically 1.7 cm of scintillator). The signal average value is 200 mV corresponding to 20 detected p.e., in agreement with what expected.

3.4.5.1 Bar response equalization

A sample of about 261000 events was collected in autotrigger mode, at a rate of ~ 1.7 Hz. The following analysis refers to a subsample of 22300 events selected by requiring only two adjacent bars with > 15 mV signal in each plane.

The triangular bar planes, as sketched in Fig. 3.16, were not staggered. This layout allows a cross-check of the laser calibration factors (see Section 3.2.1) using muon data. The response of each bar was calibrated introducing two estimators $Q_A = W_1/(W_1 + W_3)$ and $Q_B = W_1/(W_1 + W_2)$ for the bar couples (1,3) and (1,2) (see Fig. 3.16), where $W_{1,2,3} = c_{1,2,3} \times w_{1,2,3}$ are the signal amplitudes of bars scaled by their equalization factors c_i.

The comparison between the experimental and the MC predicted distributions of the estimators Q_A and Q_A is shown in Fig. 3.27 (a) and 3.27 (b), respectively. In the MC only the energy lost by the particle in the scintillator was taken into account. A qualitative agreement between simulated and real data can be observed. In Fig. 3.27 (a) the discrepancy between data and MC indicates a still incomplete equalization of bars 1 and 3; in Fig. 3.27 (b) the different shape of data and MC distributions could be due to optical photons, fiber-SiPM coupling and SiPM PDE not simulated in the MC. Equalization factors were thus obtained for every pair of adjacent or faced bars; they differ by a few % from those determined using laser pulses (only in one case the difference is $\sim 15\%$).

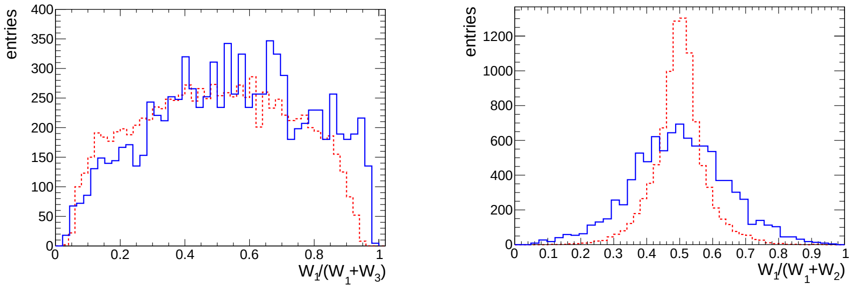

(a) (b)

Figure 3.27: (a) Distribution of the estimator $Q_A = W_1/(W_1 + W_3)$ and (b) $Q_B = W_1/(W_1 + W_2)$ from data (blue solid line) and MC (red dashed line).

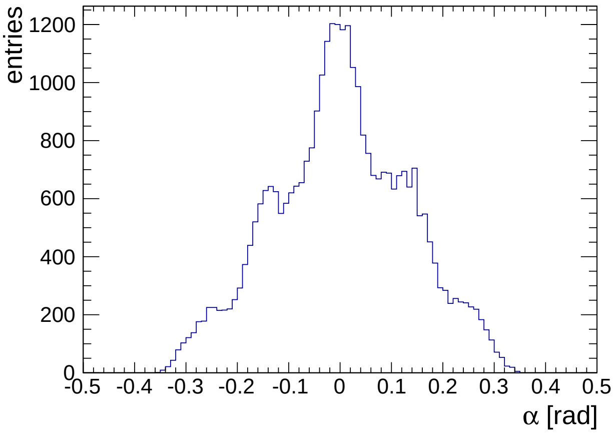

Figure 3.28: Distribution of the angle formed with the vertical axis (z) by the projection of the muon track on the xz plane for events with 2 adjacent triangular bars fired in all planes and $\chi^2 < 10$.

3.4.5.2 Plane spatial resolution

Using the reconstructed position, X_{rec} , on each plane of CR events, a linear fit was performed introducing an uncertainty of 2 mm in the x direction and of 1 mm in the z direction estimated from the maximum misalignment between planes. The distribution of α, the angle with the vertical of the muon track projection in the $x - z$ plane, for events with 2 adjacent bars fired in each plane is reported in Fig. 3.28. The shape of the distribution reflects the possible different combinations of couples of adjacent fired bars. The distribution of fit positions are shown in Fig. 3.29 for tracks with $\chi^2 < 10$ and $\alpha < 50$ mrad. Similar distributions are obtained for each plane indicating the uniformity of the response of adjacent bars.

In order to estimate the efficiency of a single plane we excluded it from the trigger during an acquisition run. Fitted tracks were computed from

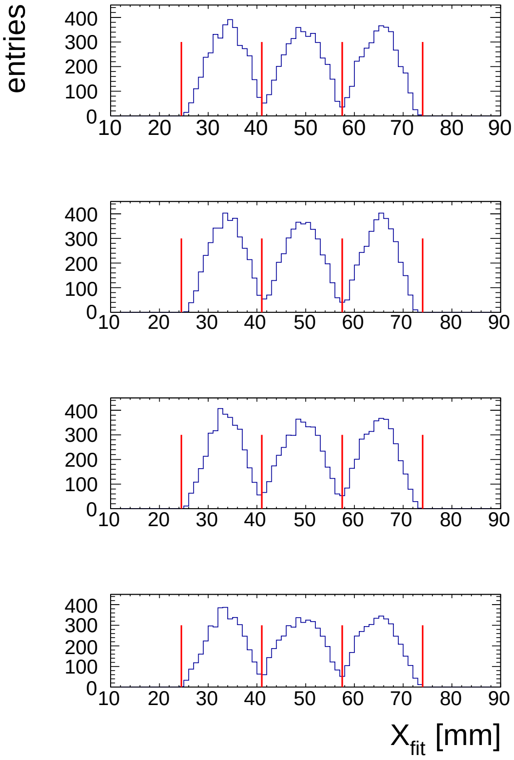

Figure 3.29: Distributions of fit positions in each plane for CR tracks with $\chi^2 < 10$ and $\alpha < 50$ mrad. Only tracks that crossed two adjacent triangular bars in each plane were selected. Red vertical lines indicate the fiber positions.

the positions reconstructed on the remaining planes participating in the trigger. Events with only two adjacent bars with a signal > 15 mV and $\alpha <$ 50 mrad were selected. In this way tracks that crossed the "left" pairs of adjacent bars (channels 2-4, 10-12, 9-11), the "central" pairs of adjacent bars (channels 4-6, 12-14, 11-13) and the "right" pairs of adjacent bars (channels 6-8, 14-16, 13-15) of Fig. 3.1 were selected. In the plane excluded from the trigger only events with signals in the corresponding pairs of adjacent bars crossed by the fitted track were selected, namely channels 1-3 for the "left" pairs, channels 3-5 for the "central" pairs and channels 5-7 for the "right" pairs. The average value of the plane efficiency, evaluated by the ratio of the number of selected events to the total number of triggered events, is 85%. In a similar manner the efficiency of a bar was determined by the ratio of the number of events with a signal > 15 mV in the bar to the total number of triggered events. This ratio was computed for each bar; the average of ratios, i.e. the average bar efficiency, is ~ 92 %. The values of the plane efficiencies and of the single bar efficiencies are reported in Table 3.3.

The plane spatial resolution was estimated by the differences between

	plane ϵ	single bar ϵ
“left” pairs	82.5%	91%
“central” pairs	87%	93.4%
“right pairs”	86%	92.7

Table 3.3: In this table are reported the efficiencies obtained for the bottom plane of module 1 for the different pairs of adjacent bars and the single bar efficiencies obtained for the bars of the bottom plane of module 1.

the reconstructed particle positions and the fit positions in that plane. The distribution of residuals in the bottom plane of module 2 is shown in Fig. 3.30 (a) (blue solid histogram). Only fitted tracks with $\chi^2 < 10$ and $\alpha < 50$ mrad were selected; a spatial resolution of 1.5 mm is obtained. Results for other planes are consistent with each other and range from 1.4 to 1.8 mm and are shown in Fig. 3.31. In Fig. 3.30 (b) the distribution of the residuals in the bottom plane of module 2 is reported versus the track inclination α.

A more complete MC simulation was done taking into account light transport in the bar and the PDE of the SiPM. Only muons impinging vertically on the detector plane were considered. The MC distribution of residuals is shown in Fig. 3.30 (a) (red dashed histogram): the standard deviation of the gaussian fit to the distribution is (1.4 ± 0.1)mm in good agreement with the data. The number of collected p.e. in a couple of adjacent bars is plotted in Fig. 3.32 versus the reconstructed position. A qualitative agreement with the experimental distribution of Fig. 3.26 (a) can be observed.

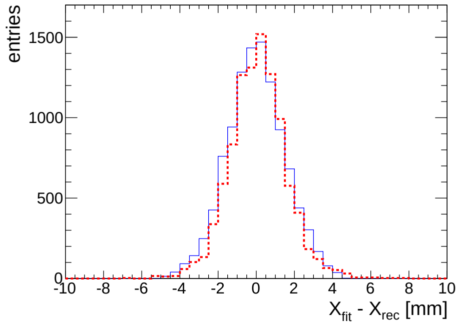

(a)

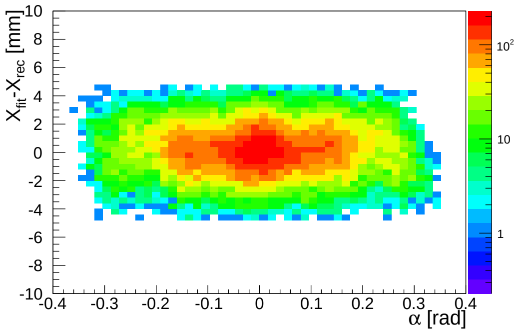

(b)

Figure 3.30: (a) Distribution of differences between the reconstructed and the expected positions as predicted by the fitted tracks, in the bottom plane of module 2 for events with 2 adjacent triangular bars with a signal > 15 mV in each plane. The spatial resolution obtained with data (blue solid histogram) is 1.5 mm to be compared with 1.4 mm MC based prediction (red dashed histogram). (b) Residuals between the reconstructed and the projected positions of fitted tracks vs. the track inclination for the bottom plane of module 2.

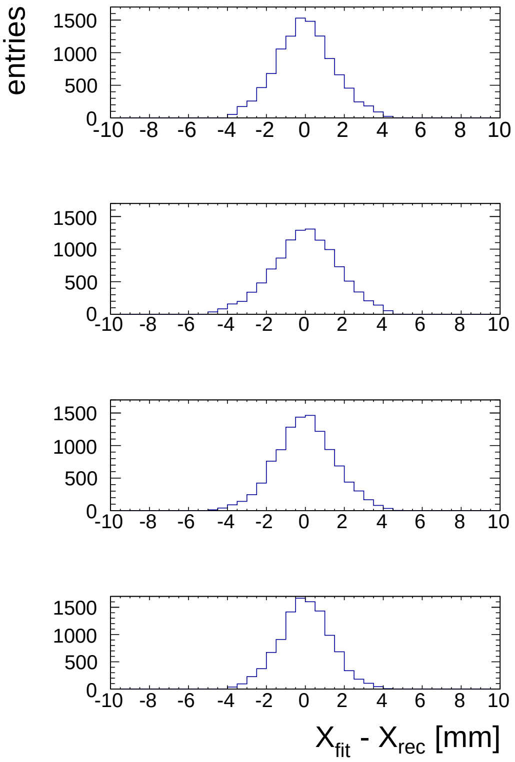

Figure 3.31: Distribution of differences between the reconstructed and the expected positions as predicted by the fitted tracks for each plane. The spatial resolution ranges from 1.4 to 1.8 mm.

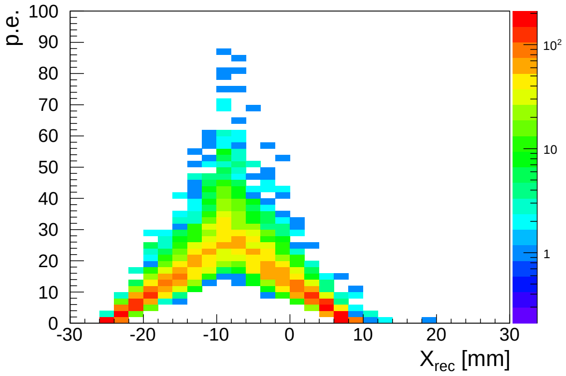

Figure 3.32: MC distribution of p.e. collected in a couple of adjacent bars vs. the reconstructed position.

Chapter 4

Beam test of a tracker prototype

Based on the results obtained testing the lab tracking prototype with CR muons, we developed a larger multiplane tracker to be tested with charged beams at the CERN *Proton Synchrotron* (PS). In this chapter I report about the construction of this prototype and the tests done at CERN.

4.1 The tracker prototype

The tracking system prototype is composed of 5 detector modules, each with 2 orthogonal X, Y scintillator strip planes (the Z coordinate aligned with the beam direction). Each plane is made of 16 triangular scintillator bars. The overall number of electronic channels is 160. The scintillator bars are 30 cm long and are of the same type as those used for the lab prototype described in chapter 3. In Fig. 4.1 (a) is shown a sketch of the tracker prototype.

In each bar the scintillation light is collected by a multicladding Y11 Kuraray [74] WLS fiber of 2 mm diameter, glued into the bar hole with RTV 615 optical glue (as described in chapter 3, Section 3.2). The fiber has an absorption peak at $\lambda = 430$ nm and an emission peak at $\lambda = 476$ nm shifting blue light to green; the attenuation length is > 3.5 m and the trapping efficiency is 5.4 %.

Each detector plane is contained in a black box of PVC (Polyvinyl Chloride) 0.4 cm thick. The box has 2 opposite caps: a cap covering the back of the bars is equipped with an aluminium foil to maximize light reflection and a frontal cap encloses the WLS fibers outgoing from the bars and coupled to SiPMs. The modules are at a distance of 25 cm from each other and are mounted on a movable structure with an height of 180 cm and an area of 140×130 cm^3 as shown in Fig. 4.1 (b). The tracking system can be placed at different distances from the beam pipe and at different angles with respect

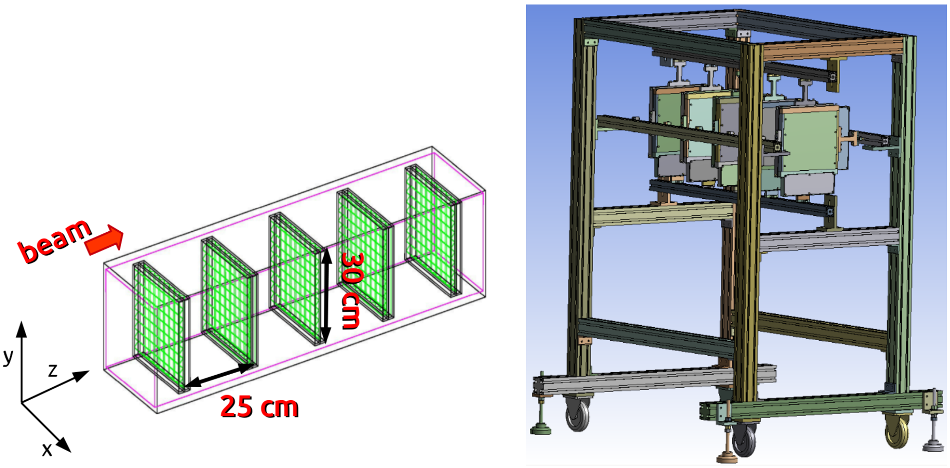

(a) (b)

Figure 4.1: (a) A sketch of the tracking system prototype. (b) The tracking system mounted on its movable support structure.

to beam.

Each detector bar is coupled to a SiPM (microFC - 30035 series) produced by SenSL [75]. The sensor active area is 3 × 3 mm^2, the cell size is 35 μm for a total of 4774 microcells and an overall fill factor of 64 %. The breakdown voltage, as reported in the datasheet, is (24.5 ± 0.5) V and the overvoltage ΔV_{ov} is allowed to range between 1 and 5 V. I measured the pulse height distribution of the dark current at T = 26 °C and $V_{bias} = (V_{bk} + \Delta V_{ov}) =$ 26.5 V which is shown in Fig. 4.2 for one SiPM. The total dark current rate is about 300 kHz. The analog signal from SiPM is sent to the front-end board before being amplified through a RG-403 triaxial cable (1 m long) which limits the electronic noise at a low level.

The SiPM is coupled to the WLS fiber through a custom connector (shown in Fig. 4.3) realized with a 3D printer by the Bologna INFN mechanic's workshop. In Fig. 4.4 is sketched the box containing a plane of scintillator bars. Black silicon was used at the junction between the front cap and the RG-403 cable to avoid light entering inside the box.

4.2 Front-end electronics

The SiPMs signals from a detector module were readout in analog mode by an EASIROC (*Extended Analogue SiPM ReadOut Chip*) chip [76]. It is a 32 channels fully analogue front end Application-Specific Integrated Circuit (ASIC) for the amplification and readout of SiPM signals.

A total of 5 EASIROC chips were used. Each chip acquires signals from 32 SiPMs of a pair of XY planes of one module: SiPM of bars dedicated

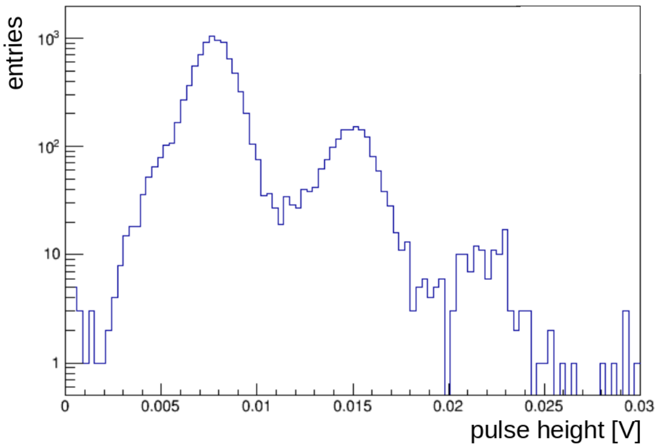

Figure 4.2: Pulse height distribution of the dark current for the SenSL MicroFC-30035 SiPM. The dark current rate, including contributions from other noise sources (i.e. cross talk and after pulses) is ∼ 300 kHz, with a cross talk probability of about 7%. The measurement was taken at T = 26 °C and V_{bias} = 26.5 V.

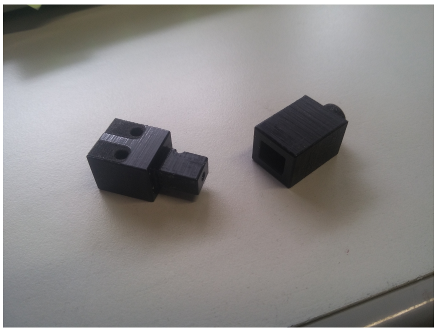

Figure 4.3: The connector used to couple the WLS fiber to the surface of the SiPM.

to the reconstruction of the Y coordinate were connected to the first 16 channels of EASIROC, while those dedicated to the reconstruction of the X coordinate were connected to the next 16 channels.

The architecture of the EASIROC analog core is shown in Fig. 4.5. In each channel, two separate electronic chains allow High and Low gain (HG/LG) of the signal in order to measure charge from 160 fC up to 320 pC, i.e. from 1 p.e. to 2000 p.e. for a SiPM gain of $\sim 10^6$. The high voltage of each channel can be individually tuned in order to equalize the gains by varying the bias voltage in a 8-bit DAC from 0 to 4.5 V. Each chain is composed of an adjustable preamplifier followed by a tunable *Slow Shaper* and a *Track & Hold* circuit. The schematic circuit of a track and hold cell is shown in Fig. 4.6 (a). The slow shaper integrates the signal providing a charge measurements while the track and hold unit stores the signal peak amplitude value for each channel (see Fig. 4.6 (b)). A third

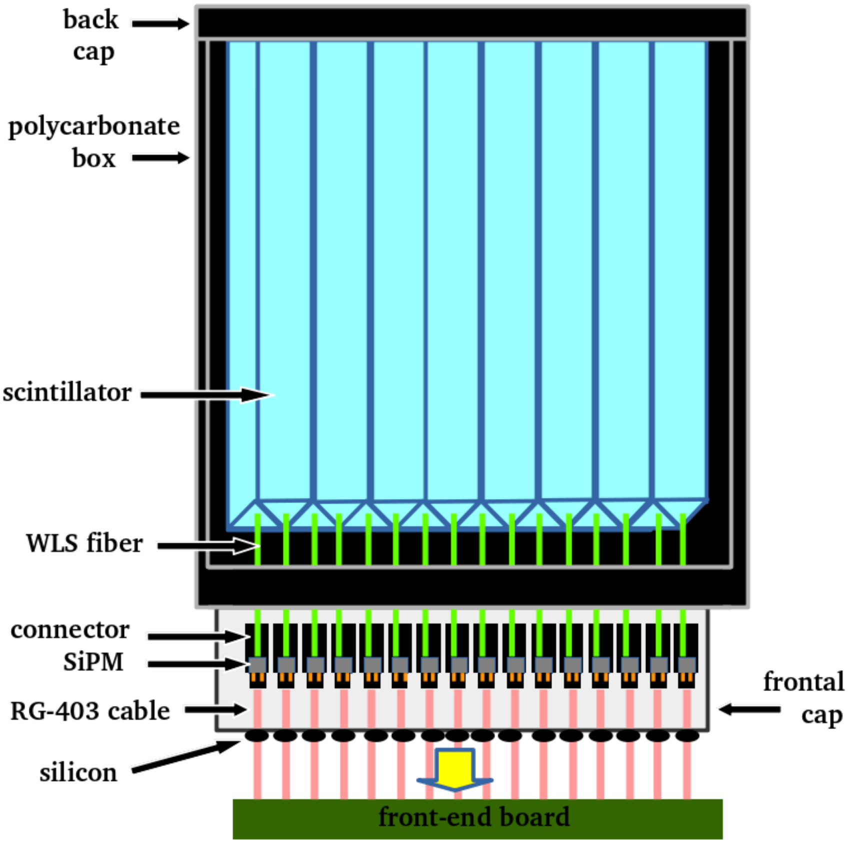

Figure 4.4: A sketch of a detector plane: it is composed of 16 adjacent scintillator bars inside a black PVC box. Fibers are coupled to SiPM through a connector and the analog signal is sent to the front-end board through a triaxial cable.

chain is implemented to generate a trigger using a fast shaper followed by a discriminator, set by a 10-bit DAC control register common to all the 32 channels (see Fig. 4.5).

The track and hold mechanism is reported in Fig. 4.7 (a) which shows an oscilloscope screenshot taken during an acquisition of CR events done to test the EASIROC operation mode. The screenshot shows the SiPM analog signal (green) after being amplified and shaped and the corresponding trigger signal (red). If the signal exceeds a threshold (set by the user through the 10-bit DAC control register) the track and hold signal (blue) saves the signal amplitude at its peaking time whose digitized level is represented in yellow. The timing of the track and hold signal has to be tuned properly in order to store the correct value of the signal amplitude.

EASIROC is integrated on a *Printed Circuit Board* (PCB) with an FPGA (*Field Programmable Gate Array*) to implement different trigger logics. The 32 channel triggers are sent to the FPGA that, according to the set threshold,

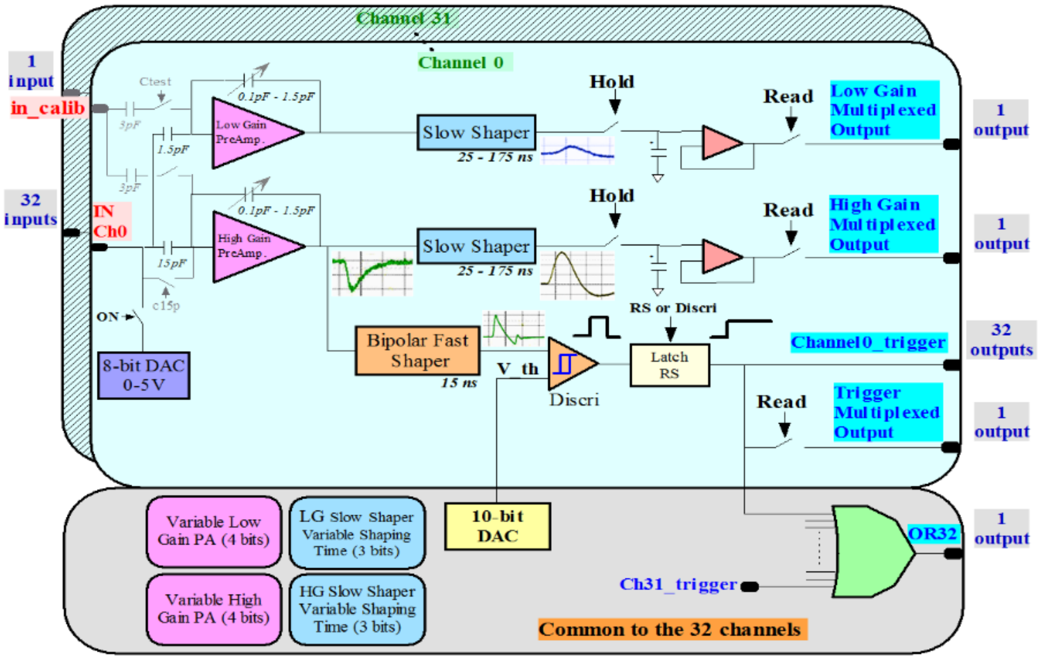

Figure 4.5: Architecture of the front-end EASIROC chip.

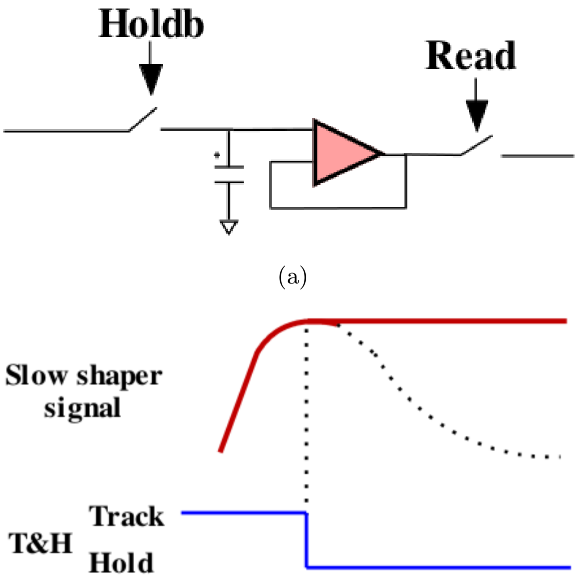

(a)

(b)

Figure 4.6: (a) Schematic of track and hold cell. (b) Track and hold working mode: the chip has to save the amplitude of the pre-amplified and shaped signal at its peaking time.

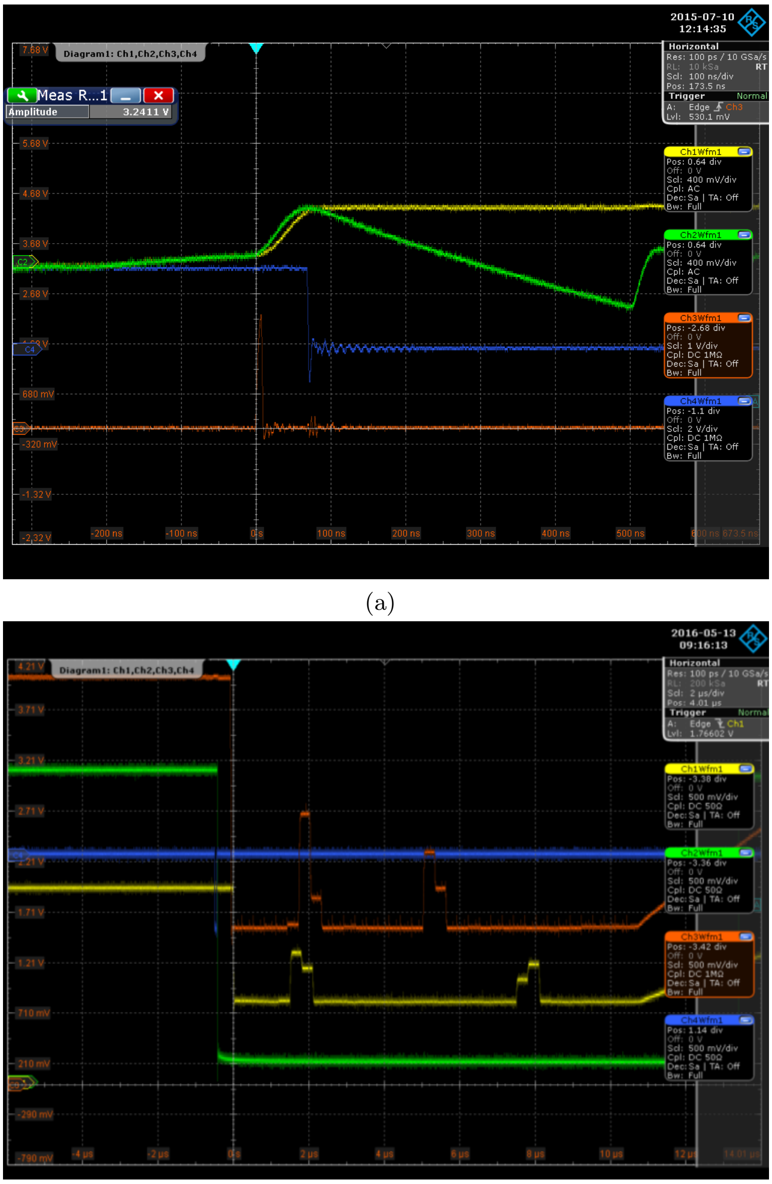

Amplitude 3.2411 V

2015-07-10
12:14:35

Horizontal
Res: 100 ps / 10 GSa/s
RL: 10 kSa RT
Scl: 100 ns/div
Pos: 173.5 ns
Trigger Normal
A: Edge Ch3
Lvl: 530.1 mV

Ch1Wfm1
Pos: 0.64 div
Off: 0 V
Scl: 400 mV/div
Cpl: AC
Dec: Sa | TA: Off
Bw: Full

Ch2Wfm1
Pos: 0.64 div
Off: 0 V
Scl: 400 mV/div
Cpl: AC
Dec: Sa | TA: Off
Bw: Full

Ch3Wfm1
Pos: -2.68 div
Off: 0 V
Scl: 1 V/div
Cpl: DC 1MΩ
Dec: Sa | TA: Off
Bw: Full

Ch4Wfm1
Pos: -1.1 div
Off: 0 V
Scl: 2 V/div
Cpl: DC 1MΩ
Dec: Sa | TA: Off
Bw: Full

(a)

2016-05-13
09:16:13

Horizontal
Res: 100 ps / 10 GSa/s
RL: 200 kSa RT
Scl: 2 µs/div
Pos: 4.01 µs
Trigger Normal
A: Edge Ch1
Lvl: 1.76602 V

Ch1Wfm1
Pos: -3.38 div
Off: 0 V
Scl: 500 mV/div
Cpl: DC 50Ω
Dec: Sa | TA: Off
Bw: Full

Ch2Wfm1
Pos: -3.36 div
Off: 0 V
Scl: 500 mV/div
Cpl: DC 50Ω
Dec: Sa | TA: Off
Bw: Full

Ch3Wfm1
Pos: -3.42 div
Off: 0 V
Scl: 500 mV/div
Cpl: DC 1MΩ
Dec: Sa | TA: Off
Bw: Full

Ch4Wfm1
Pos: 1.14 div
Off: 0 V
Scl: 500 mV/div
Cpl: DC 50Ω
Dec: Sa | TA: Off
Bw: Full

(b)

Figure 4.7: Oscilloscope screenshots of EASIROC signals: (a) the red signal is the trigger associated to a SiPM with a signal over threshold, the green signal is the analog output from that SiPM, the blue signal is the track and hold signal storing the value of the (green) signal amplitude at its peaking time and the yellow signal is the digitized output that contains the stored signal amplitude value; (b) the yellow and red signals are the High Gain Multiplexed Output from 2 detector modules (in the case shown here an event with a CR muon crossed 2 adjacent pairs of triangular bars in each plane), the green signal is the track and hold signal and the blue signal is the RSTB-READ generated when the track and hold is sent to the FPGA.

generates a common hold signal for the output readout. The following trigger conditions were implemented on the FPGA:

1. OR of the 32 triggers channels (OR32);
2. OR of the first 16 trigger channels (OR16 Low): at least one channel with a signal over threshold in the Y plane;
3. OR of the next 16 triggers channels (OR 16 High): at least one channel with a signal over threshold in the X plane;
4. AND between (OR16 Low) and (OR16 High).

These trigger signals are available on LEMO connectors in the standard TTL together with a signal (called RSTB-READ), generated in correspondence of the track and hold, which trigger the data acquisition (section 4.3). An input LEMO connector (HOLDB) is available to send to EASIROC a track and hold signal generated externally. In fact, is it possible to configure the FPGA in order to choose the hold command from the HOLDB connector or the OR32 (1).

The output of each channel is multiplexed on a common line thus providing a signal that contains the sequence of the 32 SiPMs signal amplitude values. This signal is available both in Low and High gain (*High* and *Low Gain Multiplexed Output*) from 2 LEMO connectors. The analog output of an EASIROC channel is also available from a LEMO connector, thus it is possible to select the channel through a proper register. In Fig. 4.7 (b) a screenshot of the oscilloscope during an acquisition run with 2 modules is shown: the High Gain Multiplexed Outputs from each module (yellow and red signals) are shown together with the track and hold (green) and the RSTB-READ (blue) signals.

A LabVIEW based software of National Instruments, developed by the LAL (Laboratoire de l'Accelerateur Lineaire) Tests group [77], commands the EASIROC chip and receives the output via USB connection. The PCB was developed by the Bologna INFN electronic group starting from the scheme of an evaluation board provided by Omega. The INFN PCB board has 32 input channels to connect the SiPM to the EASIROC and require a power supply of (-5,+5) V. A sketch of the PCB is shown in Fig. 4.8.

The evaluation board was used in preliminary data acquisitions and to test the EASIROC functionality. To this purpose the test board has 2 external ADCs allowing data acquisition. Through the LabView application is it possible to acquire and store data and to monitor online the data acquisition by histograms of (f.e.) the charge spectrum of a single channel (see Fig. 4.16 (b)) or the ADC value measured for each channel both for low and high gain output.

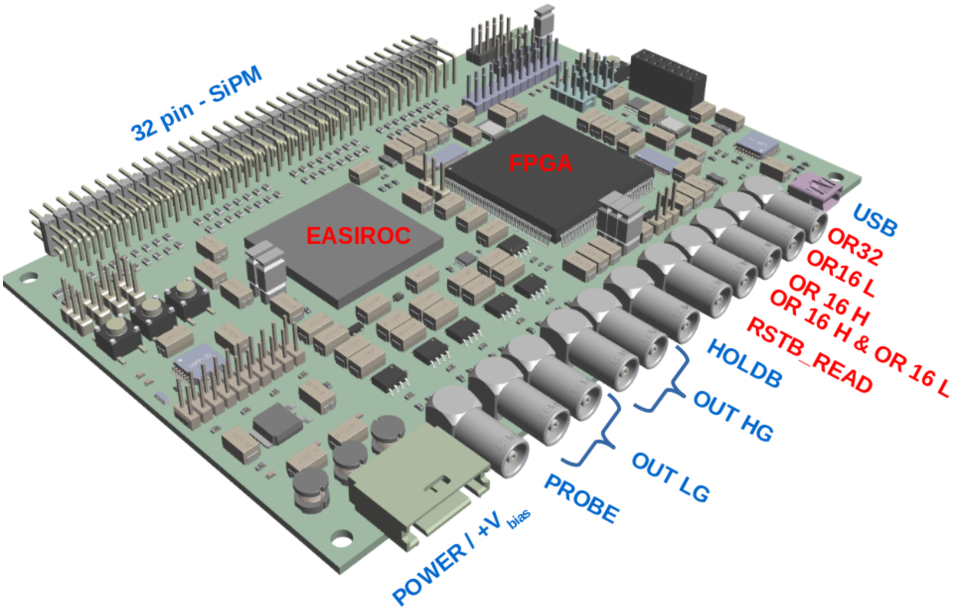

Figure 4.8: A sketch of the INFN PCB to access the EASIROC chip.

4.2.1 Trigger generation

The track and hold signal was generated externally according to the scheme shown in Fig. 4.9. The TTL trigger signal (OR16 Low) AND (OR16 High) from each front-end board is sent to a CAEN V976 module which is a 1-unit VME module housing four 4-input coincidence, fan in/fan out and NIM - TTL / TTL - NIM adapter sections. The trigger signals from modules 1 and 5 are sent to a unit of the V976 to form a coincidence (1 & 5), while triggers from module 2, 3 and 4 are sent in coincidence to another unit (2 & 3 & 4). During the beam test an enable signal from the control room was sent to each unit to select the detector modules participating to the trigger. In this way events with a signal over threshold in at least each corresponding detector plane could be selected.

Furthermore, a trigger system based on 2 couples of rectangular plastic scintillators coupled to PMTs (fingers), one upstream and the other downstream with respect to the tracking detector, was installed. This system allowed to select particles crossing a detector area of 3×3 mm^2. A threshold of 130 mV was applied to each scintillator signal.

The two coincidence signals, 1 & 5 and 2 & 3 & 4 were put in OR to a third unit of the V976. The corresponding NIM output signal was input to the START of a Dual Timer to open a gate ~ 15 μs wide thus generating the track and hold signal. The track and hold signal is sent to the FPGA through the input LEMO connector HOLDB of the front-end boards. Since

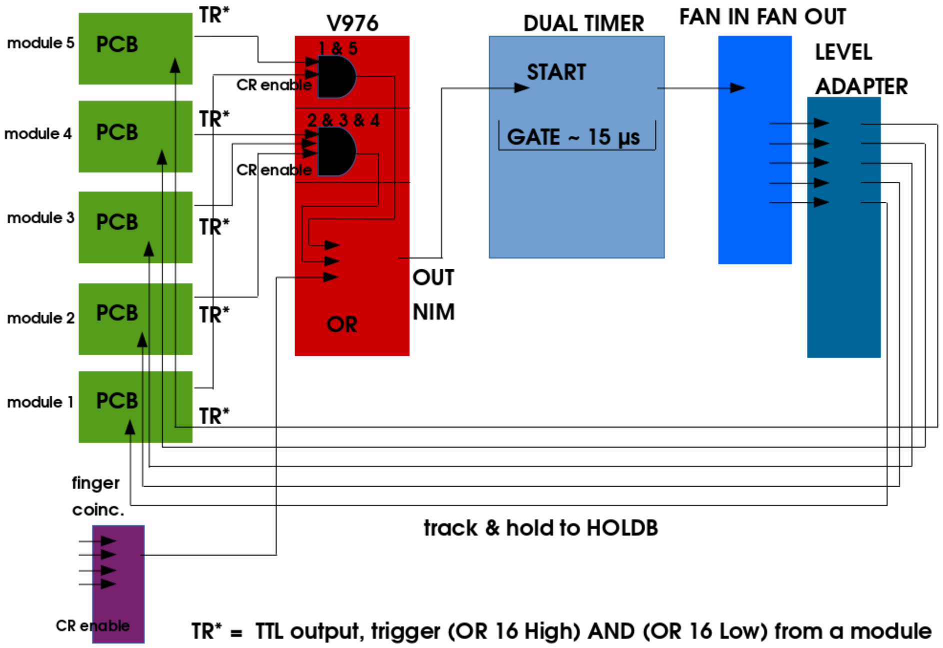

Figure 4.9: Scheme of the trigger chain for the generation of the track and hold signal.

the FPGA accepts only TTL signals, NIM Dual Timer signals are sent to a fan in fan out module to generate 5 identical outputs which are input to a Level Adapter module that converts NIM signals to TTL ones. Finally, 5 converted signals are input to the FPGA.

The timing of this trigger chain was properly optimized by means of an oscilloscope in order to generate the track and hold at the peaking time of the shaped analog signal.

4.3 DAQ

I contributed to the development of the DAQ readout. The multiplexed outputs from front-end boards were acquired by means of an 8 channels waveform digitizer V1720 with a sampling rate of 250 MS/s. Only the High Gain Multiplexed Output was acquired. The 5 waveforms from the front-end boards were input to the digitizer channels and in order to acquire all the 32 SiPMs signals contained in a waveform, the time acquisition window was 16 μs wide. Starting from the trigger time, the signal is acquired every 4 ns and 4096 voltage levels are stored in the digitizer memory. Fig. 4.10 shows the waveform acquired by one digitizer channel, which contains 32 multiplexed SiPMs signals peak values, the first 16 values corresponding to the 16 SiPMs channels of the Y-plane, while the second set of 16 values to SiPMs channels of the X-plane.

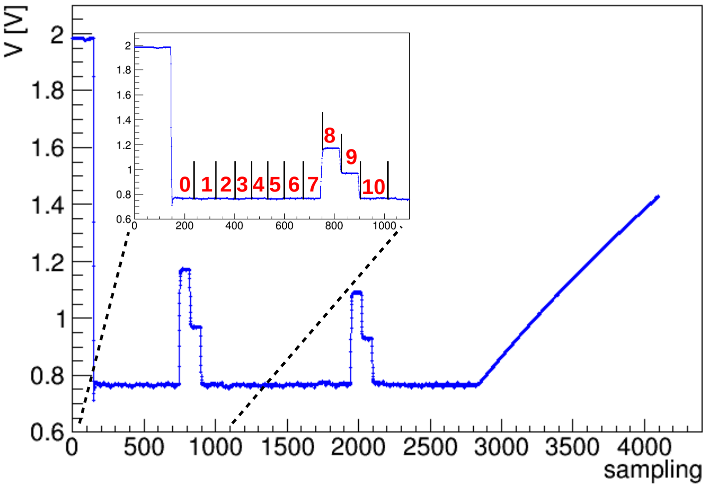

Figure 4.10: Waveform acquired by a digitizer channel. The waveform is a sequence of 32 multiplexed SiPMs signals peak values. The inset is a zoomed in portion of the WFD. Red numbers separated by black lines indicate the corresponding EASIROC channel.

The data acquisition is done according to the scheme shown in Fig. 4.11. The RSTB-READ signal is generated once the track and hold signal is sent to a board. The RSTB-READ is sent to a level adapter that converts it into the standard NIM. Then the converted RSTB-READ signal is sent to the START of a dual timer opening a gate 40 ms wide. Finally, the gate signal is input to the digitizer to trigger the data acquisition.

The data stored in the digitizer memory are acquired by a DAQ readout application. The digitizer is connected to a PC through a V2718 VME bridge via optical link. The readout program was developed under Windows operating system. The program checks asynchronously (with a system timer of 25 ms) if there are data available in the digitizer memory and then initializes a data readout BLT (*Block Transfer*) cycle, clearing the digitizer memory that can be used at next cycles. The DAQ program can acquire up to $\sim$ 400 particles/spill. The DAQ program provides a user interface (see Fig. 4.12) which allows to set, for example, the number of events/run and the digitizer configuration (number of post trigger samples, enable/disable channels, the number of buffers, etc.). By default the digitizer configuration allows to acquire 5 channels and for each channel $\sim$ 4000 samples after the trigger time are stored. The typical event size is $\sim$ 40 kB/trigger, i.e. $\sim$ 16 MB/spill. The digitizer *raw-data* are stored in binary files and the size of each data file is limited to 1 GB. The DAQ program also has the possibility to run in "auto start" mode. In this modality, when a data file reaches the size of 1 GB, the program starts automatically the acquisition storing data

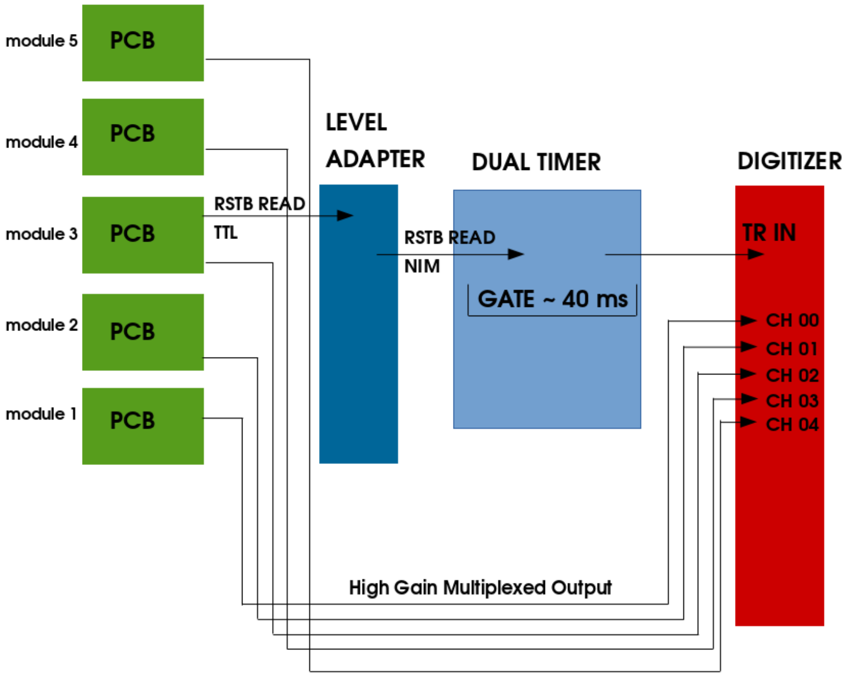

Figure 4.11: Scheme of the generation of the trigger to be sent to the digitizer.

in a new file.

Furthermore, the DAQ application counts at every BLT cycle the trigger signals that were input to a scaler. The trigger signals recorded by the scaler, reported in table 4.1, are: the trigger OR 16 Low and High of each detector module (trigger 2 and 3 described in section 4.2), the SPILL, the coincidence between 2 scintillator counters (PM) located after the beam pipe, the coincidence between two pairs of finger scintillators (a pair upstream and a pair downstream with respect to the tracking system), the RSTB-READ signal which is used to trigger the digitizer acquisition, the coincidence 1 & 5 and 2 & 3 & 4.

4.4 Assembling and testing of detector modules

The detector planes of the tracker prototype were assembled in Bologna inside PVC boxes. Each detector plane was tested with cosmic rays. For this purpose the 16 plane channels were input to the EASIROC. The FPGA was programmed so to select coincidences of pairs of adjacent channels[1] (the

---

[1] (ch00 AND ch01) OR (ch01 AND ch02) OR (ch02 AND ch03) OR (ch03 AND ch04) OR (ch04 AND ch05) OR (ch05 AND ch06) OR (ch06 AND ch07) OR (ch07 AND ch08) OR (ch08 AND ch09) OR (ch09 AND ch10) OR (ch10 AND ch11) OR (ch11 AND ch12) OR (ch12 AND ch13) OR (ch13 AND ch14) OR (ch14 AND ch15)

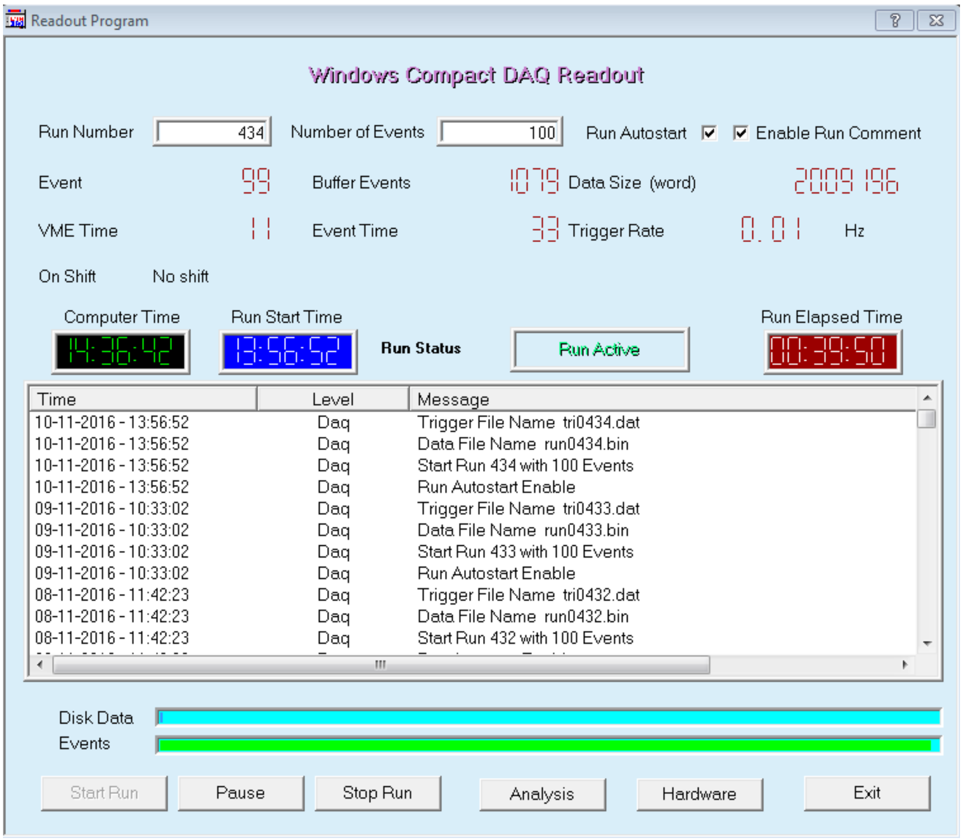

Run Number 434 Number of Events 100 Run Autostart ☑ ☑ Enable Run Comment

Event 99 Buffer Events 1079 Data Size (word) 2009196

VME Time 11 Event Time 33 Trigger Rate 0.01 Hz

On Shift No shift

Computer Time 14:36:42 Run Start Time 13:56:52 **Run Status** Run Active Run Elapsed Time 00:39:50

Time	Level	Message
10-11-2016 - 13:56:52	Daq	Trigger File Name tri0434.dat
10-11-2016 - 13:56:52	Daq	Data File Name run0434.bin
10-11-2016 - 13:56:52	Daq	Start Run 434 with 100 Events
10-11-2016 - 13:56:52	Daq	Run Autostart Enable
09-11-2016 - 10:33:02	Daq	Trigger File Name tri0433.dat
09-11-2016 - 10:33:02	Daq	Data File Name run0433.bin
09-11-2016 - 10:33:02	Daq	Start Run 433 with 100 Events
09-11-2016 - 10:33:02	Daq	Run Autostart Enable
08-11-2016 - 11:42:23	Daq	Trigger File Name tri0432.dat
08-11-2016 - 11:42:23	Daq	Data File Name run0432.bin
08-11-2016 - 11:42:23	Daq	Start Run 432 with 100 Events

Figure 4.12: Screenshot of the user interface of the DAQ readout program which allows different settings.

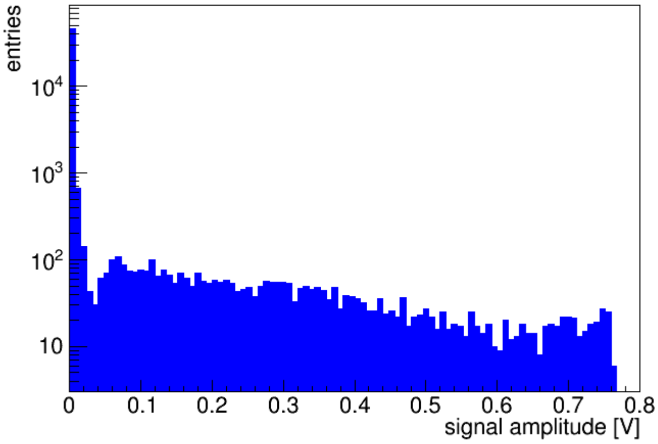

Figure 4.13: Signal amplitude distributions of cosmic rays in one detector plane channel measured triggering on coincidences of couples of adjacent bars.

scaler channel	trigger signal
Ch00	OR 16 Low module 1
Ch01	OR 16 High module 1
Ch02	OR 16 Low module 2
Ch03	OR 16 High module 2
Ch04	OR 16 Low module 3
Ch05	OR 16 High module 3
Ch06	OR 16 Low module 4
Ch07	OR 16 High module 4
Ch08	OR 16 Low module 5
Ch09	OR 16 High module 5
Ch10	SPILL
Ch11	PM
Ch12	fingers
Ch13	RSTB-READ
Ch14	1 & 5
Ch15	2 & 3 & 4

Table 4.1: Trigger signals sent to a scaler at every BLT cycle.

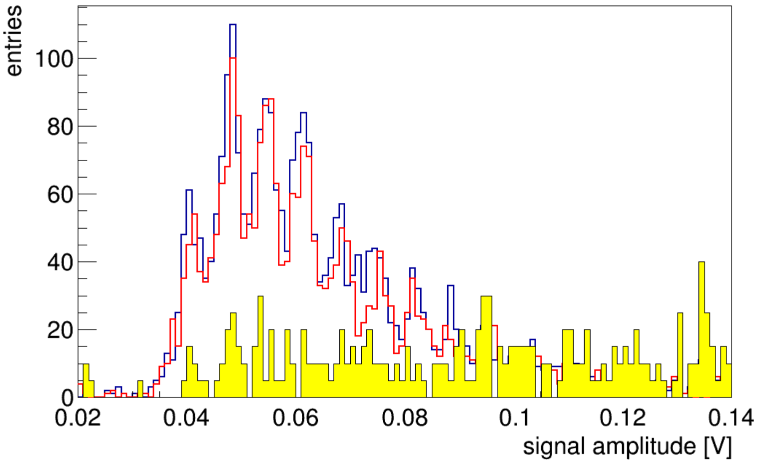

Figure 4.14: Signal amplitude distributions measured with the radioactive source positioned at 5 cm (blue histogram) and 25 cm (red histogram) from the SiPM. The yellow distribution is the signal amplitude spectrum with no source.

unused EASIROC channels were disabled). The trigger threshold for each channel was set to $\sim$ 35 mV and about 50000 events were acquired. The signal amplitude distribution of CR from one channel is shown in Fig. 4.13.

Using a radioactive source I checked the dependence of the signal amplitude from the particle crossing position along the bar. The source was

Figure 4.15: Metal cap used to inject laser pulses into the scintillator bars from the side opposite to the SiPM.

positioned on the top of a plane box in correspondence of a couple of scintillator strips (ch01 and ch02). Channels ch00, ch01, ch02 and ch03 (ch00 and ch03 adjacent to ch01 and ch02 respectively) were enabled and their threshold set at 35 mV. The trigger signal (ch00 AND ch01) OR (ch02 AND ch03) was sent to the digitizer to start the data acquisition. I measured the signal amplitude spectrum of channel 01 (shown in Fig. 4.14) positioning the source at $\sim$ 5 cm (blue histogram) and at $\sim$ 25 cm (red histogram) from the SiPM. About 5000 events were acquired at each position. In Fig. 4.14 the signal amplitude distribution of CR events (with no source) is also shown (yellow histogram). A similar behaviour is observed for the other bar (channel 02). No significant difference between the two source configurations is observed. This proves that the signal is independent on the longitudinal position along the bar, as expected by comparing the fiber attenuation length ($>$ 3.5 m as reported in the datasheet) with the length of the scintillator (30 cm).

Each detector channel was calibrated by injecting laser pulses into the scintillator bar, as described in section 3.2.1. A metal cap (shown in Fig. 4.15) was used to close the back end of the box plane. Holes in the cap are used to drive the laser fiber so to inject pulses on the end surface of the bars opposite to the one with the SiPMs. About 5000 laser pulse events were acquired for each bar obtaining a signal amplitude spectrum as the one shown in Fig. 4.16 (a). In this case the high gain multiplexed output was acquired by the digitizer. The signal amplitude spectrum shown in Fig. 4.16 (b) was obtained acquiring events by the LabView application.

Equalization factors obtained for each channel (Fig. 4.17) were determined using the procedure described in section 3.2.1.

4.5 Beam test at the CERN PS

The apparatus was tested with charged beams at the CERN PS T9 beamline located at the CERN East Hall facility [78]. The 24 GeV/c primary proton beam from the PS accelerator impinges on a target (aluminium or

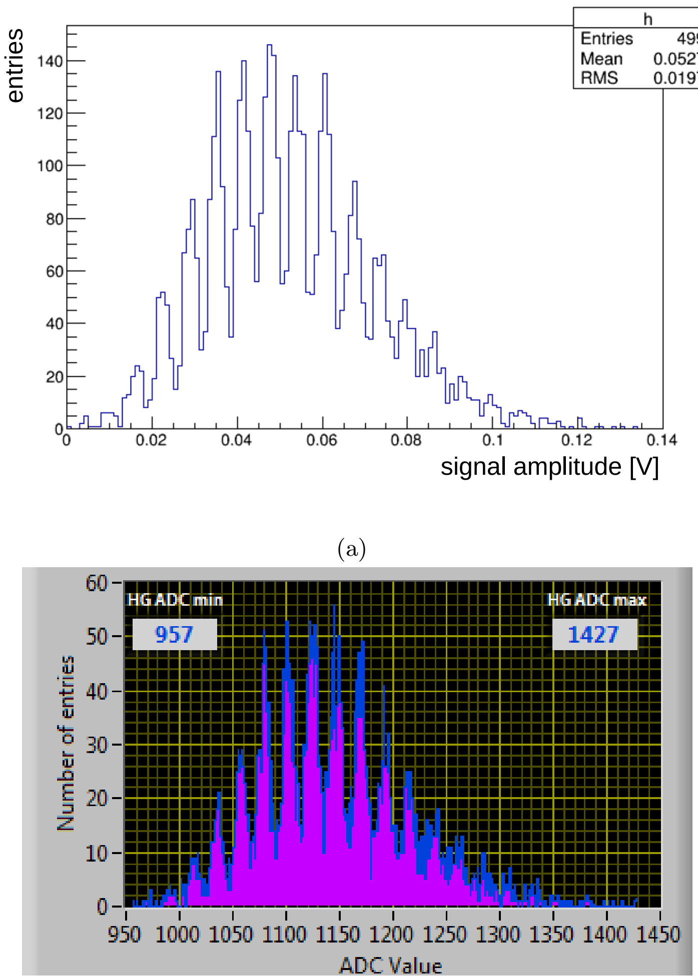

(a)

(b)

Figure 4.16: Signal amplitude spectrum obtained injecting laser pulses into a detector channel. Measured values were acquired by the digitizer (a) and by the LabView based application (b).

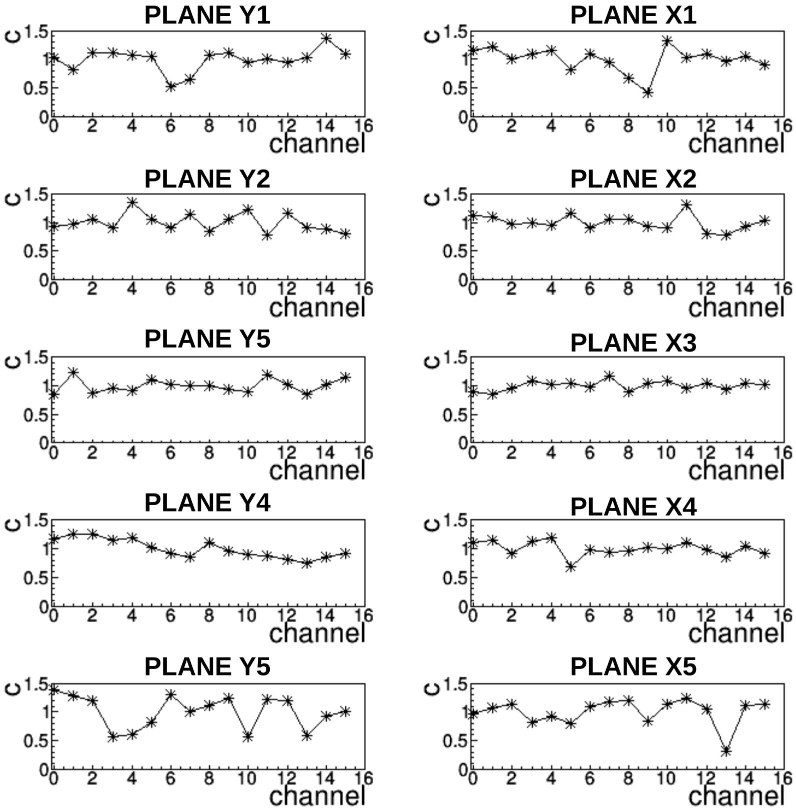

Figure 4.17: Equalization factors of different detector planes obtained injecting laser pulses into each detector channel.

beryllium) producing secondary particles for the T9 beamline. The line transports either positive or negative particles in the momentum range between 0.5 and 10 GeV/c with a momentum resolution of ~ 0.5 %. Depending on the beam momentum and charge the beam contains pions, (anti)-protons, electrons or positrons, and at the percent level, also kaons and muons. For the negatively charged beam, the fraction of electrons can be as high as 80% for $p = 0.5$ GeV/c dropping to 5% at 5 GeV/c, for the “electron-enriched” target and to few per mil when the “hadron-enriched” target is used. A charged beam produced with a “hadron-enriched” target has been used during the test. This choice allows to minimize the fraction of showering electrons. The energy spectra in negative and positive beam polarities are shown in Fig. 4.18 (a) and 4.18 (b). In Tab. 4.2 are shown the fluxes/spill of different beam components at different energies and beam polarities. The maximum particle flux per spill was 10^6, achieved at 10 GeV/c positive beam. For negative beams the rates are typically 2-3 times lower dropping significantly at lower energy. The beam is delivered uniformly in time over a

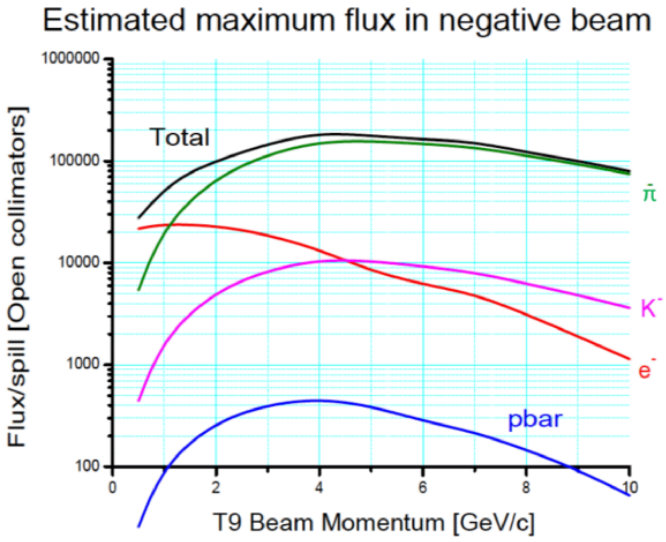

(a)

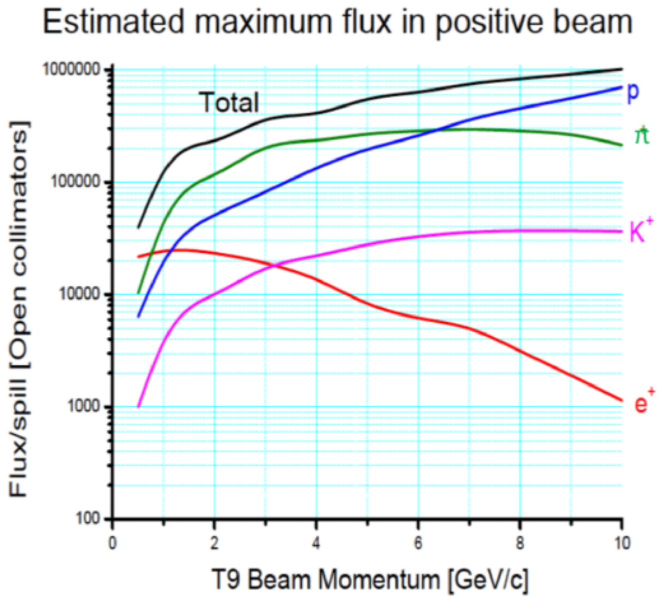

(b)

Figure 4.18: Maximum flux per spill in negative (a) and positive (b) beam polarity. The spectra show the beam composition at different energies.

burst of 0.4 seconds (*spill*) and there is typically a burst each 15 seconds. The beam travels ∼ 55 m before entering in the experimental area.

At the T9 beamline two collimators can be configured to filter the particles of the beam. Depending on its opening a horizontal collimator changes the width of the particle momentum distribution. A vertical collimator on the other hand filters the particles according to their initial angle on leaving the

E (GeV)	**negative beam (flux/spill)**				**positive beam (flux/spill)**			
	e^-	π^-	$\overline{p}$	K^-	e^+	π^+	p	K^+
1	$2{\cdot}10^4$	$2{\cdot}10^4$	$1{\cdot}10^2$	$2{\cdot}10^3$	$2.5{\cdot}10^4$	$4{\cdot}10^4$	$2{\cdot}10^4$	$3{\cdot}10^3$
5	$9{\cdot}10^3$	$1.7{\cdot}10^5$	$4{\cdot}10^2$	$1{\cdot}10^4$	$9{\cdot}10^3$	$2.7{\cdot}10^5$	$2{\cdot}10^5$	$3{\cdot}10^4$
10	$1{\cdot}10^3$	$8{\cdot}10^4$	50	$4{\cdot}10^3$	$1{\cdot}10^3$	$2{\cdot}10^5$	$7{\cdot}10^5$	$4{\cdot}10^4$

Table 4.2: Flux/spill of different beam components at different energies and beam polarities.

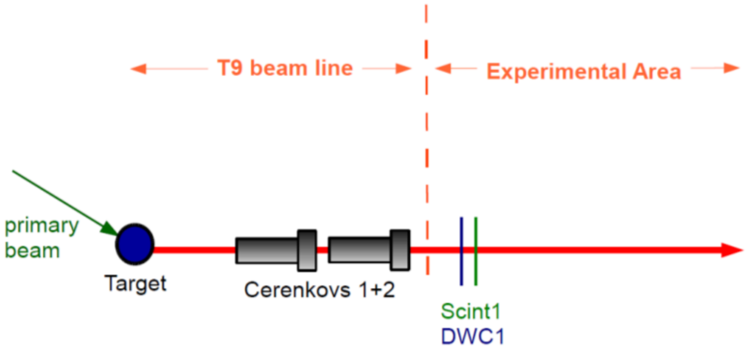

Figure 4.19: A sketch of the T9 beam line setup to monitor the beam: it consists on two cherenkov counters, two scintillator counters and one delay wire chamber.

target.

By means of a beam stopper is it possible to select only muons. Beam stoppers are massive blocks of absorber material that are used to stop all the beam particles except the muons.

Along the T9 beamline detectors are available to monitor the beam profile and the composition (Fig. 4.19). A delay wire chamber (DWC) was used to monitor the beam X-Y profile with a spatial resolution of 100-200 μm.

The beam has approximately a circular cross section of about 2 cm diameter at the focal plane. The beam focus position can be changed by changing the current of quadrupole magnets.

4.6 Data taking

The assembly of the tracker prototype in its support structure was done at the CERN East Area facility. A picture of the system placed along the T9 beam line is shown in Fig. 4.20.

The apparatus was placed at $\sim$ 7 m from the beam pipe and exposed to electrons, muons and pions in the 0.5-10 GeV energy range. The detector alignment with respect to the beam was adjusted by a level laser in order to have the X and Y planes orthogonal to the beam with an accuracy of few

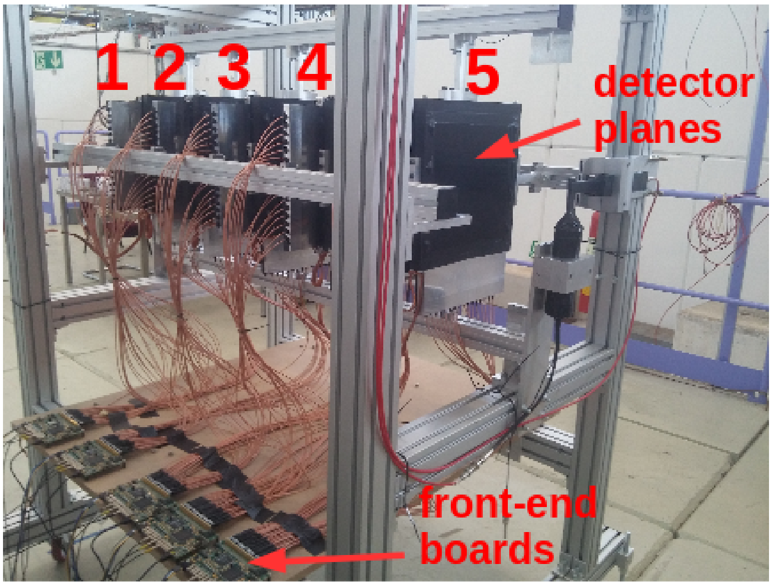

Figure 4.20: A picture of the tracking system prototype assembled on its support structure at the T9 experimental area (numbers indicate the modules).

particles	momentum (GeV/c)	focusing (m from DWC)
μ^+	0.5, 1, 3, 5, 10	1
μ^-	5, 10	1
e^-	0.5	1
π^+	1,5	0, 1, 2, 4.5, 7, 9.5 (at 5 GeV/c only)
π^-	1, 5, 10	1

Table 4.3: Beam configurations used during the test with the tracking system placed at ~ 7 m from the beam pipe.

mrad.

Since the T9 control room is far from the experimental area (~ 30 m), the PC dedicated to the data acquisition was located in the experimental area, while the online data monitoring was performed from the control room using another PC (Linux OS, used also for data storage) connected via remote desktop to the DAQ PC.

Overall about 3.6 million of events were recorded in 320 runs, with different beams (listed in Table 4.3) and different trigger selections. In table 4.3 are reported the main characteristics of different beams. From the control room it was possible to set the beam focusing and the particle energy.

Twelve trigger configurations were used, namely (numbers indicate the modules):

1. 1 AND 5 with all channels enabled;

2. 2 AND 3 AND 4 with all channels enabled;
3. 2 AND 3 AND 4 with only 6 channels enabled for each module, 3 in the X plane and 3 in the Y plane;
4. FINGERS with all channels enabled;
5. (1 AND 5) OR (2 AND 3 AND 4) OR FINGERS with all channels enabled;
6. (1 AND 5) OR FINGERS with all channels enabled;
7. 1 AND 2 AND 3 AND 4 AND 5 with all channels enabled;
8. 2 AND 3 AND 4 AND 5 with all channels enabled;
9. 1 AND 3 AND 4 AND 5 with all channels enabled;
10. 1 AND 2 AND 4 AND 5 with all channels enabled;
11. 1 AND 2 AND 3 AND 5 with all channels enabled;
12. 1 AND 2 AND 3 AND 4 with all channels enabled;

Trigger configurations 8, 9, 10, 11 and 12 were used to estimate the efficiency of each module. Several runs were done with different thresholds (common to all channels) applied to EASIROC discriminators, i.e. 20 mV, 30 mV, 45 mV, 60 mV and 70 mV. The capacitance of the preamplifier was set to 200 fF and the bias voltage was set to 26.5 V.

4.6.1 Data monitoring

I developed a a software application to monitor the data taking. It was developed under Linux OS with a graphical user interface (GUI) based on the *Qt toolkit*[2]. This interface allows the user to choose among different type of histograms and displays to monitor the data acquisition. The ROOT toolkit [80] (C++ language) is used for histogramming and graphing. An example of the user interface is shown in Fig. 4.21: two different operation mode are available, an *offline* detector monitor and an *online* detector monitor.

The offline detector monitor processes the raw data and generates a ROOT data file as described in 5.1.

The online detector monitor processes the digitizer waveform generating histograms and event displays. Available histograms are the signal amplitude distribution for each channel and the *hit map* on each X and Y plane. The hit map (see Fig. 4.22) shows for each plane the distribution of channels

---

[2] Qt is an application framework widely used for developing application software with graphical user interface [79]. Qt uses standard C++ language.

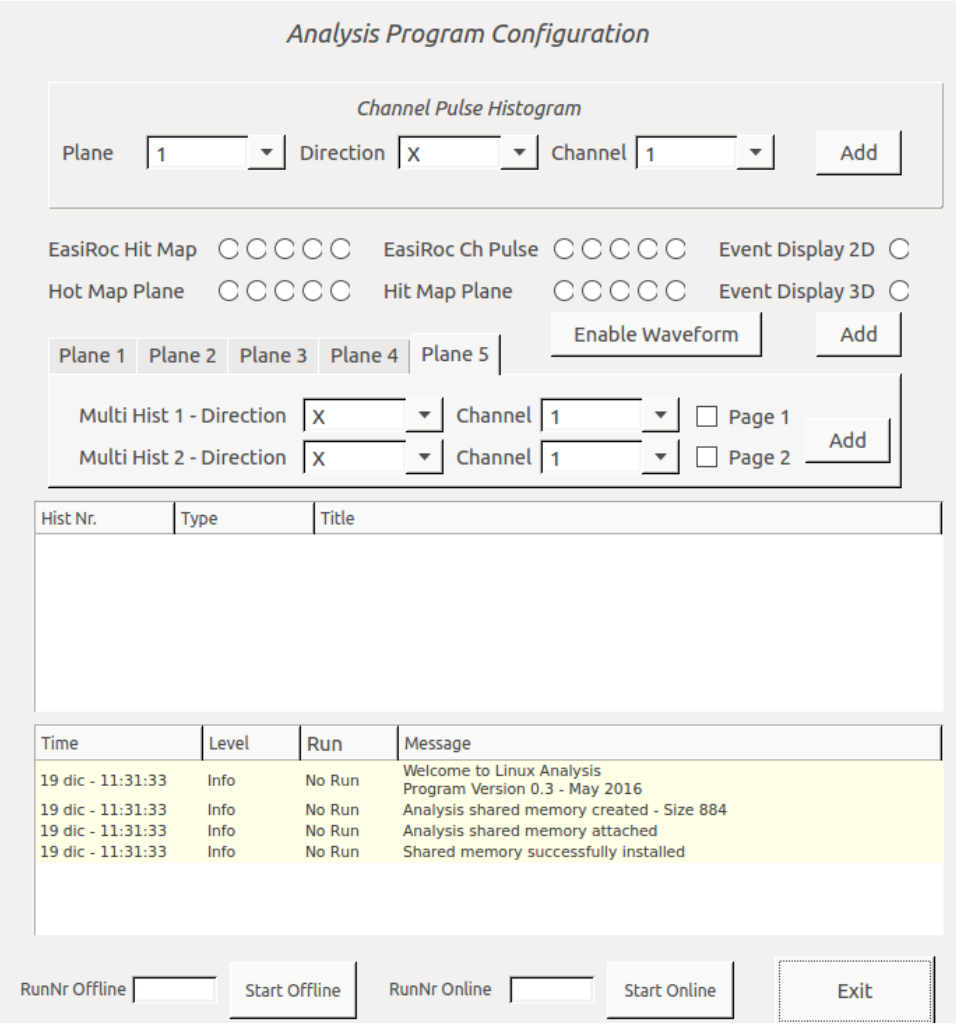

```
Time                Level   Run      Message
19 dic - 11:31:33   Info    No Run   Welcome to Linux Analysis
                                     Program Version 0.3 - May 2016
19 dic - 11:31:33   Info    No Run   Analysis shared memory created - Size 884
19 dic - 11:31:33   Info    No Run   Analysis shared memory attached
19 dic - 11:31:33   Info    No Run   Shared memory successfully installed
```

Figure 4.21: The user interface of the Qt application developed to monitor the data acquisition during the beam tests. The application allows an online detector monitor and an offline detector monitor.

with a signal over threshold *th* (that can be set by the user). Fig. 4.22 is referred to a run at 5 GeV/c in negative beam polarity. In this case, as reported in Tab. 4.2, the leading beam component consists of π^-. The focus distance from the first detector module was set at ~ 6 m, the beam is more divergent in the X direction and is more collimated in the Y direction (~ 25 cm wide along the X direction and ~ 5 cm along the Y direction). The online analysis program can display single event information, as: EASIROC channel displays, digitizer waveforms, XZ, YZ event views and 3D event display. In Fig. 4.23 is shown an example of the display of signal amplitude distributions (X-,Y-channels) for each EASIROC board (data refer to a particle crossing 2

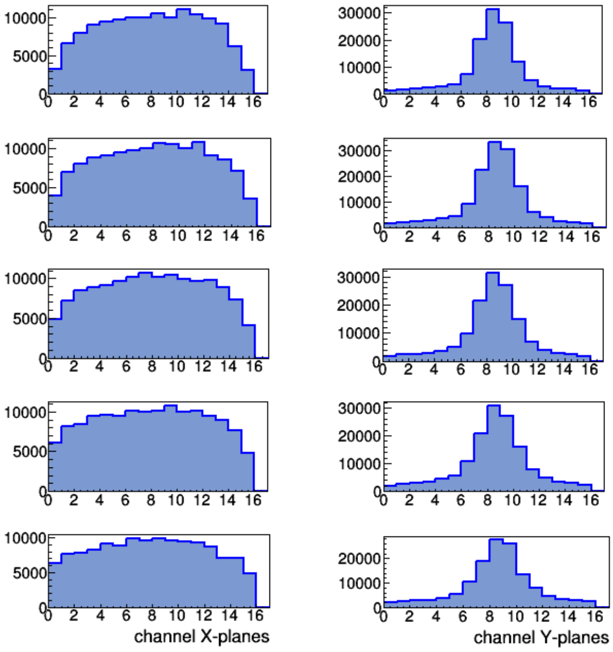

Figure 4.22: X and Y hit distributions on each detector plane showing channels with signal amplitude over threshold.

adjacent bars in each detector plane). In Fig. 4.24 is shown the 2D event display for the same event (planes are numbered from bottom , # 1, to top). The color code for triangular bars indicates if there was: no signal or signal under threshold (white bars), signal amplitude $th < \Delta V \leq 20$ mV (black bars), signal amplitude 20 mV $< \Delta V \leq$ 80 mV (green bars) and signal amplitude $\Delta V >$ 80 mV (red bars).

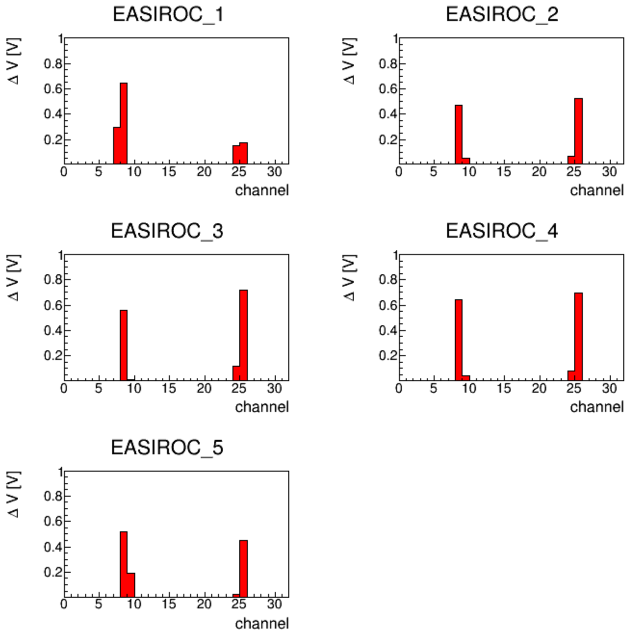

Figure 4.23: Online monitor displays of signal amplitudes in each channel.

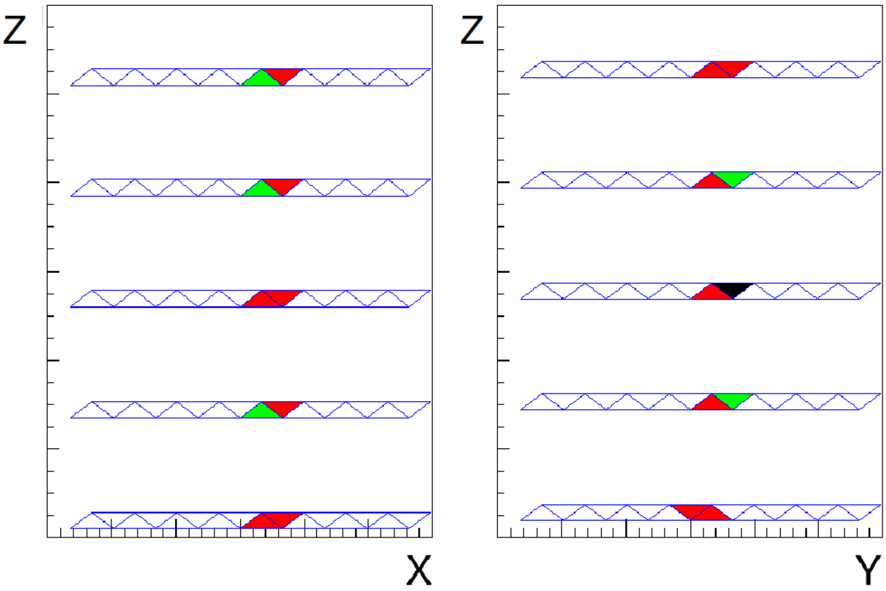

Figure 4.24: Event display in the XZ and YZ views for a particle crossing a couple of two adjacent bars producing signals with an amplitude over the th threshold in each detector plane.

Chapter 5

Data analysis and results

In this last chapter the analysis procedure performed on the beam test data is presented. The spatial resolution and the efficiency of the tracker modules are eventually derived.

5.1 Data analysis

The data analysis chain was divided in different steps as in the scheme of Fig. 5.1:

- raw to root conversion of data files and digitizer waveforms processing;
- *clusters* identification;
- event selection for track reconstruction;
- particle crossing points reconstruction and evaluation of the spatial resolution.

5.1.1 Raw to root data conversion

Raw data are processed by an analysis program based on the ROOT toolkit. This application generates an output root file with a *ntuple* that contains the digitizer waveforms (see Fig. 4.10) and a *TTree object* with the "processed" *event*. Each entry of the waveform ntuple is a digitizer sampling and the ntuple contains the following information:

- the event id;
- the digitizer channel;
- the index of the sampling;
- the voltage value of the digitizer sampling.

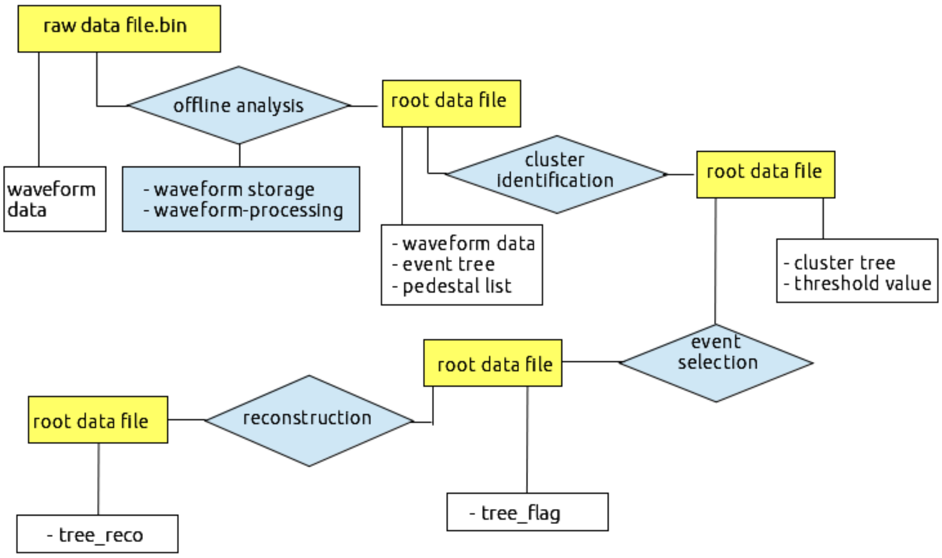

Figure 5.1: In the scheme is outlined the analysis chain: raw to root conversion, *clusters* identification, event flagged and position reconstruction in each plane.

The event tree (each entry is a digitizer event) contains:

- the event id;
- the digitizer timeStamp (i.e. the time of the event);
- the voltage value in each detector channel;
- the signal amplitude in each detector channel.

The channel voltage is extracted from the digitizer waveform: with reference to Fig. 4.10, for each channel (regions delimited by black lines) the voltage value is calculated as the mean of the voltage values over 15 sampling points ($\sim$ 75 samplings/channel).

In order to determine the signal amplitude of a channel, it is necessary to determine its *pedestal*, that is the average electronic noise of that channel. With reference to the waveform shown in Fig. 4.10, for each channel an offset value (that may vary among channels) has to be subtracted to the channel voltage to determine the signal amplitude. This offset can vary over time, thus the channel pedestal can vary run by run. The channel pedestals of different EASIROC boards are shown in Fig. 5.2 for several data taking runs. An estimate of the pedestal can be done by pre-processing the waveforms run by run, creating a list that contains the different pedestals to take into account for the different runs. The uncertainty on the pedestal, evaluated as the RMS of pedestal distribution, is about ± 1 mV .

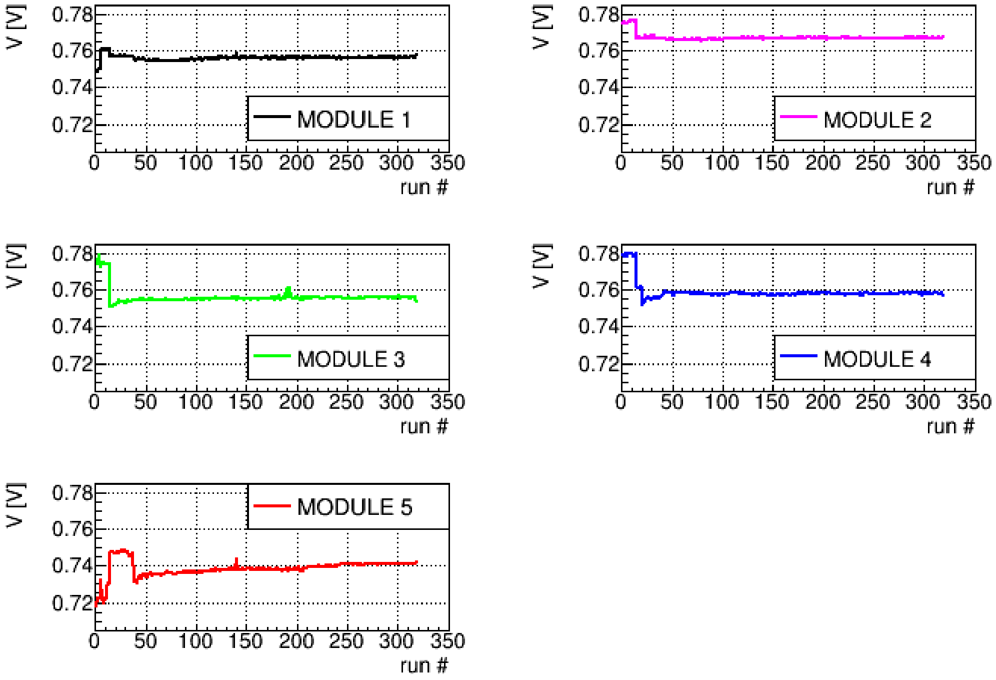

Figure 5.2: Plots showing the pedestal values for different data taking runs in channels of different EASIROC boards.

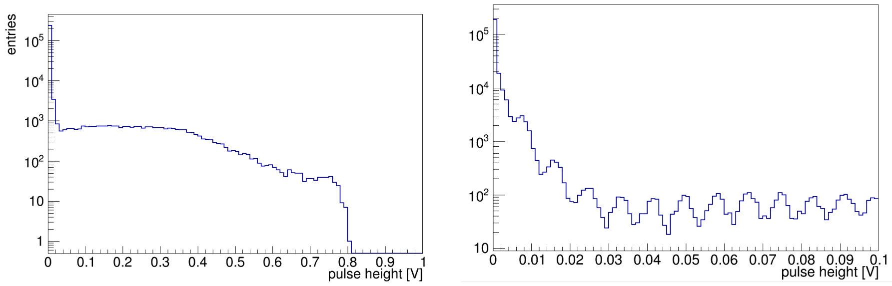

(a) (b)

Figure 5.3: (a) Distribution of a channel signal amplitude for 5 GeV/c μ^-. (b) Zoomed-in region of the distribution for $0 < \Delta V < 100$ mV.

The channel signal amplitude distribution for 5 GeV/c negative muons is shown in Fig. 5.3 (a). In Fig. 5.3 (b) the same distribution is limited to the 0-100 mV range; the peaks corresponding to different fired pixels are clearly visible. At $\sim$ 10 mV the distribution is dominated by the dark current.

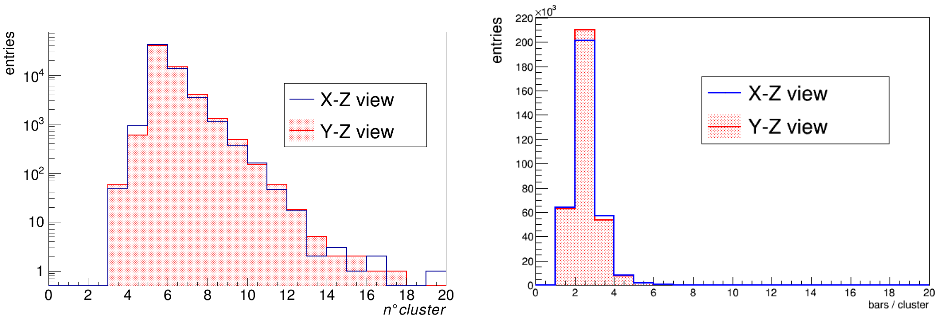

(a)

(b)

Figure 5.4: (a) Cluster distributions for each detector view: XZ (blue histogram) and YZ (red histogram). (b) Number of bars fired per cluster in the XZ (blue histogram) and YZ (red histogram) views.

5.1.2 *Clusters* identification

The second step of the analysis chain is the identification of *clusters*. A cluster is a collection of adjacent bars with a signal over threshold (in general $\Delta V > 10$ mV, i.e. larger than the 1st pixel signal).

Cluster information is stored in a tree with the event id, the timeStamp and the channel signal amplitudes. For each event, the tree contains the number of clusters in all the detector planes in the XZ and YZ views and the number of clusters in each plane. The distributions of the number of clusters are shown in Fig. 5.4 (a) for $\sim$ 62000 events of 5 GeV/c π^- (blue histogram for the XZ view and red histogram for the YZ view). For each cluster the following information is provided: the number of fired bars (cluster multiplicity), the cluster plane ID (from 1 to 5), and the channels ID (from 0 to 15). In Fig. 5.4 (b) the distributions of the number of bars fired per cluster are shown for the XZ (blue histogram) and YZ (red histogram) views for 5 GeV/c π^-. The majority of clusters are composed by 1, 2 or 3 bars. For each detector plane the following data are also provided:

- the number of cluster of 1 fired bar;
- the number of cluster of 2 fired bars;
- the number of cluster of 3 fired bars;
- the number of cluster of 4 fired bars;
- the number of cluster of more than 4 fired bars

5.1.3 Track reconstruction

The third step of the analysis chain is the event selection to identify a track in the XZ and YZ views. A flag is used to tag events having in each

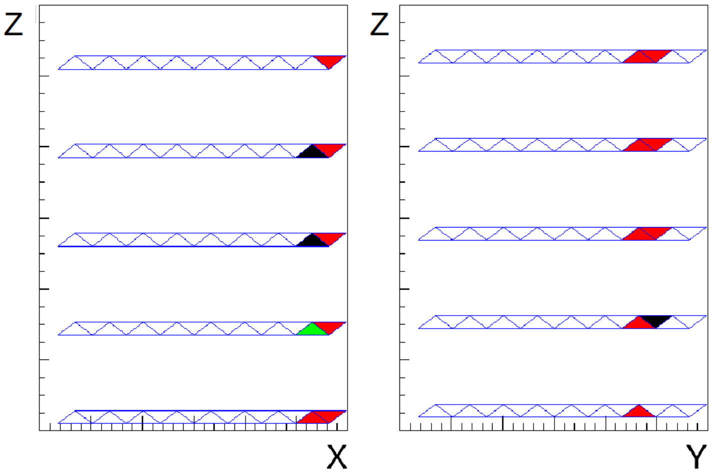

Figure 5.5: An event with a single bar cluster at the detector border in one plane (channel 15 of plane # 5 X) to whom the nominal fiber position is associated.

plane only 1 cluster of 1 or 2 bars.

A quality cut is applied to remove events with a cluster of 1 fired bar at the edge of the detector, i.e. a cluster with channel ID 0 or 15 as shown in Fig. 5.5. In fact, in the plane with a single bar cluster at its border it is not possible to reconstruct the particle crossing point. Another quality cut was applied by a χ^2 estimator. For both the XZ and YZ views a χ^2 estimator is constructed as the sum of squared residuals between the reconstructed positions $X_{rec,i}$ ($Y_{rec,i}$) and the fit positions $X_{fit,i}$ ($Y_{fit,i}$) over all planes:

$$\chi^2 = \sum_{i=1}^{5} (X_{rec,i} - X_{fit,i})^2 \tag{5.1}$$

Only events with $\chi^2 \leq 0.25$ cm^2 were selected. In this way events like the ones shown in Fig. 5.6 (a) and 5.6 (b) are removed. Fig. 5.6 (a) shows an event with a 2 bars cluster in plane # 5 in both XZ and YZ views which could be associated to another particle or could be due to the multiple scattering. These events are eliminated in the evaluation of the spatial resolution. Fig. 5.6 (b) shows an event with a spurious 1-bar-cluster with a signal amplitude < 20 mV in plane # 1 of the XZ view.

By applying these criteria the number of selected 5 GeV/c π^- events is about 6 % of the original sample of $\sim$ 62000 events.

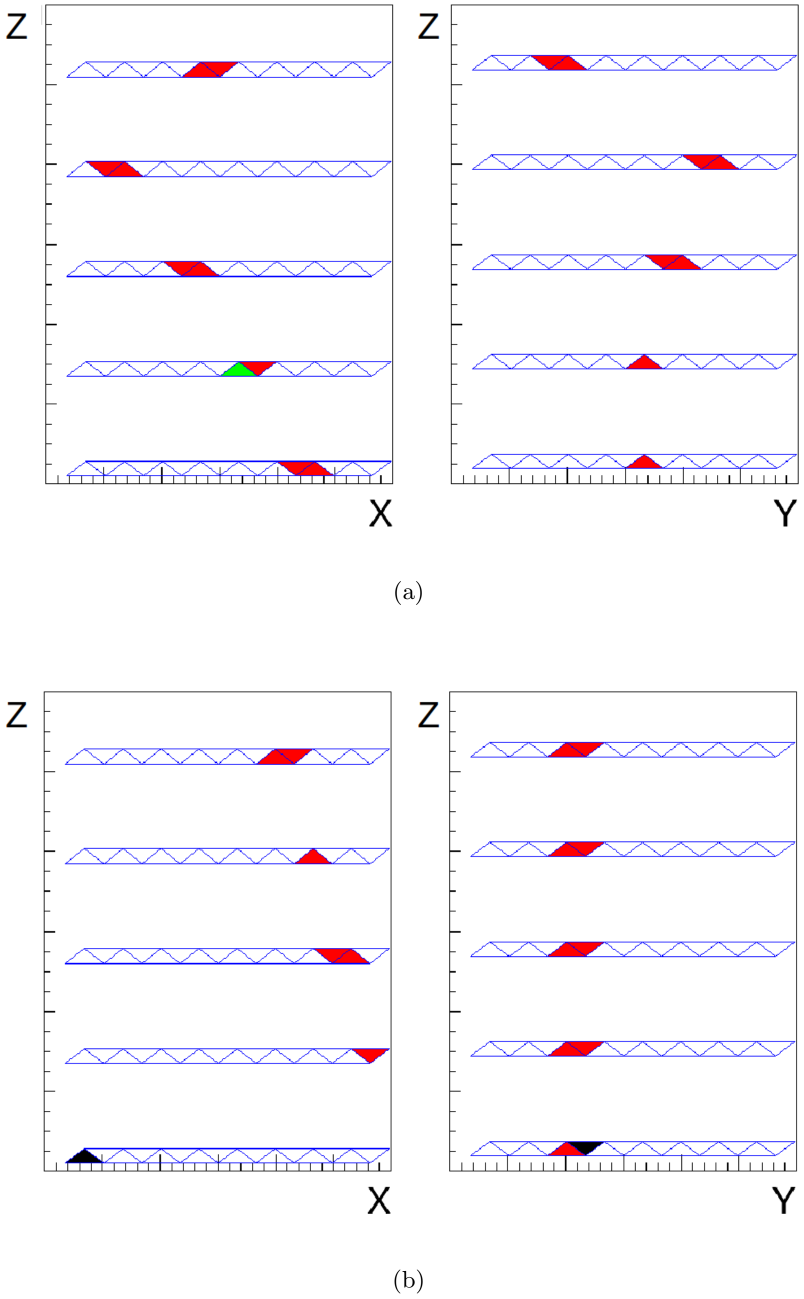

(a)

(b)

Figure 5.6: An example of events removed from the sample by applying the quality cut on χ^2. (a) The event has a cluster of 2 bars in plane # 5 X and Y which could belong to another particle or could be due to the multiple scattering. (b) The event has a spurious 1 bar cluster with signal amplitude < 20 mV (dark current pixel) in the X plane # 1 X.

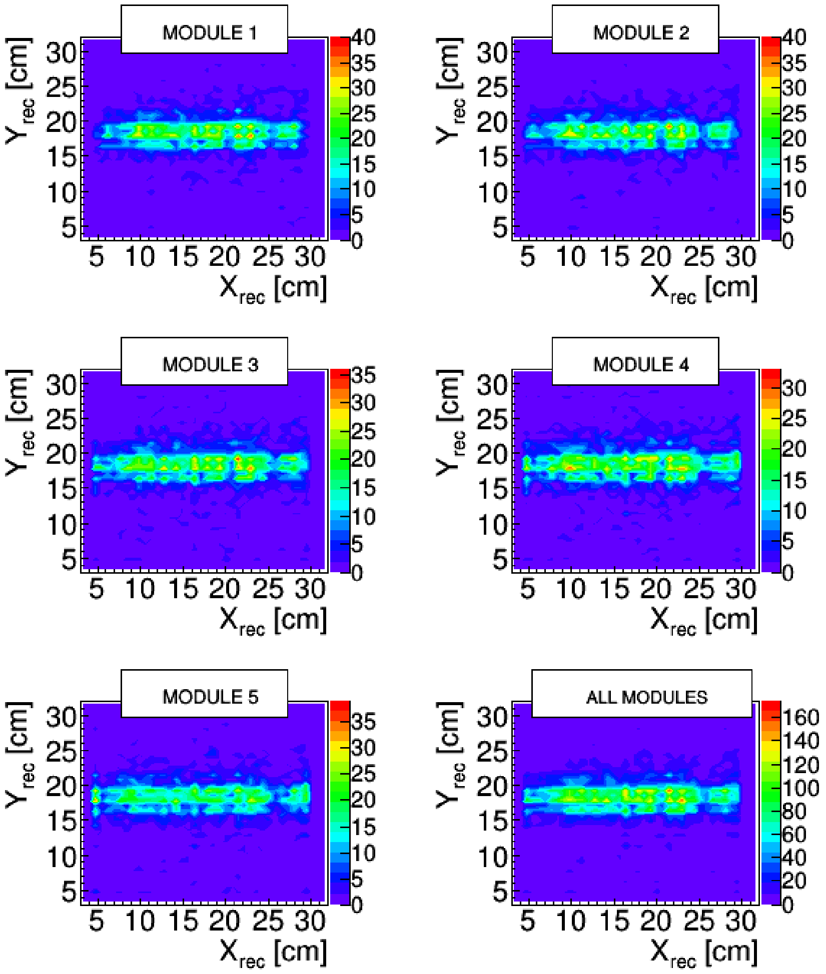

Figure 5.7: Scatter plots of X_{rec}, Y_{rec} reconstructed positions in each detector module for a subsample of 5 GeV/c π^- events. The sum of clusters in all modules is shown in the last pad.

5.1.4 Spatial resolution

As a further analysis step, the particle crossing positions for event tracks selected as described in the previous section were determined using formula 3.3. To this end the signal amplitudes of detector channels were corrected applying channel equalization factors. XY scatter plots of reconstructed positions in each detector module are shown in Fig 5.7 for the selected 5 GeV/c π^- subsample. To each reconstructed position in the XZ view a reconstructed position is unambiguously associated in the corresponding YZ view. The shape of the scatter plots reproduces that of the beam: $\sim$ 25 cm wide along the X direction and $\sim$ 5 cm wide along the Y direction.

For each reconstructed position, X_{rec}, in the XZ (or YZ) views the correct

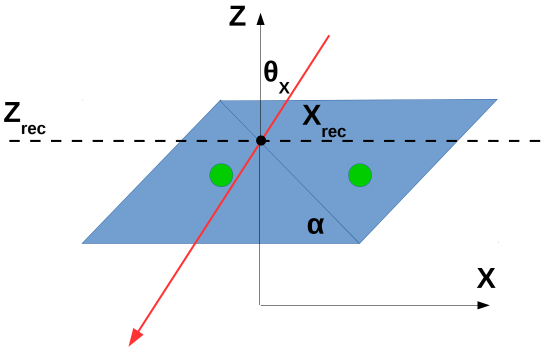

Figure 5.8: Determination of the Z_{rec} coordinate in the XZ view. The same procedure is applied for the YZ view.

coordinate along the Z axis, Z_{rec}, is determined as shown in Fig. 5.8. The reconstructed positions in all planes of each view were fitted to a straight line. In each plane the X (or Y) fit positions X_{fit} are calculated at the correct Z_{rec} coordinate. The distributions of track slopes θ_X for 5 GeV/c particles in positive beam polarity (mainly π^+ and protons as shown in Tab. 4.2) are shown in Fig. 5.9 (a). The three distributions in the figure refer to runs with the detector tilted by different angles (0°, -5° and -10°) with respect to the beam axis (Z). Fig. 5.9 (b) shows the distribution of track slopes θ_Y with the Z axis of the detector aligned with the beam direction.

The residual, $X_{fit} - X_{rec}$, between the predicted fit position and the reconstructed position on each i-th detector plane is determined. The corresponding distribution is shown in Fig. 5.10 (a); the red curve is the Gaussian fit whose width is $\sigma_{in,i} = (1.26 \pm 0.02)$ mm. If the i-th detector is excluded from the fit, the width $\sigma_{ex,i}$ of the resulting residual distribution (see Fig. 5.10 (b)) is (1.56 ± 0.02) mm. It has been shown in [81] that a good estimator for the spatial resolution of the i-th detector is given by the geometric mean:

$$\sigma_{geom} = \sqrt{\sigma_{in} \cdot \sigma_{ex}} \tag{5.2}$$

A toy MC was performed to confirm the geometric mean as a good estimator of the spatial resolution. Tracks with a random slope were generated and the track positions were calculated in each plane at five evenly spaced Z coordinates along the track. The reconstructed positions X_{rec} along the X direction in each plane were calculated applying a gaussian smearing, with $\sigma = 1$ mm, to the track position. A linear fit of the reconstructed positions in all planes was performed and the residuals between the reconstructed positions and the track fit position $X_{fit} - X_{rec}$ on each plane is computed. The spatial resolution $\sigma_{in,i}$, i.e. the width of the gaussian fit to the distributions

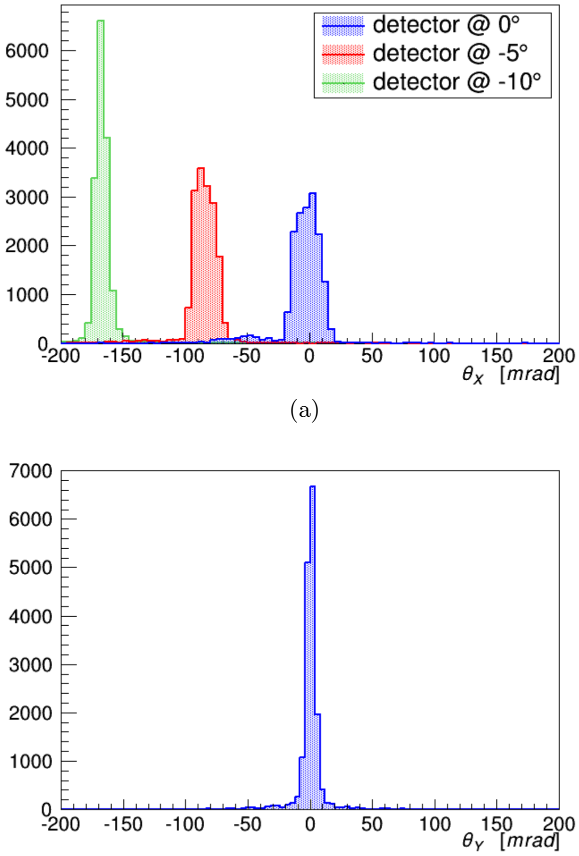

(a)

(b)

Figure 5.9: (a) The distributions of track slopes, θ_X, in the XZ view for runs at 5 GeV/c in positive polarity with the detector tilted at different angles with respect to the beam: 0° (blue histogram), -5° (red histogram) and -10° (green histogram). The tail at the left side of the blue histogram peaked at -50 mrad is due to the muon component in the beam spill. (b) The distribution of track slopes, θ_Y, in the YZ view.

of residuals, is shown in Fig. 5.11 (blue dots) for each plane. The lever arm is larger for external planes which have a better spatial resolution. Then a linear fit of the reconstructed positions was performed excluding the i-th plane from the fit. The spatial resolution $\sigma_{ex,i}$ obtained in the excluded plane is shown in Fig. 5.11 (red dots). In this case the spatial resolution on external planes is worse since the track fit position, X_{fit}, is extrapolated. In Fig. 5.11 black dots represent the spatial resolution obtained by applying equation 5.2, which correctly reproduces the expected resolution σ. In the following the spatial resolutions of detector planes was determined by the Geometric Mean Method.

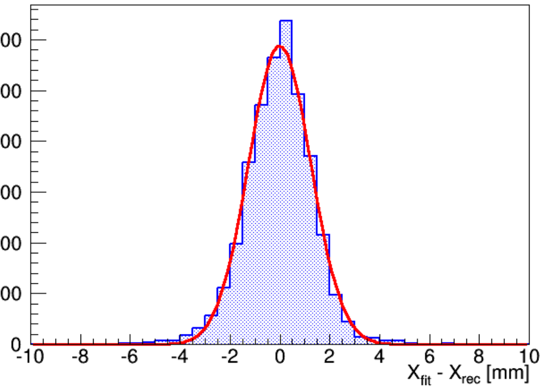

(a)

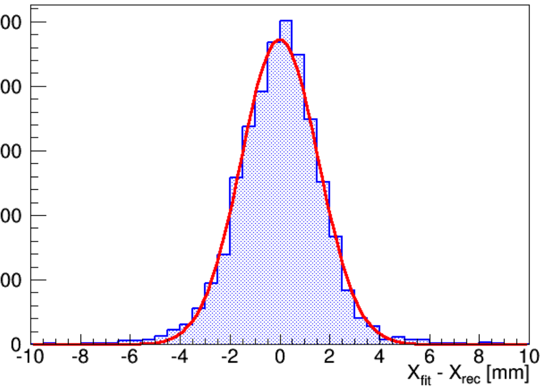

(b)

Figure 5.10: (a) Distribution of residuals, $X_{fit} - X_{rec}$ between the predicted fit position and the reconstructed one on a plane. The plane is included in the fit. The red curve is the gaussian fit to the distribution. (b) The distribution of residuals $X_{fit} - X_{rec}$ on a plane not included in the fit.

5.2 Results

In section 4.4 I reported about the determination of individual channel equalization factors obtained by injecting laser pulses. Equalization factors were also derived from the beam data by analysing $\sim 2.7{\cdot}10^5$ negative muon events at 5 GeV/c. To this end the median $m_{i,j}$ of the signal amplitude distribution of i-th channel in the j-th plane was computed. In order to remove dark current contributions a threshold of 20 mV on signal amplitudes was applied. The corresponding equalization factor $c_{i,j}$ was estimated as:

$$c_{i,j} = \frac{m_{i,j}}{\frac{1}{N}\sum_{i=1}^{N} m_{i,j}} \tag{5.3}$$

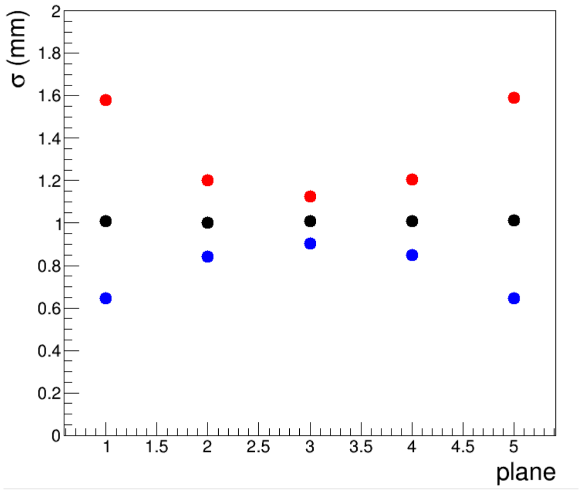

Figure 5.11: Spatial resolutions $\sigma_{in,i}$, $\sigma_{ex,i}$ and $\sigma_{geom,i}$ of each plane obtained with a toy MC. The spatial resolution $\sigma_{in,i}$ (blue dots) of each plane is obtained by fitting the reconstructed positions of all planes. The spatial resolutions $\sigma_{ex,i}$ (red dots) in the plane excluded from the fit is obtained by fitting the reconstructed positions in four out of five planes. Black dots are the spatial resolutions calculated as the geometric mean between $\sigma_{in,i}$ and $\sigma_{ex,i}$.

where N = 16 is the number of channels in each plane. The results are reported in Fig. 5.12 for each plane. The error on the median, assumed the same for all channels, is $\Delta/\sqrt{12} \sim 3$ mV, Δ being the bin width of the signal amplitude distributions. Calibration factors shown in Fig. 5.12 can be compared with those shown in Fig. 4.17: they differ on average by 20%, except those of XZ plane # 1 that differ by about 30%.

I studied the dependence of plane spatial resolution on the threshold set on the signal amplitude to identify clusters. The data of π^- at 5 GeV/c ($\sim$ 62000 events in total) were processed using three different thresholds for the cluster selection: 10, 18 and 26 mV, i.e. 2 mV above the mean signal amplitude of the 1st, 2nd and 3th pixel, respectively. In Fig. 5.13 the spatial resolutions for each plane are shown as a function of the minimum signal amplitude. The spatial resolution improves lowering the threshold on the signal amplitude because the size of the region at the vertex of the triangular bar where the particle crossing point can't be reconstructed decreases. The fraction of events with only 1 cluster of 1 or 2 fired bars in each plane as a function of the applied amplitude threshold, for a sample of 5 GeV/c π^- is reported in table 5.1. As shown in the table, for a threshold of 10 mV on bar signal amplitude, the percentage of events having 1 cluster of 1 or 2 fired bars in each plane that has to be reconstructed is significantly reduced.

Data of π^- at 5 GeV/c were used to correct for mis-alignment of detector planes. Only events with 1 cluster of 1 or 2 bars in each plane were selected. A fit of the reconstructed positions in all planes was performed to determine

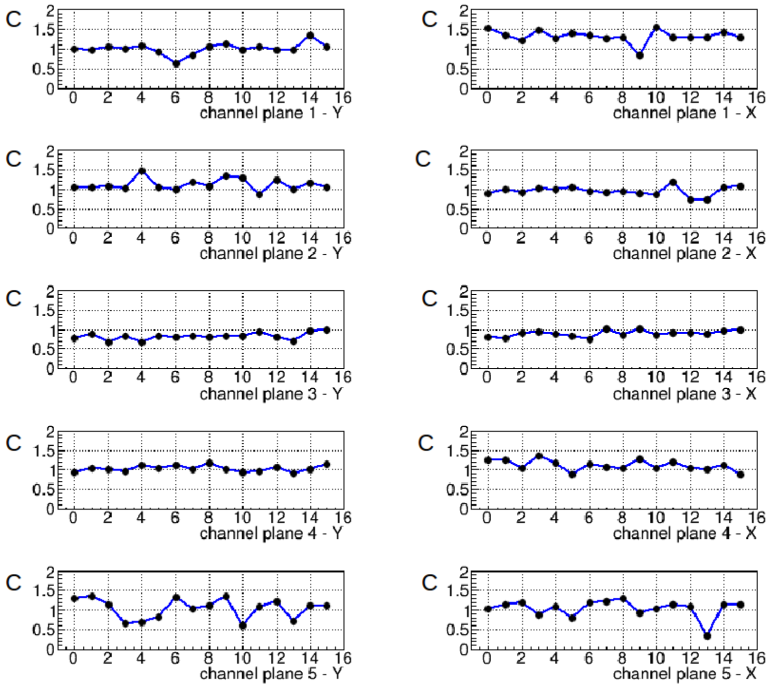

Figure 5.12: Channel equalization factors, C, determined by analysing data of μ^- at 5 GeV/c.

the track fit slope in the XZ and YZ views. Each reconstructed position, $X_{rec,i}$, in plane i-th was projected using the slope of the fitted track, to the plane $(i+1)$-th obtaining $X'_{rec,i}$ as shown in Fig. 5.14. The differences $\delta_{i+1,i'}$ between the reconstructed position $X_{rec,i+1}$ in the $i+1$-th plane and the reconstructed projected position $X'_{rec,i}$ were evaluated. The differences $\delta_{2,1'}$, $\delta_{3,2'}$, $\delta_{4,3'}$ and $\delta_{5,4'}$ are the offsets used to align the detector planes with respect to plane # 1:

1. $offset_{P_1} = 0$
2. $offset_{P_2} = -\delta_{2,1'}$
3. $offset_{P_3} = -\delta_{3,2'} - \delta_{2,1'}$
4. $offset_{P_4} = -\delta_{4,3'} - \delta_{3,2'} - \delta_{2,1'}$
5. $offset_{P_5} = -\delta_{5,4'} - \delta_{4,3'} - \delta_{3,2'} - \delta_{2,1'}$

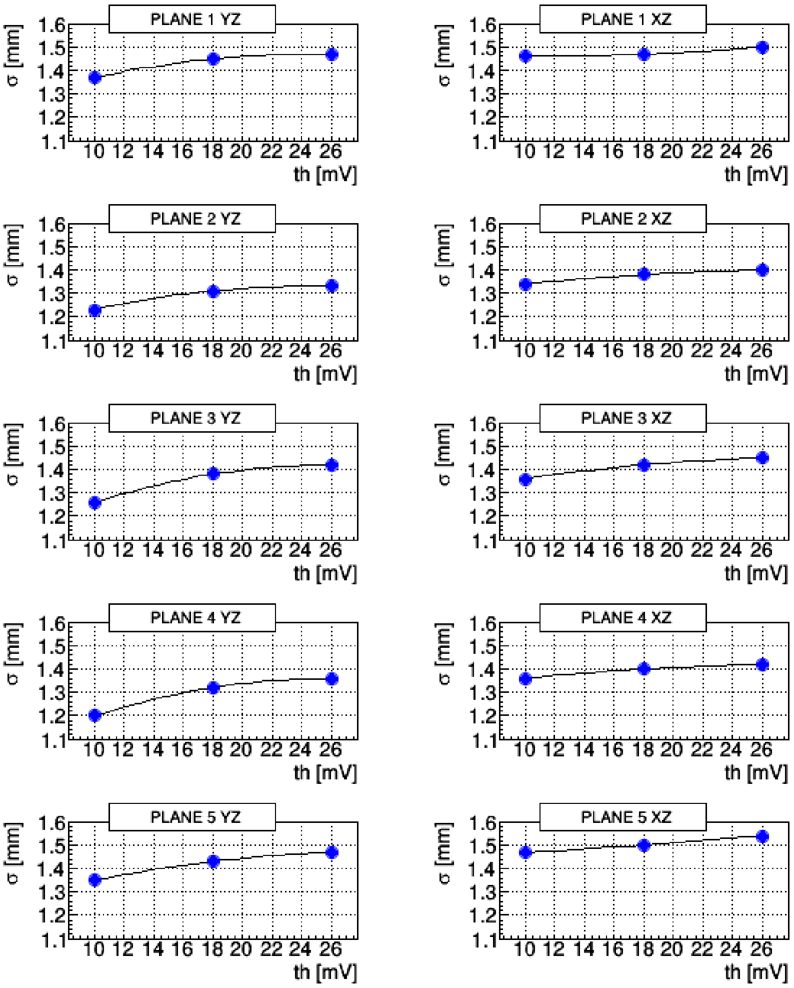

Figure 5.13: The spatial resolution, σ, of each plane versus of the signal amplitude threshold. Thresholds of 10, 18 and 26 mV to cut the 1st, the 2nd and the 3th pixel respectively.

5.2.1 Spatial resolution

Results on the spatial resolution for 5 GeV/c π^- with the detector not tilted with respect to the beam axis are shown in Fig. 5.15 (a), (b). Fig. 5.15 (a) shows the spatial resolution of each plane obtained excluding the plane from the fit. In this case the spatial resolution is worse for external planes as previously discussed. In Fig. 5.15 (b) the spatial resolution was obtained including all planes in the fit. In this case the resolution is better for external planes.

The spatial resolutions calculated as the geometric mean of σ_{ex} and σ_{in} is shown in Fig. 5.16 for each plane. The mean values for the XZ and YZ planes are $\sigma_X \sim (1.4 \pm 0.1)$ mm and $\sigma_Y \sim (1.3 \pm 0.1)$ mm, respectively.

th (mV)	events (%)
10	6.1
18	33.4
26	49.0

Table 5.1: Fraction of events with only 1 cluster of 1 or 2 fired bars in each plane as a function of the applied amplitude threshold, for a sample of 5 GeV/c π^-.

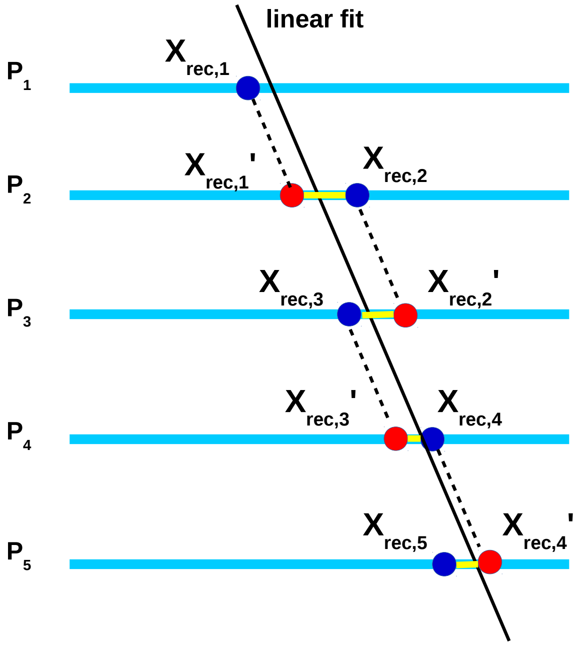

Figure 5.14: Procedure applied to align the detector planes. Blue dots are the reconstructed positions $X_{rec,i}$ in each plane, red dots are the projections $X'_{rec,i}$ obtained using the slope of the fit track (black line), yellow lines are the the differences $\delta_{i+1,i'}$ obtained to calculate the offset between detector planes.

For this run the spatial resolutions of XZ planes are worst than those of YZ planes. As discussed below there is a dependence of the spatial resolution on the track slope. In the Y direction the beam is more collimated (see Fig. 5.7 and 5.9 (b)) with a mean track slope $< \theta_Y >=$ 0.3 mrad while in the X direction the beam is more divergent (blue histogram of Fig. 5.9 (a)) with a mean track slope $< \theta_X >=$ -4.7 mrad.

In order to evaluate the dependence of the spatial resolution on the track slope data acquisitions with the detector tilted at different angles with respect to the beam axis were performed. About 74000 events were acquired at -5° tilt angle and about 300000 events at -10° tilt angle. The track slope

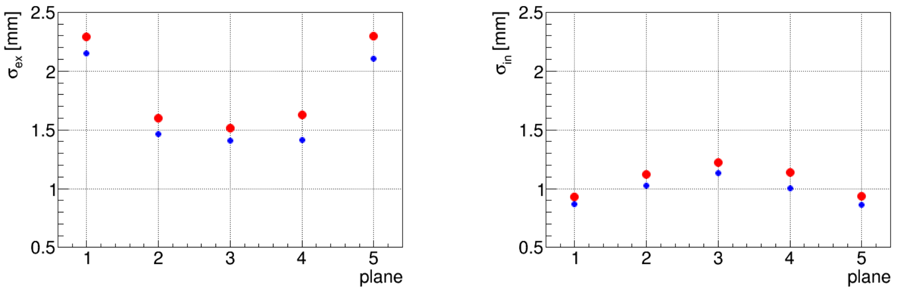

(a) (b)

Figure 5.15: (a) Spatial resolution σ_{ex} of each plane obtained excluding the plane from the fit. Red dots are referred to the X planes while blue dots are referred to the Y planes. (b) Spatial resolution σ_{in} of each plane obtained including all the planes in the fit.

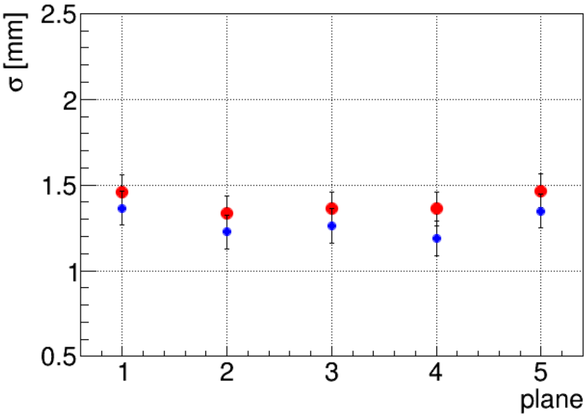

Figure 5.16: Spatial resolutions of the XZ planes (red dots) and the YZ planes (blue dots) obtained as geometric mean between σ_{ex} and σ_{in}. Errors bars are given by the standard deviation of the measured spatial resolutions.

distributions in the XZ plane are shown in Fig. 5.9 (a) together with that obtained for the run with the un-tilted detector. Fig. 5.17 (a) shows the average spatial resolution for XZ planes versus the track slope (θ_X) for 5 GeV/c particle momentum. Each point is obtained selecting events with a track slope within 0° ± 1°, -5° ± 1° and -10° ± 1°, respectively. One can observe that the spatial resolution worsens at larger angles. This effect may arise from residual misalignment among detector planes as well as among plane bars. Fig. 5.17 (b) shows the average spatial resolution of the XZ planes versus the track slope θ_X for 1 GeV/c particle at different tilting angle of the detector. Comparing the plot of Fig. 5.17 (a) with that of Fig. 5.17 (b), a worse spatial resolution is observed for 1 GeV/c beams with respect to that obtained at 5 GeV/c. The spatial resolution as a function of the particle

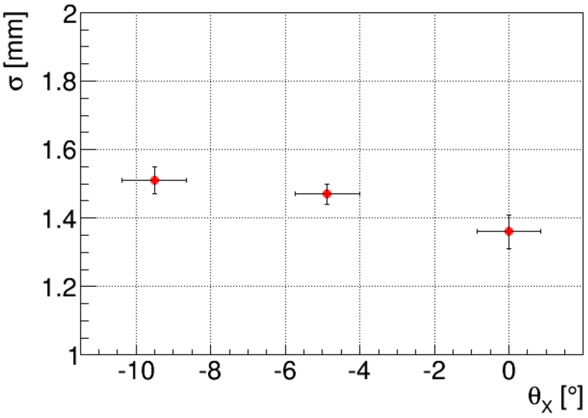

(a)

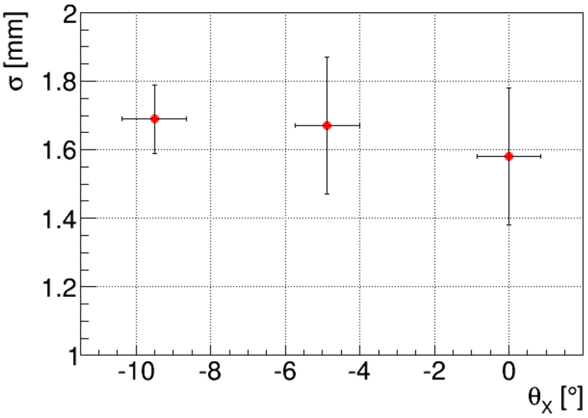

(b)

Figure 5.17: Average spatial resolutions for XZ planes versus the track slope θ_X for runs at 5 GeV/c (a) and for runs at 1 GeV/c (b). Vertical bars are the standard deviation of the measured spatial resolutions. Horizontal bars represent the bin width (2°).

momentum is shown in Fig. 5.18 for runs in negative beam polarity. Each red (blue) point is the average of the spatial resolutions of all XZ (YZ) planes. In negative polarity at 0.5 GeV/c the beam is mainly composed of electrons, while at 5 GeV/c and 10 GeV/c the beam main component are pions. The plot shows a worsening of the spatial resolution at lower momentum which can be explained as an effect due to the Multiple Coulomb Scattering (MCS) contribution, larger at lower energies [19]. The MCS contribution enlarge the particle displacement along the X and Y directions, thus increasing the width of the distribution of residuals in each plane.

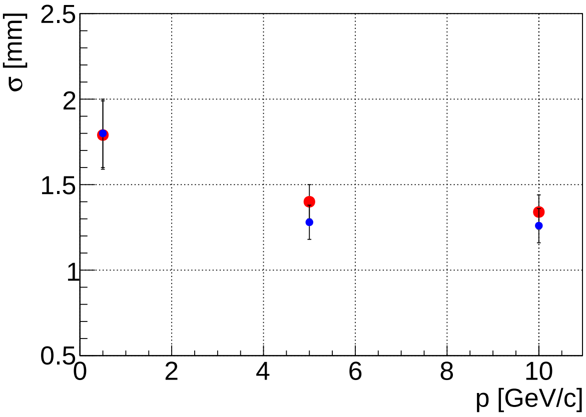

Figure 5.18: Spatial resolutions obtained as the geometric mean between σ_{ex} and σ_{in} for runs in negative beam polarity and at different particle momentum: 0.5, 5 and 10 GeV/c. Red dots are referred to the X planes and blue dots are referred to the Y planes. Each data point is the mean value of detector plane spatial resolutions. Error bars are the standard deviations of the measured spatial resolutions.

5.2.2 Plane tracker efficiency

In order to evaluate the plane efficiency different runs were performed excluding from the trigger one module at the time. Trigger configurations 8, 9, 10, 11 and 12 listed in section 4.6 were applied to 5 GeV/c and 10 GeV/c π^- beams. For each trigger two acquisition runs were done with a threshold of 60 and 45 mV, respectively.

Events with only 1 cluster of 1 or 2 bars in the planes included in the trigger were selected and reconstructed positions were fitted to a straight line. Events in which the projection of the fit position on the plane excluded from the trigger, $X_{fit-excl}$, is within the detector geometrical acceptance (i.e. $X_0 < X_{fit-excl} < X_{15}$, where X_i is the fiber position of bar i-th), are counted in the sample of $N_{tr-included}$ events. For the external planes (1 or 5) an additional requirement was applied selecting only events without clusters at the detector edge in adjacent planes (planes 2 and 4).

Events with 1 cluster in the plane excluded from the trigger with a reconstructed position within 9 cm from the track fit were counted giving the number $N_{tr-excluded}$. The efficiency of a plane was evaluated as $\epsilon = N_{tr-excluded}/N_{tr-included}$. The efficiencies determined at different thresholds are listed in Table 5.2.

5.2.3 Charge mis-identification

Using the measured spatial resolution, the capability of the tracking detector to separate μ^+ and μ^- in a magnetic field of 0.12 T has been

plane	efficiency - th 60 mV (%)	efficiency - th 45 mV (%)
1 - X	99.84 ± 0.06	99.87 ± 0.06
1 - Y	99.68 ± 0.08	99.84 ± 0.06
2 - X	99.97 ± 0.02	99.93 ± 0.03
2 - Y	99.97 ± 0.02	99.96 ± 0.02
3 - X	99.94 ± 0.03	99.91 ± 0.03
3 - Y	99.97 ± 0.02	99.97 ± 0.02
4 - X	99.81 ± 0.05	99.77 ± 0.05
4 - Y	99.96 ± 0.02	99.96 ± 0.02
5 - X	99.29 ± 0.13	99.26 ± 0.12
5 - Y	99.44 ± 0.11	99.53 ± 0.09

Table 5.2: Detector plane efficiencies determined for different values of the minimum signal amplitudes of scintillator bars, namely 60 mV and 45 mV, respectively. Uncertainties are statistical errors.

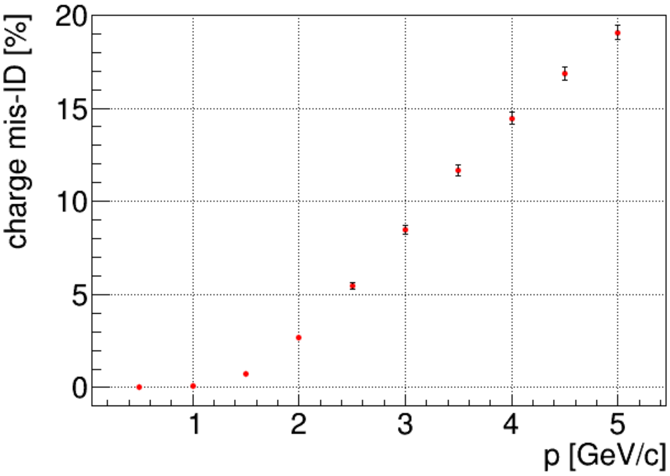

Figure 5.19: Charge mis-identification (%) as a function of the particle momentum. The vertical bars indicate the statistical error.

roughly estimated using a toy MC simulation. To each reconstructed position a gaussian smearing having the size of the spatial resolution was applied. A conservative value of 1.8 mm was used. A parabolic fit to the reconstructed positions was performed, i.e. $x = az^2+bz+c$. The charge sign is reconstructed if $|a| < 3\sigma_a$, where σ_a is the statistical error on the parameter a. The charge mis-ID was evaluated by the ratio of the number of event with a wrong charge sign to the number of events with a reconstructed charge. The charge mis-ID obtained at different particle momenta is shown in Fig. 5.19. A charge mis-ID < 3 % is obtained for $p \leq 2$ GeV/c.

Conclusions

The goal of this thesis was to design, construct and test a tracking detector to instrument a magnetic light spectrometer for the charge sign and momentum measurement of $O(1\text{ GeV})$ muons. This activity was started in the context of a program aimed at searching for sterile neutrinos at the ~ 1 eV mass scale with a short baseline ν_μ beam experiment. A basic requirement of the experiment was the capability to separate, at few percent level, ν_μ from $\overline{\nu}_\mu$ CC interactions. It had been shown that in order to reach a muon charge mis-ID < 3 % at ~ 1 GeV, muon trajectories should be reconstructed with an accuracy of $O(1\text{ mm})$.

The designed tracking detector is composed of planes of triangular scintillator bars (3.3×1.7 cm^2 cross section) with embedded WLS fibers coupled to SiPMs which are readout in analog mode. The novelty of the adopted approach is the reconstruction of the particle crossing point in each detector plane by the energy released in adjacent scintillator strips. My thesis aims at showing that $O(1\text{ mm})$ spatial resolution can be achieved with a tracker based on cm-size scintillator bars.

As a first step the idea was validated by realizing a lab set up tested with cosmic muons. Several preliminary tests on the characterization of SiPMs (dark current, temperature dependence, cross-talk) and of scintillator bars + WLS fiber (attenuation length, optical coupling, number of photoelectrons/mip) were carried out. Measurements with a preliminary tracking system, composed of 4 detector planes, each with 4 scintillator bars, showed that a spatial resolution better than 2 mm could be achieved.

In the next step a tracker prototype was developed and tested with charged beams (muons, pions and electrons of few GeV/c momentum) at the CERN PS. The prototype was composed of 5 detector modules, each consisting of two orthogonal planes of triangular bars, with 16 bars assembled in each detector plane. About 3.6 millions of events were acquired in different beam configurations. In the data analysis, *clusters* were identified as a collection of signals over threshold ($\Delta V > 10$ mV) in adjacent bars. Only events with 1 cluster of 1 or 2 bars in each plane were selected. In this way a track in both XZ and YZ views was identified. Quality cuts were applied to take into account the geometric detector acceptance, and to discard isolated clusters (from dark current or large angle scattering). The particle crossing point in each plane was determined and a linear fit of the reconstructed positions in 5 planes was performed. The distribution of residuals between the fit positions and the reconstructed positions was used to evaluate the spatial resolution in the XZ and YZ planes, σ_X and σ_Y, respectively. At 5 GeV/c π^- $\sigma_X \sim (1.4 \pm 0.1)$ mm and $\sigma_Y \sim (1.3 \pm 0.1)$ mm. The dependence of the spatial resolution on the track slope was investigated with 5 GeV/c pions. A worsening of the resolution due to residual misalignment of detector planes is observed at larger track angles, f.e. (1.5 ± 0.1) mm at 10°. At low particle momentum the Multiple Coulomb Scattering affects significantly the spatial resolution: at 0.5 GeV/c $\sigma_{X,Y} \sim (1.8 \pm 0.2)$ mm . The measured plane efficiency is larger than 99 % for all planes.

A preliminary estimation of the muon charge mis-identification was performed. Assuming conservatively 1.8 mm spatial resolution a charge mis-ID < 3 % is obtained at $p_\mu \leq 2$ GeV/c.

In conclusion, in this thesis I have shown that with a tracking detector based on planes of centimeter size triangular scintillator bars $O(1$ mm$)$ spatial resolution can be achieved. Thus a limited number of electronic channels would be needed also in a large size apparatus. The accuracy in the charge identification and detector efficiency would meet the requirements for the application of the system in neutrino experiments.

Acknowledgements

At the end of this thesis work I want to thank all the people that during these three years helped me in reaching this important goal.

I wish to thank my supervisor, Laura Patrizii, that proposed me this work and made this project possible. Many thanks to Stefano Cecchini that has always followed me during these three years, taking care of my education and giving me help every time I was in doubt. I want to thank Gianni Mandrioli for all his precious suggestions and teachings.

Special thanks to my co-supervisors: Michele who took care of this project since its beginning, giving always precious help to solve problems and Nicoletta who helped me a lot in the last part of this work.

I wish to thank Matteo and Gabriele for all their help and suggestions. Many thanks to Luigi that realized an important part of this work, taking care of the technical side. Special thanks to the Electronics Center of INFN Bologna, in particular to its coordinator, Ing. Ignazio D'Antone and to Ignazio Lax, for the development of the electronic readout. I also wish to thank the mechanical workshop of INFN Bologna and its coordinator, Dr. Anselmo Margotti, for the construction of the tracker prototypes.

I wish to thank the people I worked with at CERN during my period abroad. Many thanks to Federico Cindolo for all the work done in developing the DAQ and the help received for the beam test. Special thanks to Umut Kose that took care of me since the first day when I arrived: it was a pleasure to work with you. I would like to thank Marzio Nessi who gave me the possibility to spend my period abroad at CERN, joining the Neutrino Platform research activity.

Many thanks to the group of INFN Lecce for discussions and important contributions to this work.

I acknowledge the support of the European Union's Horizon 2020 Research and Innovation programme for the received funding to this work.

I want to thank the spokesman of the NESSiE Collaboration, Luca Stanco, for the continuos support to this project.

My gratitude goes also the other people of Bologna lab, Vincent, Claudia, Eduardo, Budda and Donato for making the lab a good and comfortable place to work.

Finally, I thank all the people that have been close to me during these years. Thanks to Francesco for all his love and support. Thanks to my family, Mum, Dad, Sara and Simone that are always present and helpful for everything and without whom I couldn't have done it.

Bibliography

[1] W. Pauli, *Letter to a physicist's gathering at Tubingen, December 4, 1930*. Reprinted in *Wolfgang Pauli, Collected Scientific Papers*, ed. R. Kronig and V. Weisskopf, Vol. 2, p. 1313 (Interscience: New York, 1964).

[2] F. Reines and C.L. Cowan, Nature 178 (1956) 446-449.

[3] G. Danby et al., Phys. Rev. Lett. 9 (1962) 36-44.

[4] ALEPH Collaboration, D. Decamp et al., Phys. Lett. B 235 (1990) 399.

[5] DONUT Collaboration, K. Kodama et al., Phys. Lett. B 504 (2001) 218-224.

[6] ATLAS Collaboration, G. Aad et al., Phys. Lett. B 716 (2012) 1-29.

[7] CMS Collaboration, S. Chatrchyan at al., Phys. Lett. B 716 (2012) 30-61.

[8] B. Pontecorvo, Zh. Eksp. Teor. Fiz. 53 (1967), 1717-1725.

[9] R. Davis, Jr., D.S. Harmer, K.C. Hoffman, Phys. Rev. Lett. 20 (1968) 1205-1209.

[10] GALLEX Collaboration, W. Hampel et al., Phys. Lett. B 447 (1999) 127-133; SAGE Collaboration, J. N. Abdurashitov et al., Phys. Rev. C 60 (1999) 055801; GNO Collaboration, M. Altmann et al., Phys. Lett. B 616 (2005) 174-190.

[11] SUPER-KAMIOKANDE Collaboration, J. Hosaka et al., Phys. Rev. D 73 (2006) 112001.

[12] KAMIOKANDE-II Collaboration, K.S. Hirata et al., Phys. Lett. B 205 (1988) 416-420.

[13] SUPER-KAMIOKANDE Collaboration, K. Abe et al., Phys. Rev. Lett. 97 (2006) 171801.

[14] SOUDAN-2 Collaboration, W.W.M. Allison et al., Phys. Rev. D 72 (2005) 052005.

[15] MACRO Collaboration, M. Ambrosio et al., Eur. Phys. J. C 36 (2004) 323.

[16] MACRO Collaboration, G. Giacomelli et al., Phys. Atom. Nucl. 67 (2004) 1139-1146.

[17] M. Apollonio et al., Phys. Lett. B 466 (1999) 415-430.

[18] F. Boehm et al., Phys. Rev. Lett. 84 (2000) 3764-3767.

[19] J. Beringer et al., (Particle Data Group) Phys. Rev. D 86 (2012) 010001.

[20] KamLAND Collaboration, T. Araki et al., Phys. Rev. Lett. 94 (2005) 081801.

[21] KamLAND Collaboration, S. Abe et al., Phys. Rev. Lett. 100 (2008) 221803.

[22] MINOS Collaboration, D. G. Michael et al., Nucl. Instrum. Meth. A 596 (2008) 190-228.

[23] L.H. Whitehead, Nucl. Phys. B 908 (2016) 130-150.

[24] K. Abe et al., Phys. Rev. D 91 (2015) 072010.

[25] OPERA Collaboration, N. Agafonova et al., Phys. Rev. Lett. 115 (2015) 121802.

[26] LSND Collaboration, A. Aguilar et al., Phys. Rev. D 64 (2001) 112007 (Preprint hep-ex/0104049).

[27] KARMEN Collaboration, B. Armbruster et al., Phys. Rev. D 65 (2002) 112001.

[28] G. Mention et al. 2011 Phys. Rev. D 83 (2011) 073006 (Preprint arXiv:1101.2755).

[29] K. N. Abazajian et al., *Light Sterile Neutrinos: A White Paper*, arXiv:1204.5379 [hep-ph].

[30] GALLEX Collaboration, P. Anselmann et al., Phys. Lett. B 342 (1995) 440-450.

[31] SAGE Collaboration, J. N. Abdurashitov et al., Phys. Rev. C 73 (2006) 045805 (Preprint nucl-ex/0512041).

[32] J. Kopp, M. Maltoni and T. Schwetz, Phys. Rev. Lett. 107 (2011) 091801.

[33] G. Mangano et al., Nucl. Phys. B 729 (2005) 221-234 (Preprint hep-ph/0506164).

[34] G. Mangano and P. D. Serpico, Phys. Lett. B 701 (2011) 296-299 (Preprint arXiv:1103.1261).

[35] P. Minkowski, Phys. Lett. B 67 (1977) 421.

[36] R. N. Mohapatra and G. Senjanovic, Phys. Rev. Lett. 44 (1980) 912.

[37] T. Yanagida, Conf. Proc. C 7902131 (1979) 95.

[38] J. Schechter and J. W. F. Valle, Phys. Rev. D 22 (1980) 2227.

[39] T. Asaka, S. Blanchet and M. Shaposhnikov, Phys. Lett. B 631 (2005) 151-156. (Preprint hep-ph/0503065).

[40] F. Deppisch, P. S. B. Dev and A. Pilaftsis, New J. Phys. 17 (2015) 075019 (Preprint arXiv:1502.06541).

[41] M. Maltoni, T. Schwetz, M. A. Tortola and J. W. F. Valle, Phys. Rev. D 67 (2003) 013011 [arXiv:hep-ph/0207227].

[42] NESSiE Collaboration, P. Bernardini et al., SPSC-P-343 (2011), arXiv:1111.2242v1.

[43] ICARUS-NESSiE Collaboration, M. Antonello et al., SPSC-P-347 (2012), arXiv:1203.3432.

[44] L. Patrizii, ICFA Neutrino European Meeting (Paris, January 2014).

[45] A. Pla-Dalamau et al., Frascati Physics Series XXI (2000) 513-522.

[46] A. Berra et al., NIM A 609 (2009) 129-135.

[47] E. Noah (on behalf of AIDA WP8.5.2) at European Strategy for Neutrino Oscillation Physics, CERN (Geneva, May 2012).

[48] L. Aliaga et al., NIM A 743 (2014) 130.

[49] G. Balbi et al., JINST 9 (2014) T04004.

[50] S. Aoki et al., NIM A 698 (2013) 135-146.

[51] MU-RAY Collaboration, G. Ambrosi et al., NIM A 628 (2011) 120-123.

[52] MU-RAY Collaboration, A. Anastasio et al., NIM A 718 (2013) 134-137.

[53] B. Dolgoshein et al., NIM A 563 (2006) 368-376.

[54] W.R. Leo, *Techniques for Nuclear and Particle Physics Experiments*, Springer-Verlag (1987).

[55] A. Mapelli, *Scintillation Particle Detectors Based on Plastic Optical Fibres and Microfluidics*, PhD. thesis, 2011.

[56] Muhammad H. Rashid, *Microelectronic Circuits: Analysis and Design*, (2015) 284.

[57] J. Millman and A. Grabel, *Microelectronics*, (1994) 48.

[58] B. P. Pal, *Fundamentals of Fibre Optics in Telecommunication and Sensor Systems*, (2005) 388.

[59] http://www.sensl.com/downloads/ds/TN%20-%20Intro%20to%20SPM%20Tech.pdf

[60] D. Renker, E. Lorenz, JINST, 4:P04004, 2009.

[61] Y. Qiang, NIM A 698 (2013) 234.

[62] D. Renker, NIM A 567 (2006) 48.

[63] http://www.crystals.saint-gobain.com

[64] S. Cecchini et al., NIM A 846 (2017) 1-7.

[65] http://www.eqphotonics.de/cms/cms/upload/datasheets/DS-MicroSL.pdf

[66] P. Eckert et al., JINST 7 P08011, 2012 (GosSiP).

[67] http://www.eljentechnology.com/products/accessories/ej-510-ej-520

[68] http://www.mgchemicals.com/products/rtv-silicones/potting-compounds/rtv615

[69] http://advansid.com/home

[70] http://www.caen.it/csite/CaenProd.jsp?idmod=570&parent=11

[71] S. Agostinelli et al., NIM A 506 (2003) 250.

[72] D. Beznosko et al., FERMILAB-CONF-04-216-E (2004).

[73] A. Bross et al., Preliminary proposal AIDA, AIDA-TP-WP 8.5.2-190912 (2012).

[74] http://kuraraypsf.jp/psf/ws.html

[75] http://sensl.com/downloads/ds/DS-MicroCseries.pdf

[76] S. Callier et al., *EASIROC, an Easy & Versatile ReadOut Device for SiPM*, Phys. Procedia 37 (2012) 1569.

[77] http://www.lal.in2p3.fr/

[78] http://sba.web.cern.ch/sba/BeamsAndAreas/East/East.htm

[79] https://www.qt.io/

[80] https://root.cern.ch/

[81] R. K. Carnegie et al., NIM A 538 (2005) 372.